Mémoire

Auteur : Mahran, Marina

Promoteur(s) : Charlier, Bernard

Faculté : Faculté des Sciences

Diplôme : Master en sciences géologiques, à finalité approfondie

Année académique : 2023-2024

URI/URL : http://hdl.handle.net/2268.2/20536

Faculté des Sciences

Département de Géologie

Rédaction et communication scientifiques : Dr Annick ANCEAU

Promoteur du mémoire : Prof. Bernard CHARLIER

Université de Liège

Formation of the P-Fe-Ti-REE Kodal deposit, Norway: the melt inclusion record

Master thesis

By

Marina MAHRAN

Graduate Studies conducted for obtaining a Master's degree in Geological Sciences

Academic year 2023–2024

Remerciements

Je souhaite exprimer ma gratitude à l'ensemble de mes professeurs de géologie, qui, par leur connaissance et leur bonne humeur, ont su transmettre leur passion.

Je tiens à adresser mes plus sincères remerciements au professeur Bernard Charlier pour sa bonne humeur, son soutien, et ses encouragements tout au long de mon travail de fin d'études.

Je remercie également le Docteur Nolwenn Coint pour m'avoir accueillie dans les locaux du service géologique de Norvège et pour avoir partagé avec moi ses précieuses connaissances sur les minéralisations norvégiennes.

Merci à Aliou, Mohammed et Thomas d'avoir pris le temps de m'accompagner lors de l'utilisation de nouveaux instruments de laboratoire. Et merci à Melvyn pour sa gentillesse et son soutien.

Enfin, je remercie très sincèrement ma famille de m'avoir encouragée durant tout mon parcours universitaire.

Abstract

In the southern part of the Permian Oslo Rift (South Norway), the Kodal deposit is an exceptional Fe-Ti oxide and apatite mineralization, consisting of a succession of lenses over 2 km long and 20 m wide. Discovered in the early 18th century, this Fe-Ti-P and REE (Rare Earth Elements) ore is the largest occurrence hosted within alkaline monzonitic rocks. Several studies have been undertaken on the Kodal deposit to determine its origin, resulting in multiple petrogenetic models, but no consensus has been reached yet. The aim of this study is to investigate whether silicate liquid immiscibility played a role in the formation of the remarkable Kodal deposit. To do this, we examined the polycrystalline inclusions hosted within the apatite crystals. The inclusions were re-homogenized at high temperatures, reaching 1100°C, using a piston cylinder apparatus. It appeared that the majority of the inclusions retained residual phases interpreted as solid inclusions trapped along with the liquid. The melt compositions display a narrow compositional range; 29–45.1 wt.% SiO_2 and 6.23–2.43 wt.% FeO_{tot}. This interval corresponds to Fe-rich melts when compared to immiscible pairs highlighted in natural rocks and experimental studies. Despite the disparity in the colors of the polycrystalline inclusions, which range from light to dark tints, the complete absence of Si-rich melts diminishes the likelihood of emulsification of two liquids during the formation of the Kodal deposit. Furthermore, Kodal melt inclusions exhibit a concordant evolution of the major elements with the first basalt sequences extruded in the Oslo Rift.

Keywords: Immiscibility – Kodal deposit – Melt inclusion – Fe-Ti-P ore – Apatite – Oslo Rift

Résumé

Dans la partie sud du Rift permien d'Oslo (Sud de la Norvège), le gisement de Kodal se distingue par une minéralisation exceptionnelle en oxydes de Fe-Ti et en apatite, composée d'une succession de lentilles s'étendant sur 2 km de long et 20 m de large. Découvert au début du XVIIIe siècle, ce minerai de Fe-Ti-P et de terres rares (REE) est la plus grande occurrence hébergée dans des roches monzonitiques alcalines. De nombreuses études ont été entreprises sur le gisement de Kodal afin d'en déterminer l'origine, aboutissant à plusieurs modèles pétrogénétiques, mais aucun consensus n'a encore été atteint. L'objectif de cette étude est de déterminer si l'immiscibilité des liquides silicatés a joué un rôle dans la formation de ce remarquable gisement de Kodal. Pour ce faire, nous avons examiné les inclusions polycristallines piégées dans les cristaux d'apatite. Les inclusions ont été réhomogénéisées à haute température, atteignant 1100°C, au moyen d'un piston-cylindre. Il est apparu que la majorité des inclusions ont gardé des phases résiduelles interprétées comme des inclusions solides piégées avec le liquide. Les compositions des liquides montrent une gamme étroite de composition ; 29–45,1 % en poids de SiO_2 et 6,23–2,43 % en poids de FeO_{tot}, un intervalle qui correspond aux liquides riches en Fe lorsqu'il est comparé aux paires immiscibles mises en évidence dans les roches naturelles et les études expérimentales. Malgré une disparité dans les couleurs des inclusions polycristallines allant du clair au foncé, l'absence totale de liquides riches en Si réduit la probabilité d'une émulsion de deux liquides lors de la formation du gisement de Kodal. De plus, les inclusions vitreuses de Kodal montrent une évolution concordante des éléments majeurs avec les premières séquences de basalte extrudées dans le rift d'Oslo.

Mots clés : Immiscibilité – Gisement Kodal – Inclusion vitreuse – Minerais Fe-Ti-P – Apatite – Rift d'Oslo

Table of Contents

1. Introduction

Melt inclusions form through the entrapment of tiny droplets of melt during the growth of crystals within magmatic environments. They provide invaluable insights into the pressure, temperature, and composition of magma at various stages of its evolution, thereby enhancing our understanding of processes within magma chambers (Roedder, 1979).

In this study, we focus on the abundant poly-crystalline inclusions trapped within apatite crystals in the Kodal deposit (Annex 1). Situated in the southern part of the Oslo Rift (Southern Norway), this deposit is a remarkable example of Fe-Ti oxide and apatite mineralization within alkaline monzonitic rocks. It is more than 1900 meters long, forming a succession of ore lenses rich in magnetite, ilmenite, and apatite, resulting in high concentrations of Fe-Ti-P and rare earth elements (REE). The estimated resources at the Kodal deposit amount to 48.9 Mt at 4.77 wt.% P_2O_5 (Kodal Minerals Plc, 2014), with REE content in apatite reaching up to 19,579 ppm (Annex 2, Decrée et al., 2022), highlighting its exceptional REE enrichment.

Today, phosphorus and REEs are highly valuable to modern society and are classified as critical raw materials by the European Commission. Phosphorus is crucial for global food production, being a primary component in fertilizers, while REEs are essential for green technologies. Phosphorus is typically extracted from phosphate minerals such as apatite found in magmatic systems like Phanerozoic carbonatites and silica-deficient alkalic intrusions (Pufahl & Groat, 2017). However, a significant portion of global phosphorus reserves (~70 %) is located in the sedimentary phosphate deposits of Morocco (U.S. Geological Survey, 2024).

The study of the Kodal deposit presents a unique opportunity in order to shed light on the formation of Fe-Ti-P-rich rocks within an evolved alkaline magmatic system, as these deposits remain poorly understood. Extensive studies have been conducted to unravel the crystallization history of the Kodal deposit, with fractional crystallization and silicate-liquid immiscibility being the main processes proposed for the formation of Fe-Ti-P-rich rocks at Kodal (Berstøl, 1972; Petersen, 1978; Andersen & Seiersten, 1994). However, no consensus has been reached.

Our principal objective is to determine if a bimodal composition of Fe-rich and Si-rich melt inclusions exists, indicating liquid immiscibility during the formation of the P-Fe-Ti ore. To achieve this, we will investigate the polycrystalline inclusions in the Kodal deposit. This involves exploring the mineralogical assemblages precipitated from magmatic liquids trapped at the onset of apatite crystallization. Subsequently, we will heat and quench the apatite crystals to obtain a homogeneous glass that reveals the melt composition at a certain temperature.

The Kodal deposit serves as a valuable case for understanding the formation of Fe-Ti-P mineralization in alkaline systems, as silicate liquid immiscibility has predominantly been suggested as a petrogenetic process occurring in tholeiitic rocks (Veksler & Charlier, 2015).

2. History

In the early 18th century, iron ore was discovered near the village of Kodal, in the southern region of the Oslo Rift, but all attempts to utilize it failed due to its high titanium content (Lindberg, 1985). Since then, interest in the Kodal deposit has continued to escalate, along with its economic value.

The first geological description of the iron-titanium oxide, apatite, and pyroxene bodies at Kodal was provided by Brøgger in 1898 (Bergstøl, 1972). Recognizing the economic potential of the rock, Norsk Hydro conducted the initial prospecting operation on the deposit using a magnetometric survey. As a part state-owned Norwegian energy and resources group, their goal was to exploit the apatite present in the Kodal deposit as a source of phosphate for a fertilizer plant at Herøya (Nielsen, 1967; Berstøl, 1972; Lindberg, 1985). To achieve this, an initial phase included 40 shallow drill holes (less than 50 m depth) between 1960 and 1963. In 1914, an additional twenty deeper diamond drill holes were added, ranging from 110 to 550 m depth.

In 2012, the British exploration company Kodal Minerals Plc conducted 918 meters of additional drilling on seven diamond drill cores, using a BQTK core barrel size (which corresponds to a 40.7 mm core diameter with a 60 mm hole diameter) in order to verify the historical drill data (Kodal Minerals Plc, 2014).

The drill data provided valuable insights into the Kodal deposit, which has limited outcrop exposure due to a densely wooded surface (Lindberg, 1985). For the first time, the structure of the ore body was described, and some evaluations of the underground potential were conducted. These assessments aimed to consider the possibility of an open-pit mining approach in 1975 or an underground mine in 1983 (Bergstøl, 1972; Lindberg, 1985).

In recent times, the economic potential of the Kodal deposit has significantly increased, especially given the imperative to reduce the supply risk of critical raw materials in Europe. Several studies have succeeded in shedding light on the exceptional concentration of phosphate and heavy metals contained in the Kodal deposit (Ihlen *et al*., 2014; Decrée *et al*., 2022).

3. Geological setting

3.1. Oslo Rift

The Oslo Rift is located along the southwest margin of the Fennoscandian Shield in southeast Norway (Figure 1). Formed in the period from late Carboniferous to early Triassic (305-240 Ma), it is part of a network of rifts or graben that extends into the Skagerrak-North Sea-Norwegian-Greenland Sea and surrounding regions (Ziegler, 1978, 1990; Ro & Faleide, 1992; Neumann *et al.*, 1992; Rämö *et al.*, 2022). Located in the foreland of the Variscan orogen, it appears that the Oslo rift was mainly a consequence of regional stretching and thinning of the lithosphere (Neumann *et al*, 2004; Corfu & Dahlgren, 2008).

The Oslo Rift consists of two main segments: the Oslo Graben (Figure 1) and its southern extension into the North Sea known as the Skagerrak Graben (Ro & Faleide, 1992).

The onshore segment of the Oslo Rift is characterized as a typical narrow intercontinental rift (Buck, 1991; Rämö *et al.*, 2022), spanning 200 km in length and ranging from 35 to 65 km in width, cutting through the Precambrian complex. The basement comprises medium to high-grade metasediments, granites, and gneisses that were accreted to the Baltic Shield between 1800–1500 Ma (Berthelsen, 1980; Ro & Faleide, 1992).
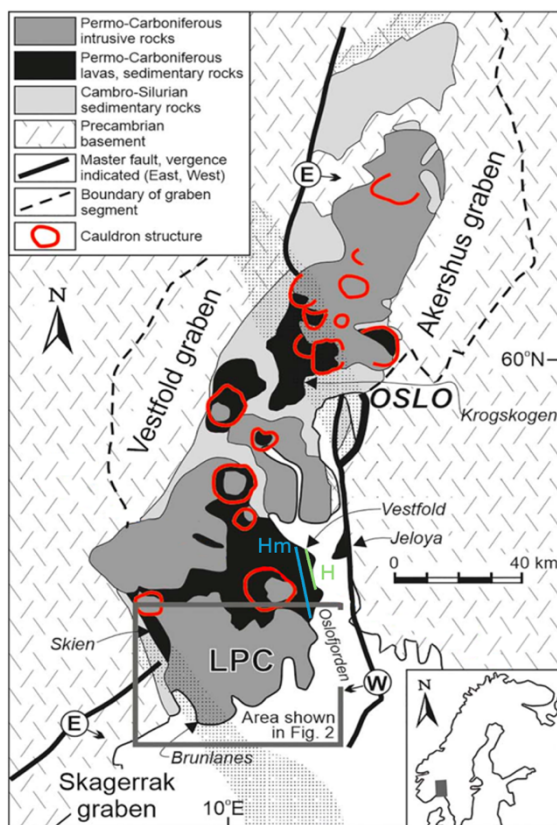
Figure 1. Simplified geological map of the Oslo rift modified from Brøgger and Schetelig (1923), Oftedahl (1960), Pedersen and van der Beek (1994) Corfu and Dahlgren (2008), Larsen *et al.* (2008) and Rämö *et al.* (2022). B1-basalts sequences: H = Horten, Hm = Holmestrand.

The earliest magmatic products of the Oslo Rift were dated at 300.4 ± 0.7 to 299.9 ± 0.9 Ma (Corfu & Dahlgren, 2008). Situated between the Vestfold and Skagerrak grabens (Figure 1), additional occurrences are observed in other areas along the flanks of the rift. These intrusions called "B1-basalts", are composed of alkaline mafic sills and dykes in Cambro-Ordovician sedimentary rocks. Following this period, extensive eruptions of rhomb porphyry lavas occurred, accompanied by their plutonic counterparts, over- to undersaturated monzonites (larvikites) and nepheline syenites (lardalite, foyaite; Annex 3). Larvikite magmatism is dated at 298.6 ± 1.4 to 292.1 ± 0.8 Ma by Dahlgren *et al.* (1996), using TIMS U–Pb zircon/baddeleyite ages (Rämö *et al.*, 2022). This stage appears to cover the longest duration in the evolution of the rift. The subsequent stage involved the formation of central volcanoes and calderas (Figure 1). These depressions were filled by clastic sedimentation. The youngest intrusions related to the Oslo Rift formation are large batholiths characterized by alkali syenitic to alkali granitic composition, notably developed at the north of the Larvik plutonic complex (Corfu & Dahlgren, 2008; Larsen *et al.*, 2008; Rämö *et al.*, 2022).

3.2. Larvik Plutonic Complex and northern intrusions

The Larvik plutonic complex is situated in the southern part of the Oslo Graben (Figure 1). It derives its name from the larvikite rocks, representing the largest occurrence within the complex (Brøgger, 1890; Rämö *et al.*, 2022). Larvikite is the traditional term used locally to describe augite syenite or monzonite composed of rhomb-shaped feldspar exhibiting a Schiller effect (Annex 3, Brøgger, 1890; Le Maitre *et al.*, 2002).

This complex formed between 296 and 289 Ma, offers valuable insights into the evolution of igneous activity as it covers almost the whole width of the rift system (Petersen, 1978; Rämö *et al.*, 2022). Petersen (1978) proposed that the complex is comprised of a succession of ten circular intrusions exhibiting unilateral younging towards the west (Figure 2). He derived this ring structure from topographic features, magnetic anomalies, and field observations, including chilled margins that delineate the extremities of the rings.

The oldest ring intrusions, situated at the easternmost part of the complex, exhibit quartz-bearing monzonite and tønsbergite, a red, quartz-bearing larvikite (rings I, II in Figure 2; Annex 3; Oftedahl & Petersen, 1978; Neumann, 1980; Rämö *et al.*, 2022). Rings III and V consist of monzonite lacking quartz and nepheline, while rings IV, VI through VIII are characterized by nepheline-bearing monzonite (Barth, 1945; Oftedahl & Petersen, 1978). The rock compositions gradually become silica-undersaturated, culminating in the youngest intrusions, rings IX and X, primarily composed of nepheline syenite (locally referred to as lardalite), some of which also contain sodalite (Figure 2; Oftedahl & Petersen, 1978; Neumann, 1980; Dahlgren, 2010).

The Larvik plutonic complex also contains historical mineralised bodies of apatite-magnetite-clinopyroxenite, locally referred to as "jacupirangite" (Kodal, Kjose, Larvik in Figure 2; Annnex 3; Brøgger, 1933; Bergstøl, 1972). It appears that all known occurrences of Fe-Ti-P ores in the complex are associated with intermediate to felsic magmatism, especially in proximity to the contact of distinct nepheline-monzonite (larvikite; Lindberg, 1985, Ihlen et al., 2014). While several areas have been investigated, only the Kodal deposit shows any economic potential as it remains the largest occurrence of Fe-Ti-P mineralization in the Larvik plutonic complex (Lindberg, 1985).

An innovative study conducted by Wang *et al.* (2024) used a machine learning program to locate new Fe-Ti-P-REE mineralization in the Larvik plutonic complex and its northern area, covering a total of 2000 km^2 area. Based on high-resolution geophysical and topological data, they successfully identified new Fe-Ti-P-REE enriched locations. Three primary regions of interest were highlighted on the generated prospectivity map (Annex 4): the Siljian area located at the northwest of the Kodal deposit, the contact between the monzonite/syenites and the B1-basalt which are the earliest magmatic products of the Oslo Rift, and finally, approximately 1 km directly south of the Kodal deposit, a mineralization roughly parallel with the same extension as the historical deposit (Figure 2, Wang *et al.*, 2024).

These new discoveries are related to the younger Siljan-Hvarnes intrusions, located at the north of the Larvik plutonic complex rings (SHI in Figure 2). These intrusions, primarily composed of monzonite to quartz-bearing syenite, were formed between 277 and 281 Ma (Pedersen, 1995). Recent dating of the Kodal deposit has shown ages more closely aligned with these northern intrusions than with the older Larvik plutonic complex. (personal communication, N. Coint).
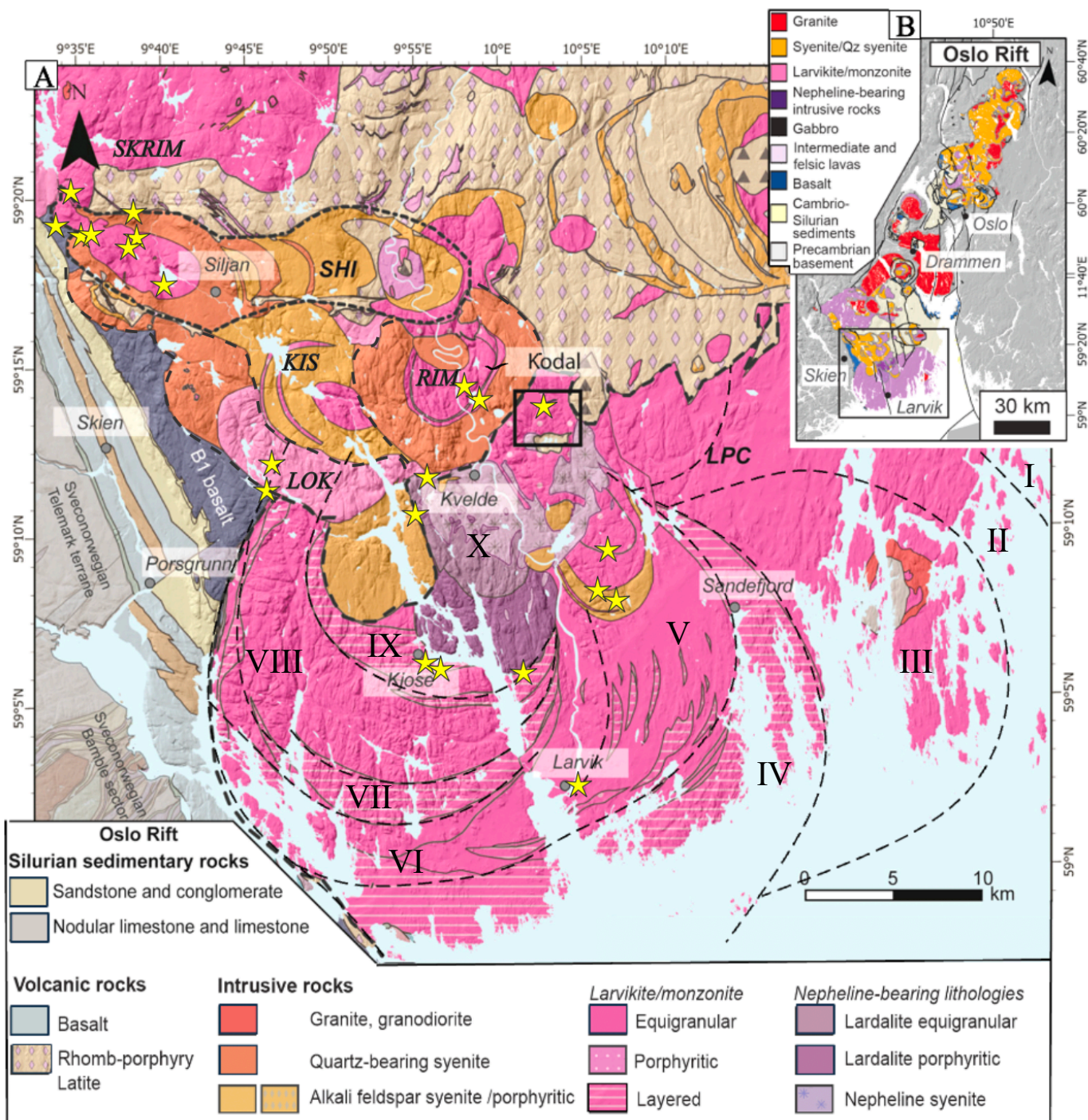
Figure 2. **A**. Simplified geological map of the study area featuring the Larvik plutonic complex along with northern **B**. Simplified geological map of the Oslo rift used to locate the study area (black rectangle) modified from Petersen (1978), Lindberg (1985), Wang *et al.* (2024) and Mansur *et al.* (in preparation). LPC = Larvik plutonic complex, SHI = Siljan-Hvarnes intrusions, KIS = Kiste intrusion, LOK = Løkka intrusion, RIM = Rimstad intrusion, SKRIM = Skrim intrusion. The yellow stars represent Fe-Ti-P occurrences. The Kodal deposit is framed in black.

3.3. Kodal deposit

The Kodal deposit is situated in the northern part of the Larvik complex at the limit with the younger Siljan-Hvarnes instrusions (Figure 2). It is composed of a succession of ultramafic apatite-ilmenite-magnetite-clinopyroxenite ores lenses contained in nepheline-bearing monzonite (larvikite) intrusions (Figure 3; Bergstøl, 1972; Lindberg, 1985). This series of lenses of varying size and shape is about 1900 m long and 20 m wide and at least several meters deep (Figure 3; Bergstøl, 1972). The deposit has an approximately east-west elongation with a general dip of 70–80° toward the south (Bergstøl, 1972; Lindberg, 1985).

Based on the whole rock geochemical analyses done on the cores, a disseminated ore area was emphasized extending up to 100 meters away from the lenses (Figure 3; Bergstøl, 1972; Lindberg, 1985). The average results indicate that the host monzonite contains 1.33 wt.% P_2O_5, 12.3 wt.% Fe_2O_3, and 2.4 wt.% TiO_2, while the disseminated ore exhibits 2.7 wt.% P_2O_5, 19.1 wt.% Fe_2O_3, and 4.18 wt.% TiO_2, and the massive ore shows 7.3 wt.% P_2O_5, 44.7 wt.% Fe_2O_3, and 8.63 wt.% TiO_2. (Miranda *et al.*, 2023). The disseminated zone mostly differs from the monzonite by an increase in Fe-Ti oxides and apatite present as bands or round-shaped pockets, reaching thicknesses of up to a few centimeters (Lindberg, 1985; Miranda *et al.*, 2023). The contact between the disseminated and massive ore exhibits variabilities, characterized by either a progressive increase in apatite and magnetite or, more frequently, the presence of a sharp contact between the two (Annex 5; Miranda *et al.*, 2023).

The Kodal deposit is intersected by several younger dykes with two distinct compositions: camptonite and syenite rhomb-porphyry (Annex 6). The dykes are characterised by pegmatitic potassic feldspar and brownish-purple pegmatitic hornblende crystals, which occasionally appear pale green (Annex 5). Most of these dykes exhibit a north-south (N-S) orientation, while a single rhomb-porphyry dyke has a northwest-southeast (NW-SE) direction (Figure 3; Bergstøl, 1972).
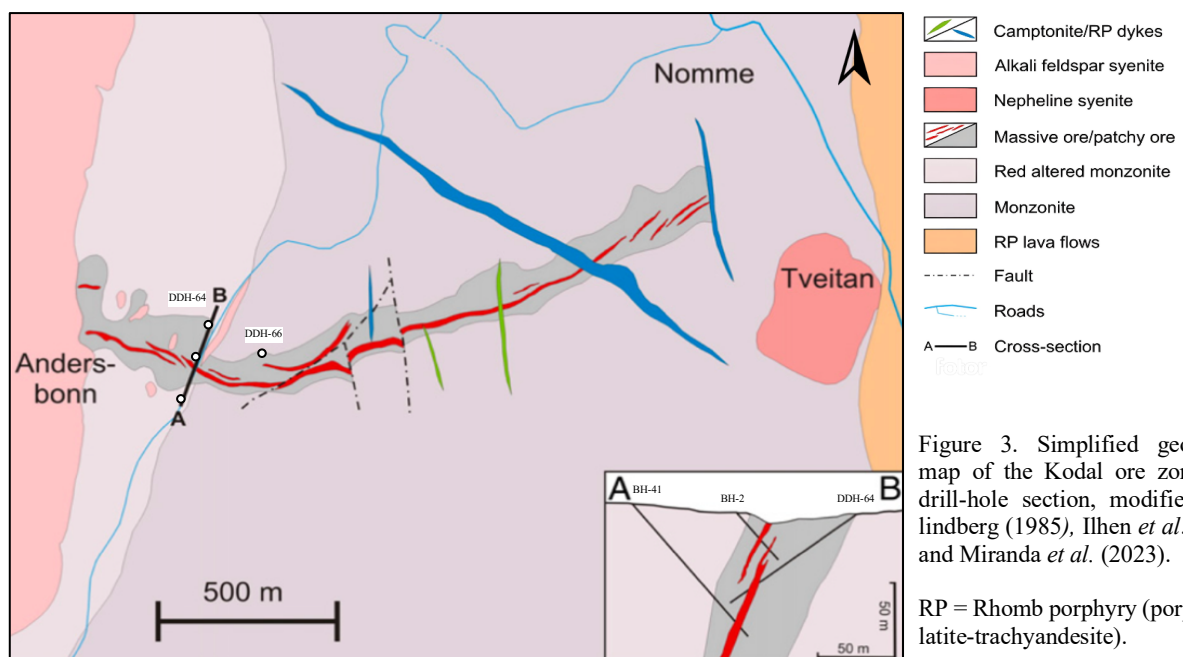
Figure 3. Simplified geological map of the Kodal ore zone with drill-hole section, modified from lindberg (1985*),* Ilhen *et al.* (2024) and Miranda *et al.* (2023).

RP = Rhomb porphyry (porphyritic latite-trachyandesite).

4. Kodal orebody genesis

The Kodal deposit has been the subject of several studies, some of which have attempted to identify the formation processes of the Fe-Ti-P and REE mineralization. Three main hypotheses have been proposed: intrusion of iron and phosphorus-rich melt liquid previously segregated by liquid immiscibility from the monzonitic magma (Bergstøl, 1972); in-situ fractional crystallization accumulation (Peterson, 1978); and crystallization of apatite and Fe-Ti oxide at depth prior to ascent (Andersen and Seiersten, 1994). These hypotheses are delved into deeper in the following paragraphs.

Bergstøl (1972) proposed the first crystallization model for the Kodal deposit based on diamond drill core data and field observations. He hypothesized that alkali feldspar and pyroxene were the first minerals to crystallize, leaving behind a monzonitic magma with a high phosphorus concentration. This change in liquid composition likely caused a reduction in the melting point due to the expansion of the liquid immiscibility field (Philpotts, 1967). As a result, an iron oxide-apatite-rich melt would segregate and likely migrate to the lower part of the magma chamber, along with previously crystallized pyroxene. Ultimately, a tectonic event is believed to have injected the partially crystallized magma through the not fully consolidated monzonitic rocks of the Kodal area (Bergstøl, 1972). Subsequent studies revealed that euhedral to subhedral apatite crystallized during the early phases, along with clinopyroxene, predating the titanomagnetite intercumulus (Petersen, 1978; Andersen & Seiersten, 1994).

While Bergstøl (1972) suggested a dyke-like structure for the ore body at Kodal, Petersen (1978) proposed a fractional crystallization process from the monzonitic magma that would have led to the accumulation of apatite and Fe-Ti oxides. He observed locally graded igneous lamination in the monzonite of the Larvik plutonic complex and occasional minor ore bodies that appear to fill depressions. In the case of the major ore bodies of Kodal, it seems to share similar characteristics with the surrounding monzonite such as fabric orientation, appropriate mineralogical composition, and lens shape (Petersen, 1978).

In support to the physical accumulation hypothesis, Lindberg (1985) observed asymmetrical shapes of massive ore lenses. The footwall contacts exhibit sharp boundaries, while the hanging walls show gradational characteristics, predominantly incorporating feldspar upward (Annex 7; Petersen, 1978; Lindberg 1985).

Andersen and Seiersten (1994) proposed a third scenario for the crystallization evolution of the Kodal ore. This scenario entails initial crystallization at depth in a magma chamber in the middle or lower crust, succeeded by a second stage involving the ascent of apatite and Fe-Ti oxide to shallower crustal levels. The crystallization history is derived from mineralogical assemblage and fluid inclusion data found in apatite and pyroxene suggesting that early mineral phases have crystallized at pressure averaging 5 to 8 kbar.

As no consensus has been reached yet, the genesis of the Kodal deposit remains to be fully explored. In this study, for the first time on the Kodal deposit, we investigated the petrography of polycrystalline melt inclusions hosted in apatite crystals.

5. Melt inclusions

The potential of melt inclusions as distinctive petrologic indicators has long been recognized, as they contain small pockets of melt trapped in crystals during their growth (Sorby, 1858; Kent, 2008). The information within melt inclusions is unique, recording a range of melt compositions that are largely isolated from interactions with the external environment (Kent, 2008). Nevertheless, the amount of preserved melt is minuscule compared to the magmatic system that produces them.

The most common host phases used for the study of melt inclusions are olivine, plagioclase, apatite, clinopyroxene, and orthopyroxene (Kent, 2008; Latypov *et al.*, 2024). Apatite is an ideal host for melt inclusions due to its lack of prominent cleavage and its chemical composition (Jacobsen *et al.*, 2005). Two types of melt inclusions can be identified: glassy melt inclusions, quenched in plutonic rocks, and more commonly, crystallized melt inclusions characterized by an assemblage of crystalline daughter mineral phases.

Fully crystallized melt inclusions have mostly been described in tholeiitic rocks using two methods: estimation of bulk composition based on daughter phases or re-homogenization to obtain a glass composition. Most of the time, a wide composition range is observed, as in the various cumulate phases of Skaergaard (East Greenland; Jakobsen *et al.*, 2005; 2011), Sept Iles (Canada; Charlier *et al.*, 2011), Bushveld Complex (South Africa; Fischer *et al.*, 2016), Baima (Southwest China; Liu *et al.*, 2014) and Panzhihua layered intrusions (Southwest China; Wang *et al.*, 2018). Melt inclusions in the most evolved cumulates of the Sept Iles layered intrusion exhibited a compositional gap between the Si-rich and Fe-rich melt inclusions, interpreted as evidence for silicate liquid immiscibility (Charlier *et al.*, 2011). Nonetheless, in most studies, the melt inclusions do not show a complete absence of intermediate compositions, and the silicate liquid immiscibility hypothesis has not been ruled out. Jakobsen *et al.* (2011) interpreted the continuous composition range as a result of heterogeneous trapping of both Fe-rich and Si-rich droplets in varying proportions.

The diversity in the composition of melt inclusions could also be due to other processes that alter the composition of the parental liquid (Kent, 2008). Anomalous melt inclusions can arise due to syn-trapping processes. In such cases, nuclei can be entrapped with melts, and melt inclusions may capture melts produced by boundary layers or other localized processes, resulting in compositions that deviate from the bulk rock composition (Kent, 2008; Latypov *et al.*, 2024). After being trapped, the melt inclusion may also re-equilibrate with its host or be affected by cracks, allowing interaction with the external environment and, as a result, expanding the range of compositions found within the inclusions (Kent, 2008).

The primary objective of this study is to determine whether silicate liquid immiscibility played a role in the genesis of the Kodal deposit. Melt inclusions are particularly valuable for this investigation as they provide a detailed record of the conditions and processes occurring within the magma. Unlike large-scale geological features, which may not preserve evidence of liquid immiscibility. Furthermore, liquid immiscibility has been recognized in other geological settings through the study of melt inclusions, making them a proven tool for identifying and understanding this phenomenon.

6. Silicate liquid immiscibility process

Silicate liquid immiscibility is the term used to describe the segregation of the magma in two melts during its cooling, one silica-rich while the other is iron-rich. This phenomenon was initially identified by Roedder and Weiblen (1970), who observed contrasting compositions of melt inclusions trapped in various phases in lunar cumulate rocks. For a long time, liquid immiscibility was principally debated for lunar rocks, and it has mostly studied in material sciences, particularly for its importance in glass and ceramics technologies (James, 1975).

However, liquid immiscibility has recently regained interest in petrogenetic processes due to melt inclusions that have documented liquid immiscibility in the Skaergaard intrusion, a classic suite of magmatic rocks (Jakobsen *et al.*, 2005). This study highlights the extent and petrogenetic significance of liquid immiscibility in tholeiitic and other common magmas (Veksler *et al.*, 2006). Presently, similar results have been highlighted in multiple slowly cooled enviroements thanks to melt inclusions record as discused in the previous section (Skaergaard in Jackobsen *et al.* (2011); Sept Iles in Charlier *et al.* (2011); Buschveld in Fischer *et al.* (2016); Penzhihua in Wang *et al.* (2018)). As the layered intrusions found in thoellitic compositionnal rocks shows similar iron oxide-apatite rocks, they will be the main comparaisent to the melt inclusions data collected on the Kodal deposit.

Liquid immiscibility has only been recognized in microscopic segregation, either as immiscible glass droplets in experiments or as distinct compositional melt inclusions in silicate and apatite crystals. Evidence from small-scale textures is often deemed insufficient to support the role of immiscibility as a large-scale differentiation process. Nevertheless, recent studies have revived the original idea of Daly (1914), attempting to explain the Daly gap, known as the dearth of intermediate magmatic composition at the Earth's surface. Indeed, in many tholeiitic provinces, the evolution from basalt to rhyolite is marked by a lack of compositions between these two liquids, such as monzodioritic melts along the evolution from tholeiitic basalt to A-type granite in Sept Iles intrusive suite (Quebec; Charlier *et al.* 2011; Namur *et al.* 2011). Fractional crystallisation alone does not account for the rapid evolution in liquid composition. Experimental studies have shown that silicate liquid immiscibility can occur during the liquid line of descent in many tholeiitic provinces, with the onset of immiscibility coinciding with the appearance of the Daly gap. This process results in the separation of liquids along the binodal curve, creating a compositional gap that becomes more pronounced as the temperature decreases (Charlier *et al.*, 2011; Charlier & Grove, 2012).

Principes of unmixing

The liquid line of descent is a graphical representation of the variation in the composition of a liquid during the differentiation of a magmatic body. Unmixing occurs when the liquid line of descent intersects the binodal curve, which defines the fields of liquid immiscibility in silicate melts. This phenomenon results in the formation of emulsified droplets of two different types of liquids: small, viscous, low-density Si-rich liquids and low-viscous, high-density Fe-rich liquids (Holness *et al.*, 2011). Depending on whether the liquid line of descent reaches the binodal curve near its closure (near the apex of the curve), the liquids produced will exhibit a narrower compositional gap. Additionally, at the onset of immiscibility, thermodynamics recquire that equilibrium immiscibility liquids crystallize identical mineral assemblages in different proportions, making the unmixing difficult to identify (Veksler *et al.*, 2007). Nevertheless, the evolution of the conjugate liquids along the binodal curve during cooling will expand the compositional gap (Charlier & Grove, 2012).

Below the binodal curve, the area defined by the spinodal curve is unstable, with no thermodynamic barrier to phase separation. In this region, even the tiniest fluctuations in composition and density will lead to spontaneous phase separation (Veksler & Charlier, 2015).

Two mechanisms govern phase separation: nucleation and growth, and spinodal decomposition. Liquids with compositions between the binodal and the spinodal curves will undergo separation via nucleation and growth, where small regions of a new phase form and then grow. On the other hand, when the liquid undergoes a (near-) instantaneous undercooling, the spinodal decomposition mechanism will lead to segregated phases within the spinodal curves, which are the metastable regions of the phase diagram (Shelby, 2005; Veksler & Charlier, 2015). Honour *et al.* (2019) also introduced the possibility that compositional heterogeneity, provoked at the boundary of crystals during their growth, could also trigger unmixing in the immediate surrounding liquid.

7. Samples

The samples belong exclusively to the last prospecting mission conducted by Kodal Minerals Plc in 2012. The Geological Survey of Norway, represented by Nolwenn Coint, selected and sampled five representatives from two distinct drill cores (DDH 64 and DDH 66; Figure 4). These samples, measuring approximately 15 cm in length and a quarter of a core in width (equivalent to 2 cm), were extracted from the massive magnetite-ilmenite-apatite-rich region, devoid of any discernible alteration or quartz fractures indicative of fluid circulation (Figure 4).

From core DDH64, three samples were studied at depths of 50.8, 55.5, and 71.4 meters, which correspond to samples Kodal 112 280, Kodal 112 281, and Kodal 112 282, respectively (for smoother reading, they will be referred to as K80, K81, and K81 in the rest of the work). Two supplementary samples were included from core DDH66 at depths of 110.5 and 122.2 meters, Kodal 112 279 (K79), and Kodal 112 278 (K78).
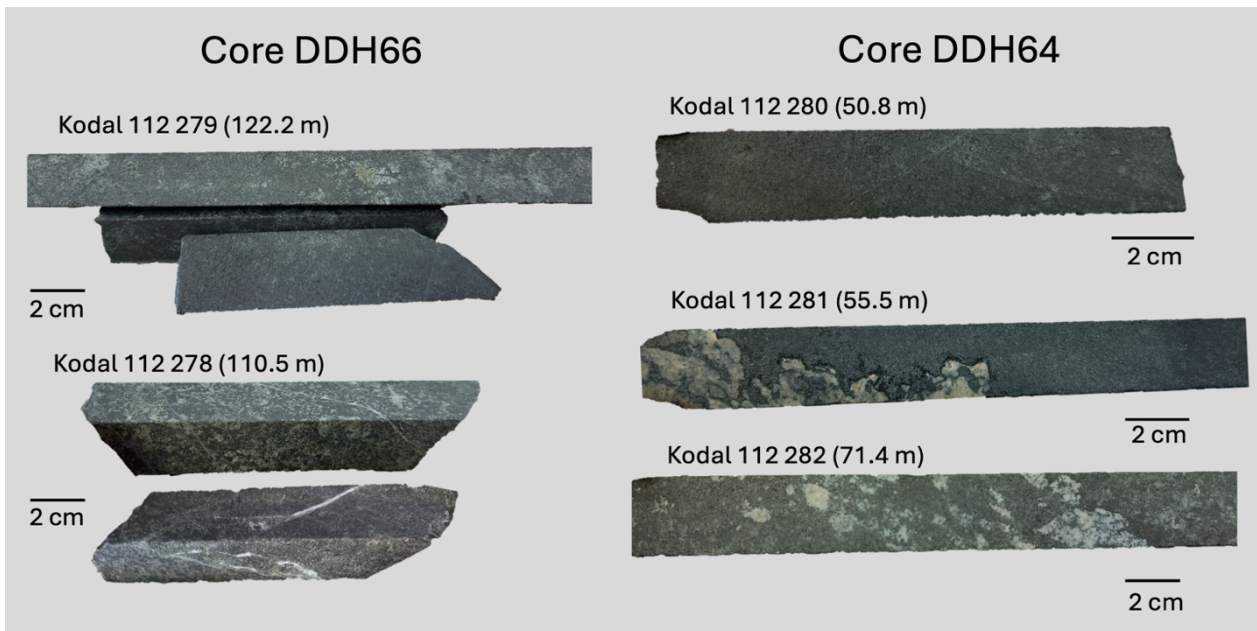
Figure 4. Photographs of the Fe-Ti-P massive ore cores from the Kodal deposit used for this study.

8. Methods

In the first stage, a qualitative study was conducted on the samples. From each of the five drill cores, several thin sections of different thicknesses (ranging from 30 microns to 1.3 millimeters) were prepared for petrographic and mineral analyses. All the samples were analyzed by scanning electron microscope (SEM) to determine the phases present in the apatite-hosted polycrystalline inclusions.

Subsequently, three samples were selected to undergo fragmentation. The objective was to recover single crystals of apatite without damaging the apatite crystals containing the polycrystalline inclusions. Electric pulse fragmentation, considered less harsh on crystals, was chosen instead of conventional crushing. The resulting single crystals were subsequently fractionated using various methods to separate the unfractured apatite crystals with melt inclusions from the other crystals present in the ore. The latter were then reheated and quenched

using a pressure vessel apparatus. This crucial step allowed the re-homogenization of the polycrystalline inclusions, resulting in a glassy texture. The composition of this glass was determined using the scanning electron microscope for the second time.

8.1. Ore fragmentation

The fragmentation of the core samples was conducted at the GEMME laboratory at the University of Liège using the SELFRAG Lab unit manufactured by SELFRAG AG, Switzerland (Annex 8). The procedure was carried out under the supervision of Mohamed Aatach.

8.1.1. Electrical fragmentation principal

Electric pulse fragmentation is a method that relies on high-voltage electric discharges of short duration, applied to rocks to weaken or fully fragment them. For this mechanism to be appliable, the solid material being fragmented should have multiple phases with distinct electrical properties. When these distinct constituents of the sample are subjected to a high electric field, they polarize, creating an imbalance of electric charges at the grain boundaries. The amount of charge that accumulates at the interfaces of the grains increases with the difference between the electrical properties of the grains (Andres *et al.*, 2001). This difference in charges, in an intense electric field, creates a discharge (plasma) locally, leading to thermal expansion followed by a radial shock wave. This succession of mechanisms fractures the rock at the interfaces between phases almost instantaneously (Annex 9; Andres *et al.*, 1999; Touzé *et al.*, 2017).

8.1.2. The Selfrag apparatus

In the SELFRAG Lab unit, the following operating parameters are set and can vary: the distance between the electrodes (10–40 mm), the number of pulses (1–1000), the pulse rate (1–5 Hz), and the voltage (90–200 kV).

The samples are put in the process vessel which is a cuve designed to process up to 1 kg of materials immersed in 4 liters of dezionized water (Figure 5). At the top of the process vessel, the working electrode will transmit the discharge through the process liquid to the ground electrode at the bottom of the vessel. The electrical discharges are generated by a Marx generator fed by a transformer (Figure 5, Peter van der Wielen *et al.*, 2013).
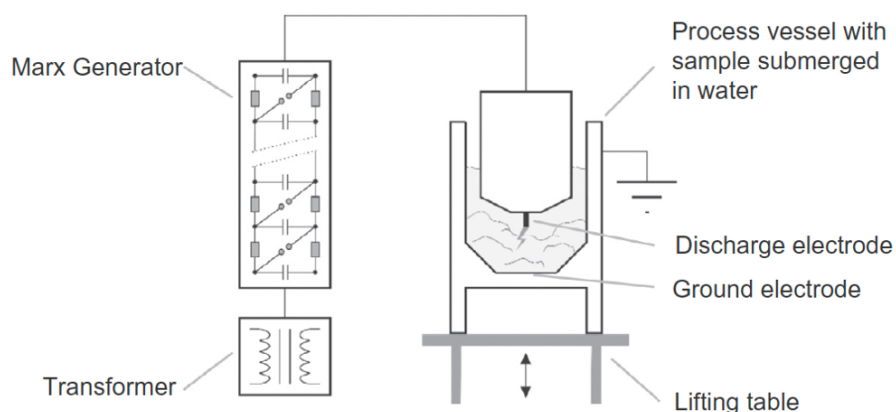
Figure 5. Schematic of the SELFRAG Lab unit from Peter van der Wielen *et al.* (2013)

8.1.3. Operating conditions

Based on the quality of the apatite crystals and the abundance of melt inclusions within them, three samples were selected to undergo Selfrag fragmentation. The process was conducted in two stages. Initially, the sample K79 was fragmented, and the separated grains were examined using a binocular. Subsequently, the parameters were slightly adjusted for the two additional core samples, K78 and K82. Furthermore, the magnetic section of sample K79 exhibited larger grain sizes after the initial fragmentation operation compared to the non-magnetic section. The magnetic section underwent a second round of fragmentation using the Selfrag system. For the sample K79, the majority of the apatite crystals were picked in the magnetic section. Two reasons could explain the magnetic proprieties of the apatite: firstly, in some cases, a thin layer of magnetite was still attached to the apatite, secondly, a majority of polycrystalline inclusions are rich in magnetite which can alter the physical proprieties of the apatite crystals.

The gap between the electrodes, the frequency, and the voltage were maintained constant for all experiments at 25 mm, 3 Hz, and 140 kV, respectively. For the first sample (K79), the number of pulses was set at 705, resulting in 681 discharges (Table 1). The granulometry of the sample was examined every 200 pulses. In the last three fragmentation attempts, the product was sieved every 100 pulses to prevent the re-fragmentation of the fraction with grain sizes under 150 μm. The operating parameters used for each experiment are detailed in Table 1.

Table 1. Selfrag equipment settings for the different samples

Samples	Electrode gap (mm)	No. of Pulses	Pulse rate (Hz)	Voltage (kV)	No. of discharges
Kodal 112 279	25	705	3	140	681
Kodal 112 279 magnetic section	25	705 + 300	3	140	681 + 280
Kodal 112 278	25	500	3	140	477
Kodal 112 282	25	400	3	140	397

8.2. Apatite separation

Once the core samples were fragmented, the non-fractured apatite crystals with polycrystalline inclusions had to be hand-picked one by one in order to be heated. Several processes were applied to increase the proportion of apatite in a smaller fraction. Firstly, only the fraction with grain sizes above 150 μm was retained. It was observed that the apatite crystals under 150 μm underwent fragmentation within the apatite itself, leading to fracturing of the apatite at the inclusion level (Annex 10). In the next step, magnetite grains were removed using a magnet, and the remaining fraction underwent separation using the Frantz magnetic separator (Annex 11). This device applies increasing electric currents (0.3 and 0.5 A) to separate magnetic materials. The non-magnetic fraction obtained at 0.3 A achieved the best balance, removing ilmenite and silicate crystals while retaining apatite crystals with multi-phase inclusions. However, the fraction obtained at 0.5 A contained more apatite crystals, but they were smaller and more pure, lacking inclusions.

Ultimately, only the apatite crystals from samples K79 and K78 from core DDH 66 were chosen for re-homogenization. As previously observed in thin sections, samples from core DDH 64 exhibited smaller and less abundant apatite crystals with melt inclusions. Picking apatite crystals from sample K82 was particularly challenging notably due to the presence of disseminated ore, which led to large grains of feldspar in the core.

8.3. Re-homogenization of melt inclusions

The re-homogenization of the melt inclusions took place at the Petrology, Geochemistry, and Petrophysics Laboratory of the University of Liège on the piston cylinder apparatus in a ¾ inch configuration, model MavoPress LPC 250-300/50, manufactured by Voggenreiter (Germany; Annex 12).

8.3.1. The piston-cylinder apparatus

The piston-cylinder apparatus is employed to create controlled high-temperature and high-pressure conditions to a sample, capable of reaching up to 2000°C and 4 GPa. Originally designed by Boyd and England in 1960, it drew inspiration from Coes' (1955) and Hall's (1958) earlier designs.

The piston-cylinder consists of four distinct cylinders stacked on top of each other, with a centrally positioned capsule containing the sample (Figure 6). This assembly is placed within the press, which applies pressure vertically from the upper and lower pistons onto the cylinders. The pressure of the two pistons is manually controlled using two independent hydraulic pumps. Initially, the upper piston (end-load) is pressurized, followed by the lower piston (master ram), the latter is monitored and continually adjusted as heating reduces the pressure. The sample is surrounded by a graphite resistance furnace that allows the circulation of the electrical current which will heat the sample. The electrical current is controlled by a tool heater that allows by a switch (on/off) to activate or deactivate the heating. A thermocouple placed in the cell assemblage permits to monitor the temperature of the experiment. In our setup, we used type D W–Re thermocouples which allows a 0.8% accuracy at 1000°C (Dunn, 1993).

i. The piston-cylinder

The piston-cylinder assembly comprises four cylindrical components: the base, the pressure vessel, the spacer plate, and the top plate. The base, being the lower cylinder, supports all the others. It is the thickest and heaviest cylinder, positioned directly on the lower piston. The base consists of two sections the cylindrical armature with in its center a cone-like inner part that
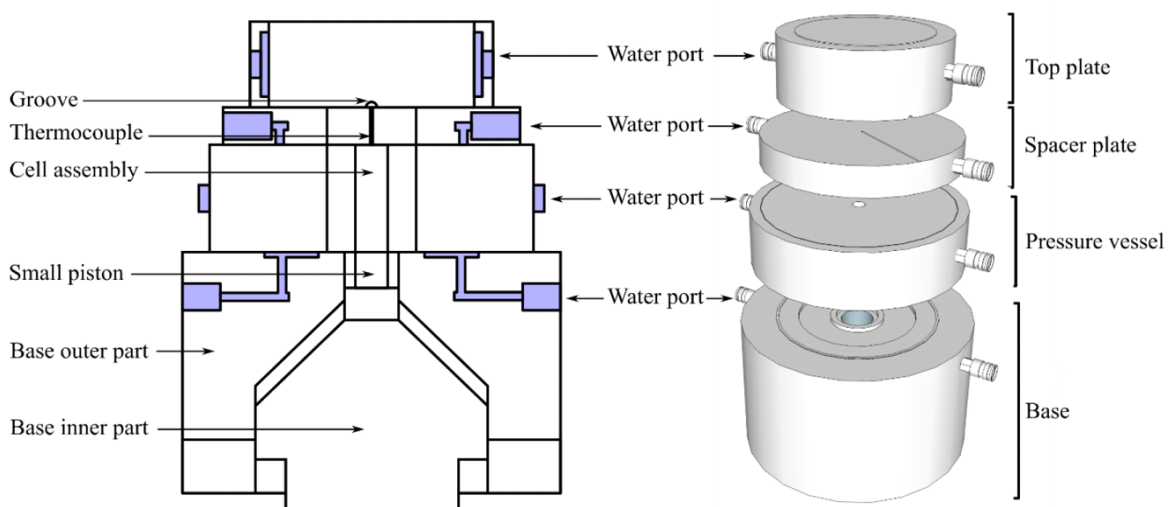
Figure 6. Schematics of the piston-cylinder apparatus from Pirotte (2023)

moves vertically within the outer part (Dunn, 1993). This conic shape allows the lower piston to transmit its pressure from a larger area to a smaller piston, which rests on the top of the base. As the area impacted by the pressure decreases, it is subjected to a significant multiplication factor that increases the pressure per unit of surface.

The small piston, in its turn, transmits pressure from the lower piston to the cell assembly situated at the bottom of the pressure vessel. The pressure vessel is the most crucial component of the piston-cylinder assembly. Positioned at the center of the assembly, it contains the cell assembly with the sample. The pressure vessel can be divided into two parts: the outer ring composed of stainless steel and the tungsten-carbide core, which directly contacts the sample (Pirotte, 2023). On the top of the pressure vessel sits the spacer plate, a plain stainless-steel cylinder with a hole in its middle. This hole accommodates the thermocouple, which crosses the spacer plate until reaching the sample in the pressure vessel. A plastic sheet is spaced between the pressure vessel and the spacer plate in order to center the assembly before pressurization.

Finally, at the summit of the assembly, the top plate is a thick cylinder made of steel, designed to support the pressure exerted from the upper piston. Before the start of pressurization, a sheet of Mylar is placed on top of the plate. This ensures that the apparatus and the press are electrically isolated, allowing the current to exit through the electrodes.

Each cylinder is equipped with two water ports that allow the cooling of the apparatus. We employ a closed cooling system, which utilizes a pump to cool the circulating deionized water.

ii.   The cell assembly

The cell assembly is composed of multiple cylinders made of various components that, when assembled, have a ¾-inch diameter to fit into the pressure vessel. At the center of the assembly lies the capsule containing the sample. The components forming the cell can vary from one experiment to another, but generally, the cell assembly consists of a cell, a furnace, a capsule, a ring, a wafer, a pedestal, and a sleeve (Figure 7, Annex 13).
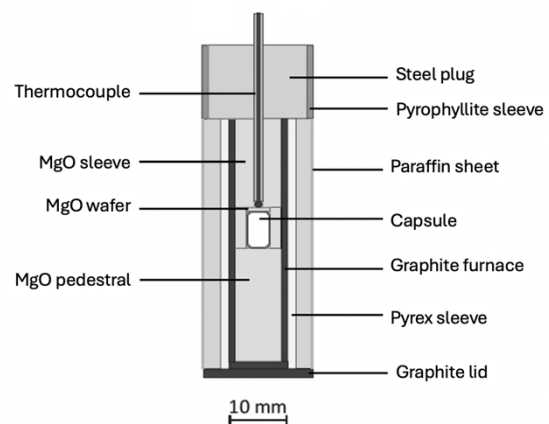
Figure 7. Piston cylinder cell assembly schematic modified from Condamine *et al.* (2022)

Two types of capsules were used in our experiments: palladium-gold (Pd-Au) capsules that have been sealed to encase the sample and graphite capsules topped with a graphite lid (Annex 14). The capsules were filled with apatite crystals mixed with a matrix (MgO or NaCl powder). The matrix serves a dual role: firstly, it fills any gaps in the capsule to prevent breakage during pressurization, and secondly, it prevents the apatite crystals from adhering to one another.

The capsule is then inserted into a MgO ring, which serves to electrically isolate the capsule from the furnace. On both sides of the capsule, three additional components of the assembly are also made of MgO: the pedestal, the sleeve, and the wafer (Figure 7). The pedestal is a plain cylinder, positioned beneath the capsule to provide support. Above the capsule sits the sleeve, similar in appearance to the cylindrical pedestal but distinguished by the hole running through

its center along its entire length. This hole will accommodate the thermocouple during the experiment. To prevent contact between the thermocouple and the capsule, and thus avoid any chemical reaction between the two, a 1.25 mm thick wafer, is placed between the MgO sleeve and the MgO ring containing the sample. The height of both the pedestal and the sleeve is crucial, as their role is to transmit the deformation caused by the vertically applied pressure onto the sample. It's essential for the sample to be positioned precisely in the middle of the assembly.

The MgO assembly is held together within a thin graphite tube known as the furnace (Figure 7). This conductive material facilitates the transmission of electrical current, which heats the graphite furnace. In turn, the heated furnace then raises the temperature of the capsule. Finally, the cell is the larger tube that encloses the entire assembly. It is constituted of high-purity talc containing a Pyrex cylinder, acting as an electrical insulator.

Once the assembly is put together, it is slid into the pressure vessel. To facilitate the sliding, a paraffin sheet is wrapped around the cell assembly, and the walls of the pressure vessel are coated with lubricant, typically MoS_2. Once the cell assembly is inserted, a thin graphite cylinder is placed beneath it. Its role is to ensure electrical connectivity between the furnace and the small piston. Finally, on the opposite side of the assembly, a steel plug surrounded by a pyrophyllite ring is inserted into the pressure vessel (Figure 7). It's role is to prevent contact between the steel and the tungsten carbide core (Pirotte, 2023).

8.3.2. Experimental setting

To start the experiment, the upper piston was pressurized to 500 bars, followed by the lower piston, which was maintained at 154 bars until the end of the procedure. The samples were heated up to 865°C at a rate of 100°C per minute. This temperature was maintained for 6 minutes, after which the heating speed was reduced to 50°C per minute until reaching 1100°C. The target temperature was maintained for 15 minutes before ending the experiment with an immediate quench, rapidly decreasing the temperature. It is important to note that the thermocouple reading will be approximately 25°C lower than the actual temperature applied to the apatite crystals due to the presence of the MgO wafer separating the capsule from the thermocouple.

A total of four experiments were conducted with the parameters previously mentioned, with variations only in the capsule materials and the composition of the matrix. For each of the core samples (K78 and K79), the hand-picked apatite crystals were initially mixed with MgO powder and then sealed in a Pd-Au capsule by welding the ends. For K78, approximately a 50-50 proportion between the matrix and the apatite crystals was used, resulting in a block of apatite crystals cemented together within the MgO. Ultrasonic cleaning bath and mortar and pestle were employed to detach the crystals (Annex 14). For the second attempt, the MgO quantity was increased, but the capsule underwent significant deformation, leading to the fragmentation of the apatite crystals. The last two experiments were conducted with graphite capsules and a NaCl matrix. This combination was more efficient and preserved the apatite crystals intact, as the NaCl could be easily dissolved in water, allowing the recovery of the apatite crystals.

Finally, the individual apatite crystals were mounted in epoxy using small brass tubes and then polished using sandpapers until the re-homogenized inclusions were exposed (Annex 15). To achieve a smooth surface for optimal microscope observations, the polishing process was concluded with a diamond solution polish.

8.4. The SEM and EDS

Scanning electron microscopy (SEM) analyses were conducted in two stages in this study. Initially, poly-crystalline inclusions in thin sections were analyzed at the University of Aachen in Germany using a "FEI QUANTA 650 FEG" SEM coupled with a "Bruker Dual X-Flash 5030 Detector" which is a double energy-dispersive X-Ray spectrometer. Subsequently, the re-homogenized melt inclusions, which were heated and mounted in epoxy, were analysed at the KU Leuven using a "TESCAN MIRA 4 FEG" SEM coupled with the "Ultim Max 65 energy-dispersive X-Ray detector" from Oxford Instruments (Figure 8).
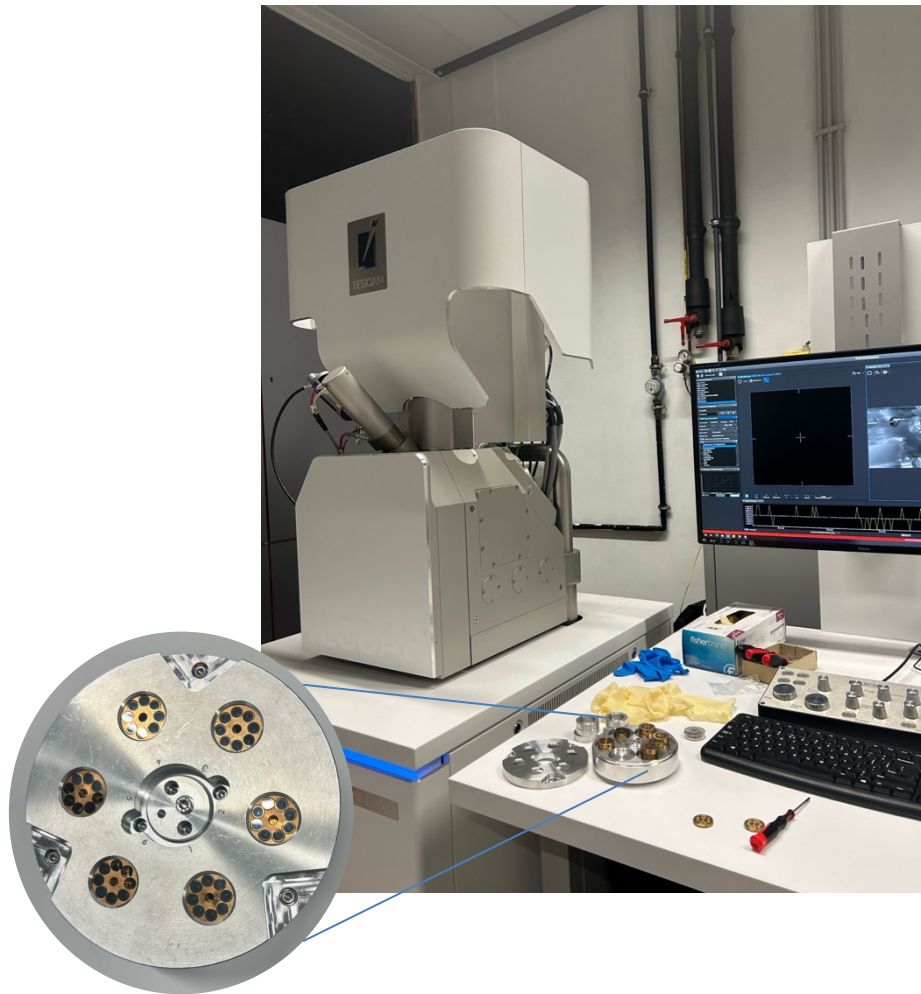
Figure 8. Photograph of the TESCAN MIRA 4 FEG scanning electron microscope device at KU Leuven. In the bottom left corner, a close-up view of the sample holder that will be inserted into the SEM is visible. This sample holder contains six wheels, each bearing epoxy-mounted apatite crystals.

In both cases, the sample is bombarded with a beam of electrons that interact with its atoms. As a result of this bombardment, various signals are reemitted with a small energy loss. These devices can detect secondary electrons and backscattered electrons, which are used to create an image of the sample. The flux of backscattered electrons produced by the sample correlates with the density of the different phases. Dense minerals, characterized by higher atomic numbers, emit more backscattered electrons and appear brighter in the generated image compared to lighter phases (Danguy & Quivy, 1956). The SEM is also coupled with X-ray detectors capable of performing Energy Dispersive X-ray Spectroscopy (EDS). These analyses enabled us to obtain qualitative imaging and semi-quantitative spectra in order to determine the different phases present in the polycrystalline and re-homogenised inclusions hosted in apatite crystals.

The operating conditions varied slightly between the different institutions. With the QUANTA 650F scanning electron microscope used for the polycrystalline inclusions, we proceeded with an acceleration voltage of 15 kV. The nominal beam current was set at approximately 1 nA, and a working distance of around 13 mm was maintained.

On the other hand, with the TESCAN MIRA 4 FEG scanning electron microscope used for the re-homogenized inclusions, the acceleration voltage was set at 20 kV, with a nominal beam current of approximately 1 nA and a working distance of around 15 mm. The EDS spectra and semi-quantitave compositions were analysed using the Oxford Instruments Aztec software.

Prior to SEM analyses, the samples were meticulously coated with a thin layer of carbon. This step is crucial to ensure electrical conductivity and prevent charging effects that could interfere with the electron beam's interaction with the sample. The carbon coating facilitates the smooth circulation of electrons on the sample surface, enhancing image quality and ensuring accurate analytical results.

9. Results

9.1. Petrography of the Kodal deposit

The petrography of the Fe-Ti-P mineralization at Kodal was primarily defined through thin sections prepared from the five cores samples selected by the NGU (Figure 4). Nevertheless, the Kodal deposit is divided into several entities, distinguished mainly by their chemical properties, including the monzonite-host rock, the disseminated ore, and the syenite dykes that intersect the deposit. Descriptions of these entities, especially the syenite dykes, are primarily based on macroscopic observations of core DDH66 and existing literature. I had the privilege of visiting the NGU's core facility during my stay in Trondheim. This visit allowed me to examine the different entities and their distribution within the core. All core photographs included in this study were taken during this visit.

9.1.1. The host rock

The monazite host is predominantly composed of grey to bluish coarse-grained feldspar, with minor interstice filled with fine-grained titano-magnetite, augite, and apatite (Figure 9A).
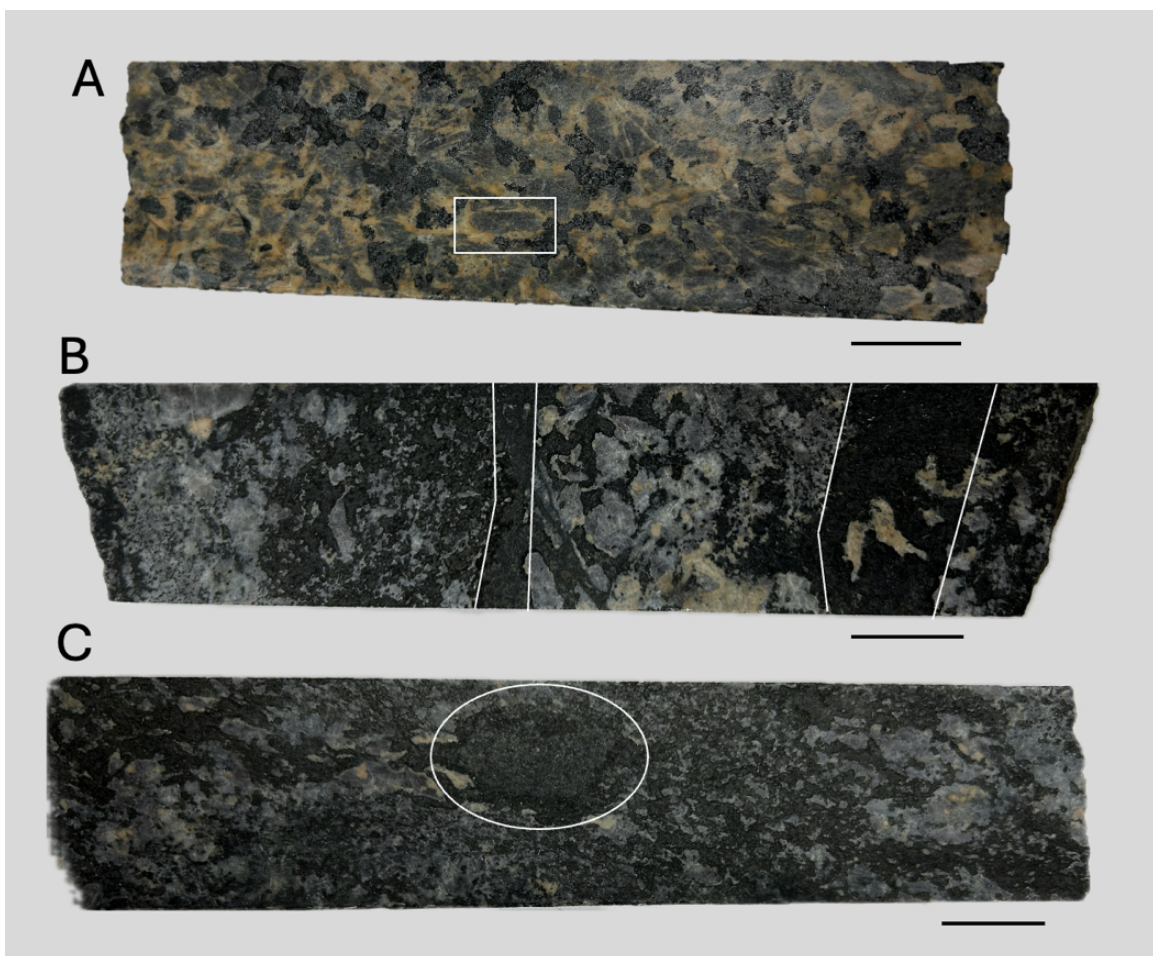
Figure 9. Core DDH66 of the Kodal deposit photography. **A.** Monzonite host within the white rectangle a representative bluish feldspar crystal with pale pink edges (12.3 m Depth). **B.** Disseminated ore with massive ore bands (29 m depth). **C.** Disseminated ore with encircled in white a rounded pocket of massive ore (22.3 m Depth). The black line is the scale measuring 2 cm for each sample.

Notably near the surface, the bluish feldspar often acquires a pale pink tint, which is more characteristic of the potassic feldspar found in the syenite dykes intersecting the deposit. Typically, only the rims of the feldspar crystals display this colour variation, possibly resulting from the late crystallisation of a more evolved magma, which favoured the formation of a more potassic feldspar (personal communication, Nolwenn Coint). Miranda *et al.* (2023) identified this colour change in the feldspar as weathered feldspar transforming into fine-grained sericite (Figure 9A).

9.1.2. The syenite dykes

The studied area is intersected by multiple younger dykes that are approximately perpendicular to the massive ore lenses. Most of the dykes are composed of syenite rhomb-porphyry, characterized by pegmatitic potassic feldspar with some phenocrysts reaching up to 5 cm in length, and euhedral brownish-purple pegmatitic hornblende crystals, which occasionally appear pale green (Annex 6 A-B, Bergstøl, 1972). Interstitial medium to fine-grained Fe-oxides are also present between the larger crystals. A sharp contact is observed between the dykes and the surrounding rocks, such as the jacupirangite ore or the monzonite host rock (Annex 6 A-B). Additionally, an unusually linear concentration of zircon is observed in the syenite, following the contact with the massive ore (Annex 6 C).

9.1.3. The disseminated ore

The disseminated ore closely resembles the composition of the monzonite host but exhibits elevated levels of Fe-Ti oxide and apatite. Within the disseminated ore, coarse-grained feldspar phenocrysts are often immersed in Fe-Ti oxides, primarily comprising magnetite with minor ilmenite. These oxides form interconnected interstices, occasionally developing into bands several centimetres thick (Figure 9 B). In other areas, the feldspar crystals are smaller, medium to fine-grained, creating an equigranular texture with the oxides. In those cases, the disseminated ore features small, rounded pockets of Fe-Ti oxides, measuring a few centimetres in diameter (Figure 9 C).

The contact between the disseminated and massive ore is sharp, appearing linear or delineating lobes (Annex 5). At the interface with the Fe-Ti oxides, feldspar and augite develop a ring of alteration, primarily composed of secondary biotite (Figure 10 A-B-C). This alteration is also observed in the massive ore area, forming few microns thick rings around medium-grained augite. However, it becomes more pronounced at the contact between the disseminated and massive ore, where the biotite alteration band can reach a thickness of one millimetre.

9.1.4. The massive Fe-Ti-P-REE ore

The massive ore is primarily composed of Fe-Ti oxides (mainly magnetite with some ilmenite), apatite, and augite. The magnetite is predominantly titano-magnetite, displaying exsolution lamellae of ilmenite (Figure 11). This texture results from an ulvöspinel phase within the magnetite that has oxidized to ilmenite (Bergstøl, 1972). However, approximately 20% of the magnetite grains are free of lamellae, suggesting the possibility of two generations of magnetite growth. Ilmenite also occurs as individual grains; some exhibit signs of oxidation, leading to the formation of rutile and hematite, referred to as hemo-ilmenite (Figure 11, Bergstøl, 1972).

Apatite crystals are present both as euhedral intercumulate grains and as inclusions within magnetite and augite crystals. While they are generally evenly distributed throughout the ore, apatite crystals tend to crystallise in contact with each other, forming linear arrangements. These crystals often concentrate at the interface with the disseminated ore, creating a sort of shield that progressively fade towards the massive ore (Figure 10 A-B). Additionally, monazite crystals enriched in light rare earth elements such as cerium, neodymium, and lanthanum, are identified at the edges of the apatite crystals and as inclusions within the apatite (Figure 6).

Two types of massive ore were distinguished based on the variable amount of augite. The first type, observed in deeper samples (core DDH 66), is characterized by medium-grained titano-magnetite, ilmenite, and medium to fine-grained apatite. Medium-grained augite is present in a highly altered state and is only found in limited concentrations in localized areas. The alteration involves the formation of fine-grained ilmenite within the augite crystals and the presence of large rings of secondary biotite; in some areas, the entire augite structure has undergone biotization.

Approximately 50 meters shallower, samples from core DDH 64 are characterized by smaller apatite crystals with the lowest concentration of melt inclusions. Medium augite crystals are more abundant and are disseminated in the ore as single sub-euhedral crystals surrounded by a ring of secondary biotite (Figure 10 D). This second type of ore is also characterized by the crystallization of titanite at the edges of the oxide interstices (Figure 10 A-B).

Modal analyses of the jacupirangite reveal the following variations: 15–24% apatite (an average of 30 to 40% was observed in this study's samples), 25–60% titanomagnetite, 5–15% high-magnesium ilmenite, 20–40% augite, 3–10% phlogopite, with minor amounts of magnesiohastingsitic hornblende, feldspar and carbonates (Bergstøl, 1972; Lindberg, 1985; Andersen & Seiersten, 1994; Ihlen *et al.*, 2014).
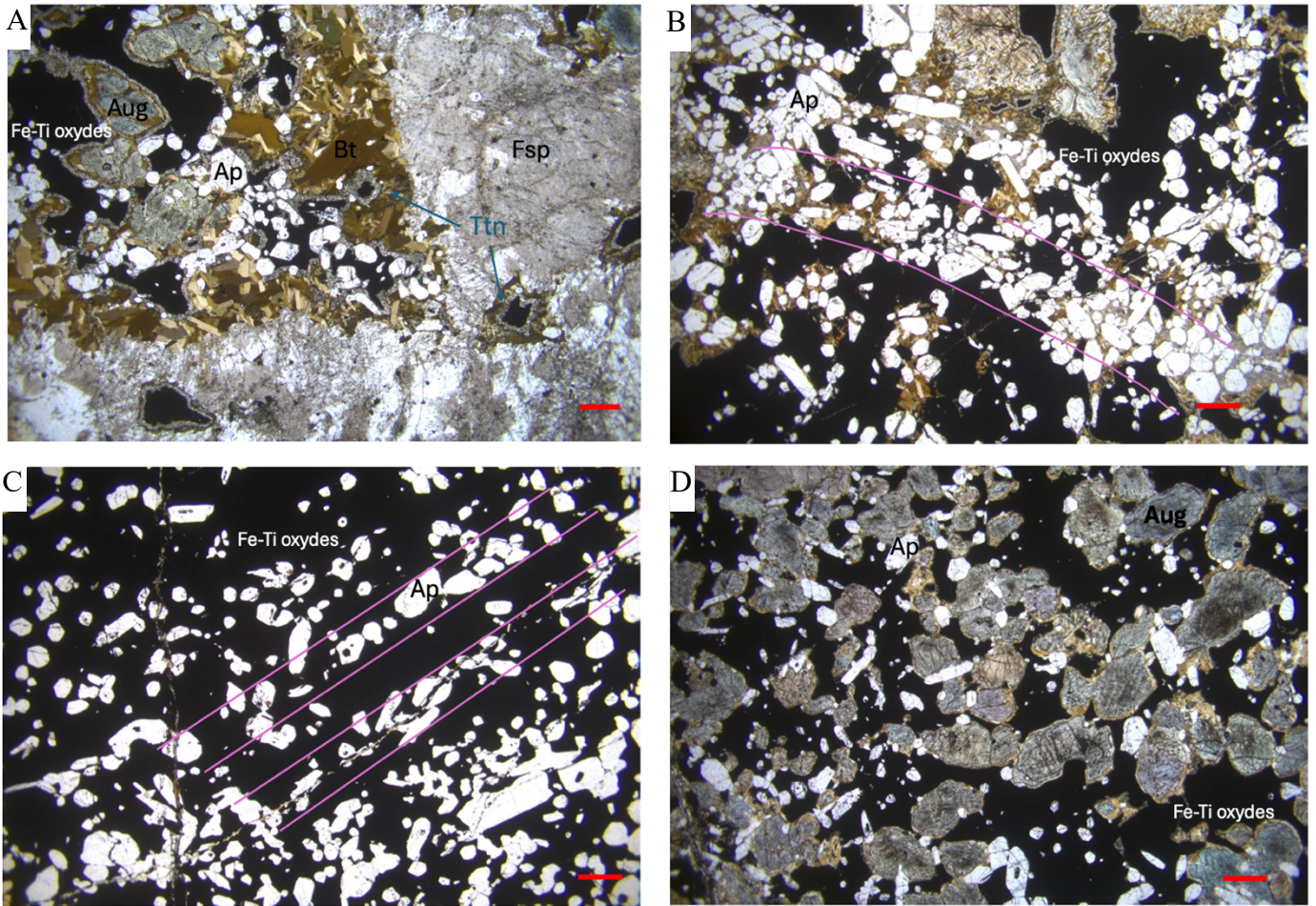
Figure 11. Transmitted light photomicrographs. **A.** Contact between the disseminated ore characterized by coarse-grained feldspar and the massive ore rich in Fe-Ti oxides, apatite, and augite crystals. The massive ore is locally characterized by a titanite corona and the shield-like structure created by the apatite crystals at the contact (Sample K82). **B.** Massive ore showing linear agglomeration of apatite crystals (Sample K81). **C.** Massive ore devoid of augite (Sample K79). **D.** Massive ore enriched in augite (Sample K80). The red line represents 200 μm.

Abbreviations: Bt = Biotite, Ap = Apatite, Aug = Augite, Ttn = titanite
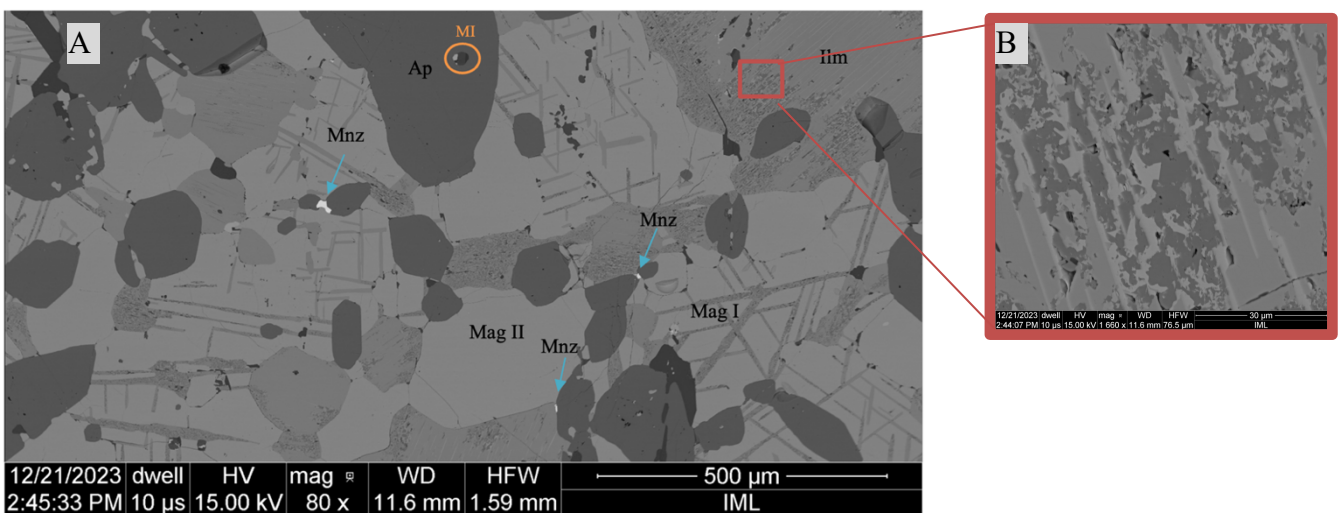
Figure 10. **A.** Back-scattered electron image of the Kodal ore deposit (K79) displaying the mineral assemblage, including apatite (Ap) grains containing poly-crystalline inclusions (MI) highlighted in orange, and monazite (Mnz). Two generations of magnetite are also observable: Mag I, characterized by ulvöspinel lamellae oxidized to ilmenite and Mag II. Ilmenite (Ilm) grains exhibit oxidation, transforming into rutile and hematite. **B.** Close-up view of the red square in picture A reveals the alteration process of ilmenite to hemo-ilmenite.

27

9.2. Petrography of the poly-crystalline inclusions

In the Kodal Fe-Ti-P mineralization, apatite grains are primarily present as single subhedral to euhedral crystals, ranging from 200 to 500 μm in length (Figure 12). They display sharp contacts with the surrounding crystals, which are mainly composed of Fe-Ti oxides such as magnetite and hemo-ilmenite. A sharp contact also exists between the apatite crystals and their hosted poly-crystalline inclusions. Typically, apatite crystals contain one or two inclusions, although the largest crystals can host up to five inclusions. Most apatite crystals do not contain inclusions, especially in the shallower samples from core DDH 64, where the apatite crystals are smaller and located at the edges of the mineralization, in contact with the augite-rich ore and the disseminated ore.
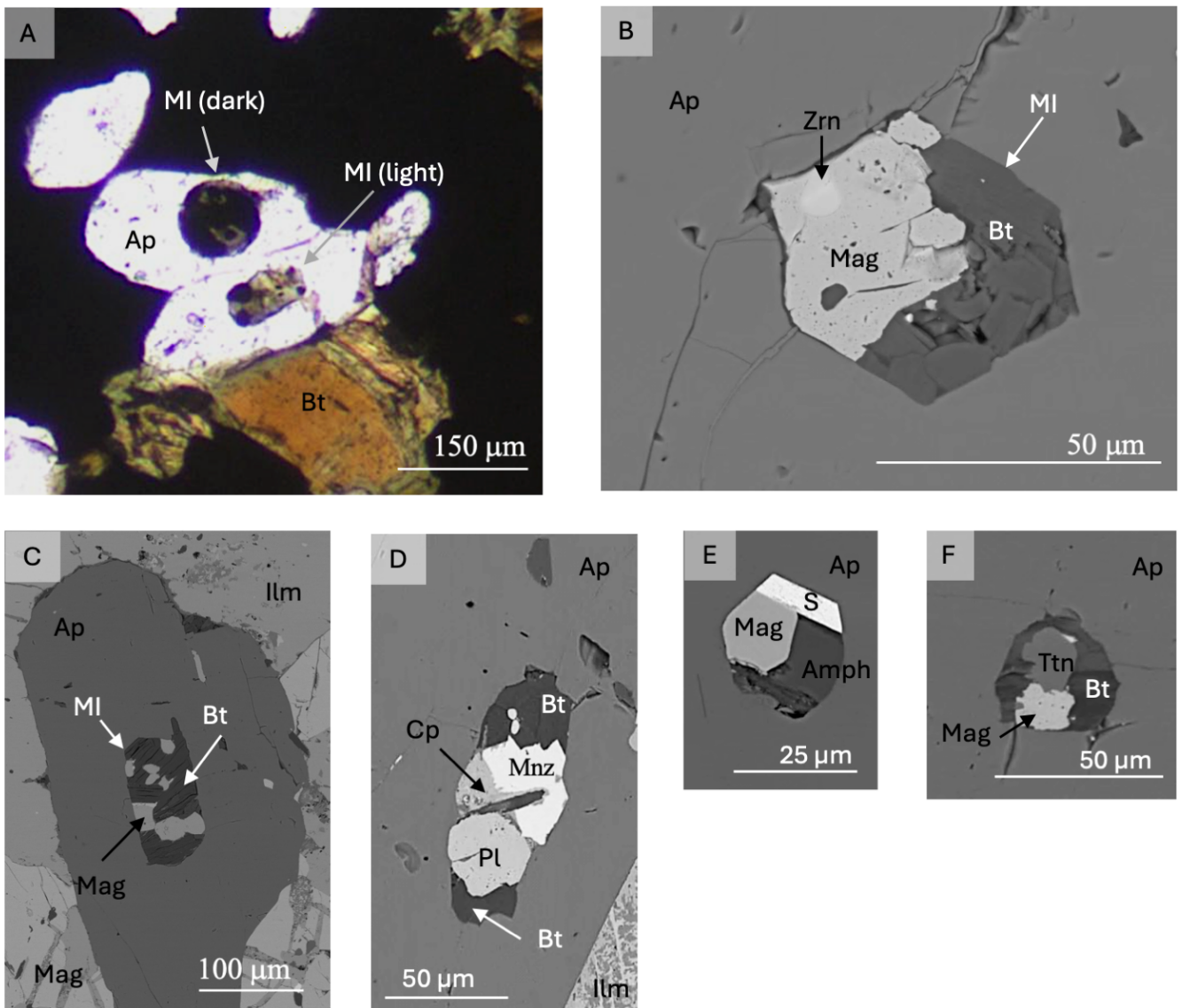
Figure 12. Poly–crystallized inclusions in thin sections (before heating). **A.** Transmitted light image showing two poly-crystallized inclusions, one is rounded and dark while the other one is elongated and lighter (sample K78). **B-C-D-E-F.** Back scatter electron imaging of poly-crystallized inclusions of respectively the samples K80, K78, K78, K79.

Abbreviations: MI = Melt Inclusion, Ttn = Titanite, Bt = Biotite, Ap = Apatite, Mg = Magnetite, Zrn = Zircon, Ilm = Ilmenite, S = Sulfur, Amph = Amphibole, Pl = Plagioclase, Mnz = Monazite, Cp = Clino-pyroxene.

The poly-crystalline inclusions exhibit rounded to elongated shapes and sometimes polygonal shapes, characteristic of the hexagonal crystalline system of apatite (Figure 12). They range from 20 to 120 μm in size and are composed of an assemblage of fully crystallized daughter phases. Two types of inclusions within the apatite crystals are distinguished: darker inclusions with a higher amount of Fe-Ti oxides and lighter inclusions richer in silicates (Figure 12 A).

The daughter phases present in the polycrystalline inclusions were determined using EDS spectra and semi-quantitative composition analysis (as shown in Annex 16). Biotite and Fe-Ti oxides are the most abundant phases in the polycrystalline inclusions. A significant proportion of the inclusions consists exclusively of an assemblage of small crystals of biotite and magnetite, with occasional ilmenite in varying proportions (Figure 12 C). However, other inclusions exhibit greater diversification with additional K-feldspar, Ca-amphibole, pyroxene, and plagioclase crystals. Minor phases such as zircon, chalcopyrite, pyrite, chlorite, titanite, sodalite, sulfur, and monazite are also locally observed (Figure 12 D-E-F).

To estimate the melt composition of the crystallized inclusions, two different methods can be applied. The first method involves analyzing the bulk composition of the daughter phases. However, this approach faces challenges due to the diversity of daughter phases, and their varying sizes. Additionally, the lack of three-dimensional information adds significant uncertainties to this method. The second method, chosen for this study, involves heating and quenching the melt inclusions in to obtain homogenized glasses with a unique composition for each inclusion. This approach provides a more reliable melt composition. As will be demonstrated in the next section, analyzing the overall composition of the inclusions without homogenization would have led to substantial errors, as the inclusions incorporated crystallized solid phases alongside the parent melts during trapping.

9.3. Re-homogenized melt inclusions

For this study, 79 homogenized melt inclusions were analyzed from 56 apatite grains from sample K79 (39 inclusions in 29 apatites) and sample K78 (40 inclusions in 27 apatites). These samples were exclusively extracted from the same core (DDH 66) at approximately 10 meters apart (K79 at a depth of 122.2 meters and K78 at 110.5 meters). We measured semi-quantitative compositions on the heated and then quenched melt inclusions using X-ray detectors coupled with the SEM at KU Leuven.

9.3.1. Characteristic of the re-homogenized inclusions

After heating and quenching, most of the melt inclusions exhibited unhomogenized textures, containing one or multiple residual crystal phases with no signs of shrinkage bubbles. Despite the non-homogeneous result, the textures and mineralogical assemblages before and after heating were different, indicating effective heating and providing valuable insights.

The heated inclusions containing residual crystals can be classified into three categories. The first category, from which almost all melt measurements are derived, is characterized by large residual crystals, often with Fe-Ti oxides adhering to the inclusion borders, and homogeneous quenched glass with a few immersed crystals (Figure 13 A). The second category appears to have retained all the original crystals with no significant signs of melting; the crystals are large, fully crystallized, and have well-defined edges (Figure 13 B). The third category features most of the time, a large crystal of Fe-Ti oxides, but the melted portion contains numerous microcrystals with no homogeneous texture (Figure 13 C).

The characteristics of inclusions from both the first and third categories encompass nearly all the inclusions studied, with a slight predominance of those falling into the third category, which lack distinguishable homogeneous melts. Notably, no significant distinctions were observed between samples K79 and K78. Furthermore, qualitatively similar characteristics are present in samples heated within capsules made of Pt-Au or graphite and matrices of NaCl or MgO.
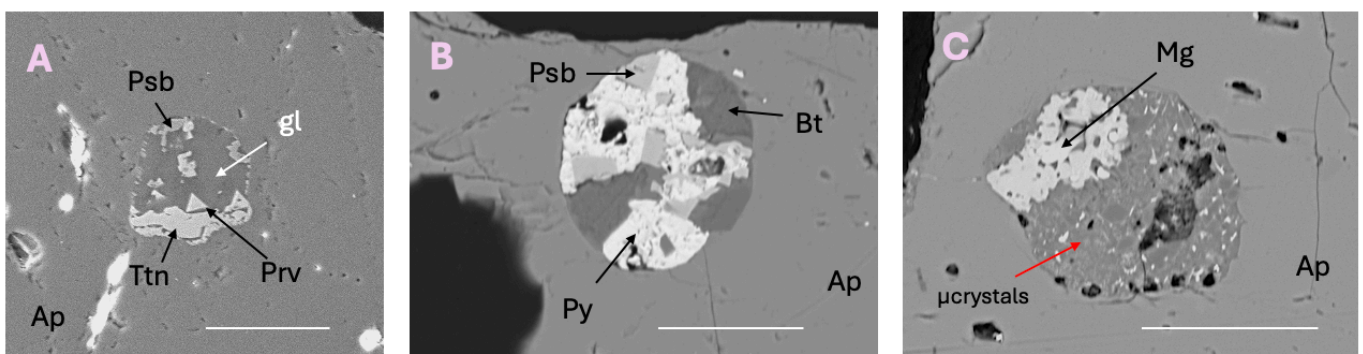
Figure 13. Back-scattered electron images of the heated apatite-hosted inclusions. **A.** Inclusions exhibit residual crystals surrounded by melts (sample 79-6). **B.** Inclusion that seems to have retained all the original phases present before heating (sample 79-7). **C.** Inclusion with residual crystals and an assemblage of microcrystals with non-homogeneous texture (sample 79-11). The bottom right white line represents the scale and corresponds to 50 μm.

Abbreviations: Psb = Pseudo-brookite, Ttn = Titanite, Prv = Perovskite, Bt = Biotite, Py = Pyrite, Ap = Apatite, Mg = Magnetite, gl = quenched melt.

The figure 14 shows two inclusions trapped in a single apatite crystal. The large inclusion, shown on the right, retains an inhomogeneous texture after heating, making it difficult to identify the glass composition. It contains multiple microcrystals of different types, including magnetite and silica. The smaller inclusion, on the left, is almost homogeneous, with only a small plagioclase crystal identified at its center. Since the smaller inclusion contains finer poly-crystalline phases, it may re-homogenize more quickly than the larger one. However, several factors could have contributed to the preservation of residual crystals in the apatite-hosted inclusions. These factors are detailed in the discussion section.
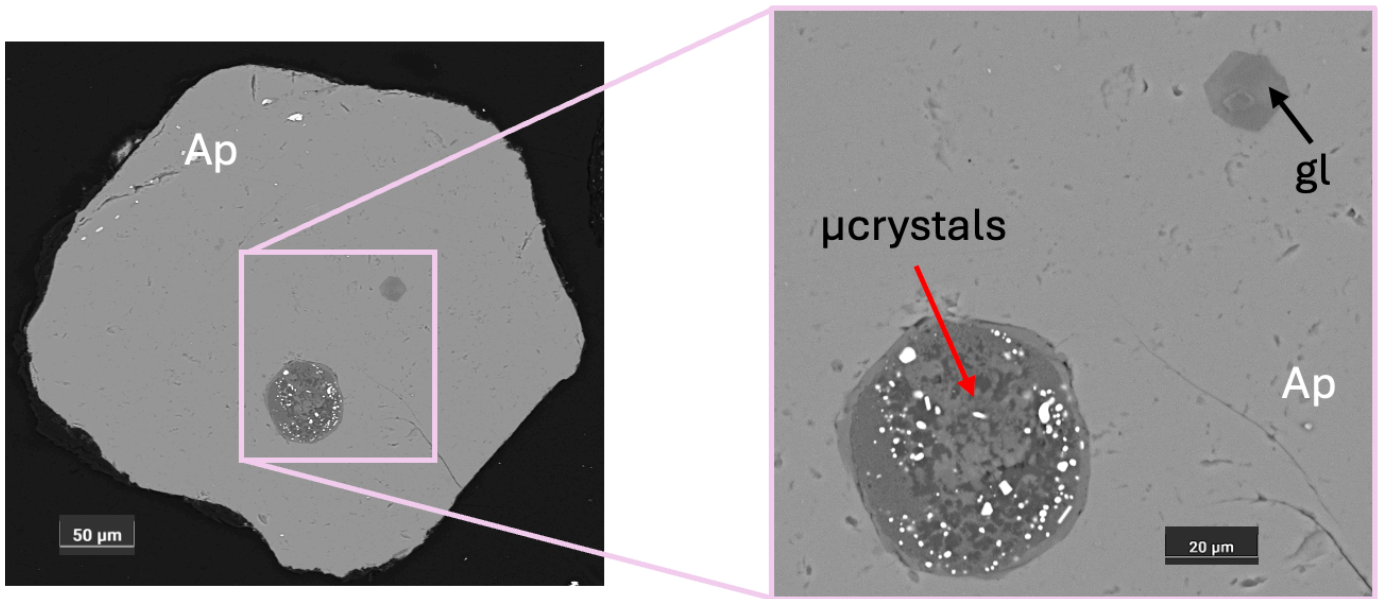
Figure 14. Back-scattered electron images of the heated apatite-hosted inclusion (sample 79-23), the lagger inclusion shows multiple phases after heating while the little inclusion shows a quite homogeneous texture. Abbreviations: Ap = Apatite, gl = quenched melt.

9.3.2. Compositions of the heated inclusions

In order to identify the melts and the residual phases, we measured a combination of dots and areas of the heated inclusions using EDS semi-quantitative compositions. Annex 17 is the list of all the compositions of minerals and melts measured in the inclusions, along with graphs highlighting the selected melt compositions compared to the other measurements. The diversity of phases still present in the heated inclusions made it challenging to determine the melt composition compared to the residual crystals.

i.   Residual phases determination

Residual crystals mainly consist of Fe-Ti oxides, including magnetite and ilmenite, which are preserved as large crystals localized at the edges of the inclusions (Figure 15 A-B-CI-E). Figures 12 B and 15 B show supposedly similar inclusions before and after heating, in which the magnetite covers half of the inclusions and contains a rounded zircon. This unchanged assemblage, with only a smoother contact noted between the magnetite and the silicic part, suggests that the large Fe-Ti oxide crystals were not affected by the heating, unlike the silicic part.

In addition to the larger Fe-Ti oxides, small crystals rich in Fe and/or Ti, identified as ferro-pseudobrookite, pseudobrookite, pyrite, and perovskite, appeared in the inclusions (see Annex 17 and Table 2). Typically, these single microcrystals surrounded by melt tend to cluster together at the edges of the inclusion (Figure 15 C-D-E). In contrast to the large Fe-Ti oxide crystals, these textures and compositions were not observed in the inclusions before homogenization.

Silicates are also preserved as residual phases in the heated inclusions. They appear as single medium to fine-grained crystals; some exhibit euhedral shapes with angular edges (Figure 15 B-D), while others have oval shapes with rounded edges (Figure 15 CIII–D–E). Similar to the oxides, they are surrounded by quenched glass and tend to cluster together. Most of the residual silicates are characterized by a higher MgO and CaO content than the surrounding melt (Table 2, Annex 17). The majority of the silica phases might be identified as amphiboles, as they exhibit a high Al_2O_3 content (highlighted in green in Table 2). However, it should be noted that these compositions are relatively depleted in SiO_2. Consequently, some measurement errors may have occurred due to the small size of the crystals.

Table 2. Heated poly-crystalline inclusion compositions of sample 79-5 (Figure 15 C), which contains three distinct inclusions (I, II, and III), each comprising different phases. The residual silica composition is highlighted in green, while the undetermined phases (n.d.) are highlighted in pink. These undetermined phases are characterized by an ensemble of microcrystals. For their measurement, an area-based analysis was performed using SEM coupled with an X-ray detector, instead of the usual dot-based analysis.

Core	MI no.	Phases	SiO_2 (wt.%)	TiO_2 (wt.%)	Al_2O_3 (wt.%)	FeO_{tot} (wt.%)	MnO (wt.%)	MgO (wt.%)	CaO (wt.%)	Na_2O (wt.%)	K_2O (wt.%)	P_2O_5 (wt.%)	Total (wt.%)
79	79-5 I-glass	n.d.	36,3	0,57	6,73	15,59	0,22	25,23	5,66	6,44	0,13	2,11	100
79	79-5 I-big	Magnetite	0,11	6,73	1,93	88,56	0,47	1,28	0,48	0,31	0	0,14	100
79	79-5 I-little	Pseudobrookite	3,5	7,95	11,99	63,23	0	11,03	1,12	0,82	0	0,37	100
79	79-5 III-h-light	gl (melt)	42,53	1,82	14,9	10,39	0,21	5,82	14,78	7,27	0,25	2,03	100
79	79-5 III-h-dark	Silica	40,16	1,02	9,23	12,53	0,38	21,71	8,43	4,69	0,15	1,29	100
79	79-5 II-light	titanite	15,05	33,75	4,02	2,04	0	7,86	31,83	2,91	0	2,54	100
79	79-5 II-h	n.d.	42,27	0,27	7,64	0,94	0	9,74	34,07	4,03	0	0,87	100
79	79-5 II-dark	Apatite	6,53	0	1,5	0,49	0	1,7	55,28	4,44	0,13	29,63	100
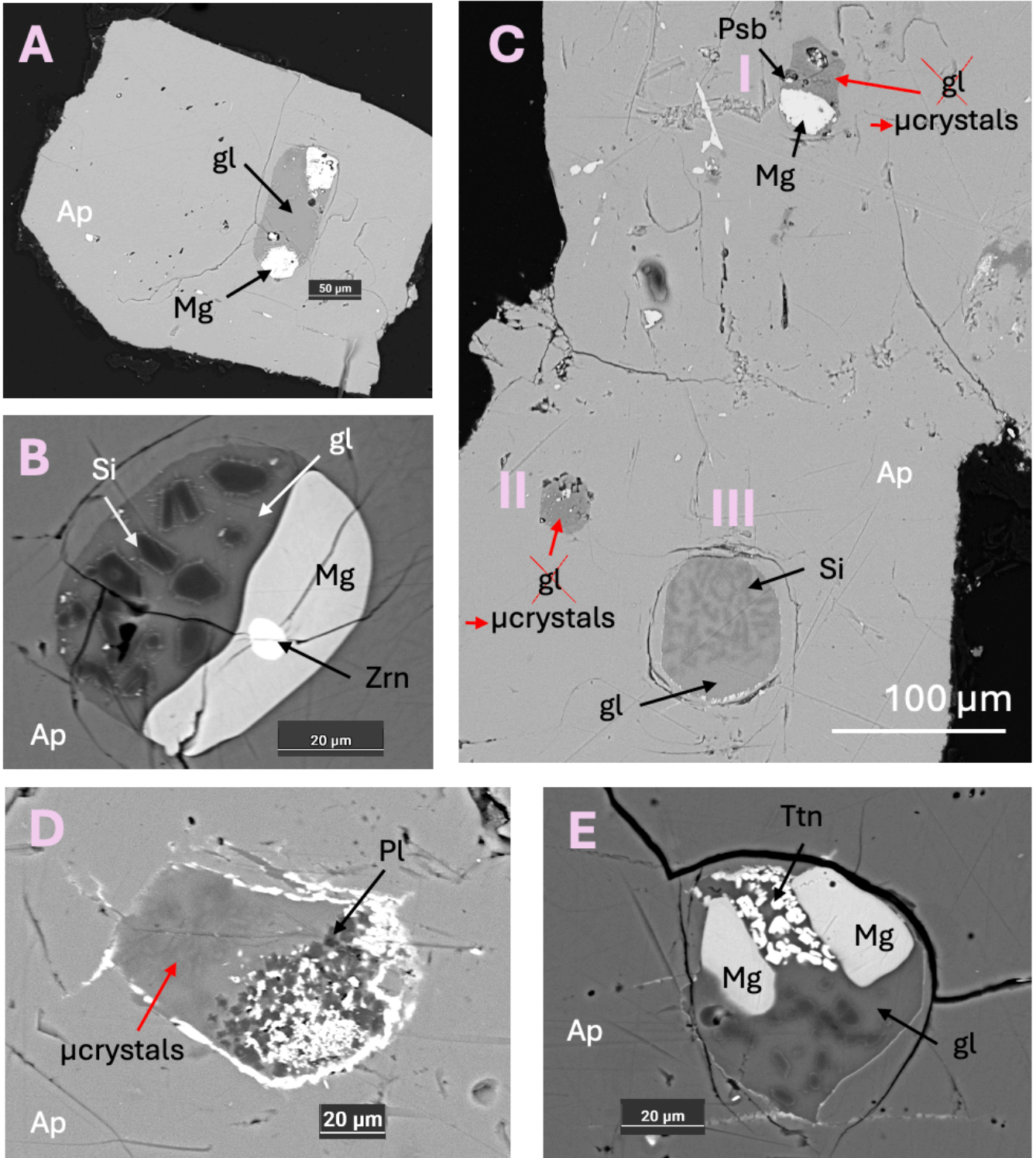
Figure 15. Back-scattered electron images of the heated apatite-hosted inclusion A. (Sample 79-8) B. (Sample 79-13) C. (Sample 79-5) D. (Sample 79-18) E. (Sample 79-3).

For melt inclusions with a non-homogenized texture, the melted part typically exhibits a homogeneous texture surrounding the other crystals (Figure 15 A-B-CIII-E). However, in some inclusions, the melted portion comprised multiple microphases, making the melt identification not visually obvious (Figure 15 CI-CII). In these instances, we measured areas instead of individual dots, resulting in compositions with higher MgO and CaO contents, likely due to the presence of silica microcrystals.

Ultimately, the inclusions displayed a wide range of compositions, with very high MgO content reaching up to 30 wt.% and almost 40 wt.% CaO (Annex 17). Melt compositions were determined based on visual aspects (absence of defined crystals, homogeneous texture surrounding residual crystals) and their chemical compositions. We ensured that the MgO and CaO content was not too high and that the P_2O_5 content was not null, assuming some melting from the apatite host during heating. However, this contamination was considered negligible. Calculations made by Fischer *et al.* (2016) following Harrison and Bruce (1984) equations, indicate that a melt with 40 wt.% SiO_2 at 1100°C would produce an increase of 3.96 wt.% P_2O_5, corresponding to only a 0.75 wt.% increase in CaO.

Finally, some larger crystals exhibited a homogeneous texture with no residual crystals. However, due to their high MgO content and low P_2O_5 content, they were preferentially identified as chlorite inclusions rather than melt inclusions. Annex 18 shows images of these inclusions along with a table detailing their compositions.

From the 79 melt inclusions analyzed, we focused our results on six key inclusions (three from sample K78 and three from sample K79), which were measured using dots instead of areas (highlighted in Table 3). To establish broader trends and provide a comprehensive view of the measured compositions, we incorporated an additional 23 melt inclusions into the dataset (Table 3). These additional compositions were predominantly measured using area methods, which introduces the possibility that residual microcrystals may have influenced the glass composition.

Melt inclusions cover a relatively narrow compositional range, 29–45.1 wt.% SiO_2 and 6.23–2.43 wt.% FeO_{tot} (Table 3, Annex 17) showing no compositional gap. Within the limited SiO_2 range, major elements exhibit quite dispersed values. However, some elements define notable linear trend. Specifically, MgO and P_2O_5 decrease with increasing SiO_2, while CaO, FeO_{tot}, and Al_2O_3 increase. The composition of the sample K79 shows a higher concentration of FeO_{tot} compared to the sample K78 (Annex 17). Notably, iron is the only element that exhibits a significant difference between the two samples. In contrast, the restricted selection defines an even smaller area of composition with no distinction between the different samples (K78-K79).

Table 3. Re-homogenized melt inclusion compositions. The highlighted rows are the selected MI within the larger selection.

Core	MI no.	SiO_2 (wt.%)	TiO_2 (wt.%)	Al_2O_3 (wt.%)	FeO_{tot} (wt.%)	MnO (wt.%)	MgO (wt.%)	CaO (wt.%)	Na_2O (wt.%)	K_2O (wt.%)	P_2O_5 (wt.%)	Total (wt.%)
K79	79-5b	42,53	1,82	14,9	10,39	0,21	5,82	14,78	7,27	0,25	2,03	100
K79	79-6	42,72	3,58	14,62	10,58	0,32	5,33	8,49	8,34	4,44	1,58	100
K79	79-8	41,91	1,66	17,85	12,01	0,3	5,32	11,55	2,79	4,42	2,19	100
K79	79-1a	24,89	2,71	12,24	16,96	0,17	14,69	12,38	7,91	1,68	6,37	100
K79	79-9	38,95	6,13	7,72	15,52	0,52	11,67	14,49	1,69	0,5	2,81	100
K79	79-11	29,92	1,45	9,42	18,77	0,26	10,38	11,31	7,36	5,35	5,78	100
K79	79-18b	33,09	0,56	5,89	22,43	0,43	21,7	9,12	3,77	0	3,01	100
K79	79-13	35,28	7,35	5,22	16,63	0,63	14,24	10,01	6,38	1,58	2,68	100
K79	79-21	33,84	10,16	7,97	19,66	0,3	7,47	14,63	1,12	0,97	3,88	100
K79	79-22	35,37	1,61	9,34	14,35	0,48	14,92	9,4	9,5	0,82	4,21	100
K79	79-23a	42,19	1,94	12,05	10,49	0,48	15,57	11,72	2,78	0,5	2,28	100
K79	79-26-h	35,35	1,21	7,12	12,76	0,08	20,97	11,94	6,8	0	3,77	100
K79	79-28	42,36	5,79	9,86	11,02	0,7	5,4	14,28	7,55	0,35	2,69	100
K78	78-1b	38,23	1,35	10,68	10,03	0	23,56	10,05	1,76	0	4,34	100
K78	78-6	43,39	2,24	15,65	7,02	0,14	13,77	9,61	3,66	3,15	1,37	100
K78	78-7	40,2	6,61	6,65	11,43	0,55	14,09	16,53	2,83	0	1,11	100
K78	78-8a	31,25	6,05	10,01	7,87	1,05	15,54	6,15	10,04	5,89	6,15	100
K78	78-9	34,16	4,86	5,73	14,2	0,82	22,04	5,27	5,84	3,16	3,92	100
K78	78-10	35,59	7,29	9,02	12,89	0,7	12,46	10,56	8,74	0,24	2,51	100
K78	78-1c-MgO	45,1	1,23	9,44	6,48	0,23	6,65	19,64	6,19	0	5,04	100
K78	78-1b-MgO	37,18	2,23	14,74	6,23	0,09	7,28	18,93	8,08	1,95	3,29	100
K78	78-1d-MgO	35,99	2,11	16,31	7,15	0,09	16,13	11,39	5,49	2,79	2,55	100
K78	78-2-MgO	38,76	5,07	10,73	12,41	0,73	7,26	15,9	3,62	1,78	3,74	100
K78	78-3-MgO	42,64	6,32	10,69	8,4	0,5	4,69	12,75	6,06	4,22	3,73	100
K78	78-4-MgO	43,09	4,69	7,17	9,77	0,55	15,13	11,84	3,87	2,42	1,47	100
K78	78-4b-MgO	35,78	7,24	9,2	13,15	0,43	16,64	14,27	0,35	0	2,94	100
K78	78-4-MgO	38,16	7,82	10,54	9,1	0,4	8,15	20,72	0,52	0,14	4,45	100
K78	78-4c-MgO	36,6	4,83	15,43	8,34	0,72	6,41	21,51	0,39	0	5,77	100
K78	78-5-MgO	41,7	1,44	14,14	8,86	0,39	6,74	11,81	12,29	0,71	1,92	100

10. Discussion

10.1. Do the inclusions represent real melts?

The apatite crystals containing poly-crystalline inclusions were heated to 1100°C and held at this temperature for 15 minutes. The goal was to achieve a homogeneous quenched glass that would reflect the composition of the liquid in equilibrium with the apatite during its crystallization. Surprisingly, most inclusions remained unhomogenized, often displaying up to four distinct phases. Very few inclusions presented a homogenized texture after being heated and the majority of the homogenized inclusions were identified as chlorite and biotite solid inclusions (Annex 18).

10.1.1. Re-homogenization temperatures

The unhomogenized texture of the apatite-hosted inclusions initially led us to question the target temperature and heating duration applied during our experiments. Fischer *et al.* (2016) and Wang *et al.* (2018) both heated their apatite-hosted inclusions to 1100°C but maintained this temperature for at least 30 minutes. Both studies re-homogenized melt inclusions of similar size (10 to 120 μm) to those in our study. Fischer *et al.* (2016) observed no residual crystals, whereas Wang *et al.* (2018) identified complex Fe-rich compositions containing fine-grained oxides such as magnetite. These were interpreted as small daughter phases that crystallized during the cooling of the trapped liquid according to the reaction: $FeO + H_2O = Fe_3O_4 + H_2$. The loss of H_2 rendered the process irreversible (Danyushevsky *et al.*, 2002). The residual Fe-Ti oxides in their study resembled the fine-grained pseudobrookite and ferro-pseudobrookite found in some re-homogenized inclusions in our study (Figure 12 D). However, this explanation does not seem applicable to the large crystals of magnetite and ilmenite present in the Kodal inclusions. The remaining phases are significantly larger and occupy approximately 50% of the volume in most inclusions.

Higher temperatures have been applied in other studies on different host phases. For example, the plagioclase-hosted inclusions in the Skaergaard intrusion achieved complete homogenization between 1135 and 1160°C. The apatite daughter phases in these inclusions melted within a narrow range of approximately 15°C, starting at around 1105°C, followed by the melting of Fe-Ti oxides, and finally, clinopyroxene and plagioclase, which began melting at 1100–1115°C. These observations suggest that applying higher temperatures would lead to the melting of the remaining Fe-Ti oxides and silicates but would also result in the host mineral melting and contaminating the melt inclusion composition.

The purpose of studying melt inclusions is to reheat them to the temperature at which they were originally trapped, thereby reversing the phase changes that occurred during natural cooling. However, significant differences can exist between the physical conditions of natural crystallization and experimental reheating. Even though the temperature may be reproduced, the pressure within the inclusion and the heating rate differs from the cooling rate. The melt inclusion composition can be affected by processes such as volatile dissociation, oxidation, and partial re-equilibration with their host during the experiment (Danyushevsky *et al.*, 2002). The assumed temperature for primary apatite crystallization is estimated to be between the liquidus and solidus temperatures of the larvikite magma, which are 1050°C and 750°C, respectively (Neumann, 1976; Andersen, 1984; Andersen and Seiersten, 1994).

Ultimately, the heating temperature used in our study aligns with previous studies on apatite-hosted inclusions and coincides with the onset of apatite crystallization. This suggests that the preserved crystals observed after heating may have a different origin from the liquid. Roeder (1984) reported that minerals found within polycrystalline inclusions may have distinct origins: daughter phases are minerals that precipitated directly from the trapped liquid, while solid minerals may have been trapped as pre-existing crystallized phases along with the liquid.

Inclusions from Kodal appear to contain both types of phases. The Fe-Ti oxides did not seem to be affected by the heating, as they remained intact alongside the other silicate crystals. In contrast, smaller inclusions, as shown in Figure 14, do not seem to have incorporated solid crystals during liquid entrapment. Other features support the solid inclusion theory, such as the intergrowth of certain phases in the inclusion with the apatite host (Annex 1). Additionally, the presence of highly diverse phases from one inclusion to another contradicts Roeder's (1984) definition of daughter phases, which are expected to crystallize similar phases in uniform proportions. These observations align with the theory of Si-rich and Fe-rich silicate liquid immiscibility pairs being trapped in melt inclusions, although the proportions of phases vary (Charlier *et al.*, 2012). Among the major phases present in the polycrystalline inclusions, large crystals of magnetite and biotite are consistently found in most inclusions. In contrast, ilmenite crystals are more inconsistent, along with other major phases such as K-feldspar, Ca-amphibole, pyroxene, and plagioclase, which are only present in a few inclusions. Minor elements exhibit a wide range of compositions that also vary notably among the different polycrystalline inclusions.

A large majority of the studied inclusions display residual crystals, a predominance likely induced by the hand-picking separation. Indeed, the larger and darker inclusions are more visible through the apatite crystal and were preferentially picked. Additionally, larger inclusions with varied compositions and colors were selected to avoid those containing single minerals, which were also observed (chlorite and magnetite inclusions).

10.1.2. Compositions of the melt inclusions and residual crystals

The quenched liquid is characterized by a homogeneous texture that surrounds the remaining crystals, except for the large Fe-Ti oxides, which tend to locate at the edges of the inclusion. The melt compositions are quite similar between different samples (K78 and K79) and cover a narrow compositional range, suggesting that the apatite crystals may have trapped a liquid along with the solid crystals. Compared to the residual crystals in the inclusions, the quenched liquids present a higher diversity of elements and have lower CaO and MgO contents than the majority of the residual silicates.

Given that the vast majority of crystals contain residual crystals, often consisting of an assemblage of Fe-Ti oxides and silica, the number of homogenized inclusions is insufficient for a meaningful comparison. However, no major variations in the major element compositions of the inclusions are observed based on the residual phases present. However, Wang *et al.* (2018) noted that apatite-hosted inclusions from Panzhihua, with remaining crystals after heating, were on average richer in SiO_2 and depleted inFeO_{tot}.

We note that the majority of the heated inclusions were fractured after heating; these fractures supposedly occurred during the decompression phase of the pressure cylinder. Although we assume that the apatite crystal offers a closed system for the inclusions, the heating, combined with the fractures, leads to variations in formation conditions such as oxygen fugacity and water content, or also possibly the re-equilibrating with their host (Danyushevsky et al., 2002). The changes in these parameters during heating, compared to the trapping and crystallization stage of the inclusions, could have led to new phases within the inclusions, particularly in minerals sensitive to these changes such as Fe-Ti oxides (pseudobrookite, ferro-pseudobrookite and perovskite).

10.2. Did liquid immiscibility play a role?

Our curiosity about silicate liquid immiscibility as a process behind the formation of the Kodal deposit was piqued by the striking color differences between the polycrystalline inclusions (Figure 12 A). We noticed light-colored inclusions, primarily composed of silica, contrasted with darker inclusions rich in Fe-Ti oxides. This vivid distinction hinted that some inclusions might have crystallized from a Si-rich liquid and others from an Fe-rich liquid, both coexisting in equilibrium at the same time in the magma chamber. This observation strongly suggested the possibility of liquid immiscibility playing a key role in the formation of the Kodal deposit.

Beyond the composition of melt inclusions, their abundance in a slow-cooling environment could be attributed to chemical and physical changes caused by emulsification (Veksler, 2006; Jakobsen *et al.*, 2011). Indeed, silicate liquid immiscibility results in the formation of emulsified droplets, consisting of viscous, low-density Si-rich liquids and low-viscosity, high-density Fe-rich liquids (Holness *et al.*, 2011).

In the past two decades, the concept of silicate liquid immiscibility has re-emerged to explain the formation of large Fe-Ti-P ore deposits in layered intrusions within slowly cooled tholeiitic systems (Veksler & Charlier, 2015). Liquid immiscibility is a challenging process to identify, as it produces two melts in equilibrium that crystallize the same minerals in different proportions (Charlier *et al.*, 2013). Additionally, solidified rocks, particularly in intrusive systems, rarely preserve a record of the original melt composition. Nevertheless, the study of melt inclusions has provided new insights and has been key to associating the concept of immiscibility with natural intrusive rocks. Liquid immiscibility has been described using melt inclusion data in numerous locations, primarily within tholeiitic systems, such as the Skaergaard intrusion in East Greenland (Jakobsen *et al.*, 2005, 2011), the Bushveld intrusion in South Africa (Fischer *et al.*, 2016), the Sept Îles intrusion in Canada (Charlier *et al.*, 2011), and the Panzhihua intrusion in China (Wang *et al.*, 2018).

The Kodal deposit, though smaller and formed in an alkaline system lacking significant layering, it shares with those massive deposits, the intriguing iron-titanium-phosphorus mineralization. Apatite crystals are the prominent phases of the Kodal deposit, containing all the phosphorus and housing the majority of the REE-rich minerals along their edges. These apatite crystals are crucial to our study, as they captured portions of the parental melt as inclusions during their crystallization. Given the similarities between the Fe-Ti-P mineralization in the tholeiitic deposits and the Kodal deposit, it is valuable to compare their melt inclusion data with our findings from Kodal, particularly in order evaluate if liquid immiscibility played a role in the formation of Kodal mineral deposit. To further this comparison, our melt inclusion data will also be evaluated alongside experimental liquid immiscibility data (Dixon and Rutherford, 1979; Charlier *et al.*, 2013; Zhang *et al.*, 2023).

Although silicate liquid immiscibility was primarily reported in tholeiitic environments, it appears that higher TiO_2, P_2O_5, and alkali content tend to promote immiscibility by expanding the two-liquid field (Charlier & Grove, 2012). Since the melt inclusions associated with the Kodal deposit are particularly enriched in alkalis ($Na_2O + K_2O$), this makes it a good candidate for studying silicate liquid immiscibility.

10.2.1. Lack of the Si-rich composition

The most noticeable difference between the literature data and the inclusions from Kodal is the narrow compositional range of SiO_2. In the Kodal inclusions, SiO_2 ranges from 29 to 45.1 wt.%, and for the restricted selection, it is even narrower, from 38.7 to 45 wt.% SiO_2 (Figure 16A-B).

Jackobsen *et al.* (2005) was the first to identify immiscibility in the Skaergaard intrusion using apatite- and olivine-hosted melt inclusions. He later extended his work to other areas using plagioclase-hosted inclusions (green crosses; Jacobsen *et al.*, 2011). The apatite-hosted inclusions revealed two distinct compositional poles: numerous Fe-rich inclusions and a few Si-rich ones (pink crosses; Figure 16 A). When plotted alongside the plagioclase-hosted inclusions, the Skaergaard inclusions exhibit a continuous Fe-rich to Si-rich compositional range, similar to the data from the Bushveld and Panzhihua layered intrusions (Fischer *et al.*, 2016; Wang *et al.* 2018). Jacobsen *et al.* (2011) interpreted the absence of a compositional gap as the result of trapping droplets of both immiscible liquids in varying proportions. Similarly, apatite-bearing melt inclusions from the Sept Iles intrusion revealed the presence of two immiscible liquids within a single inclusion (Charlier *et al.*, 2011).
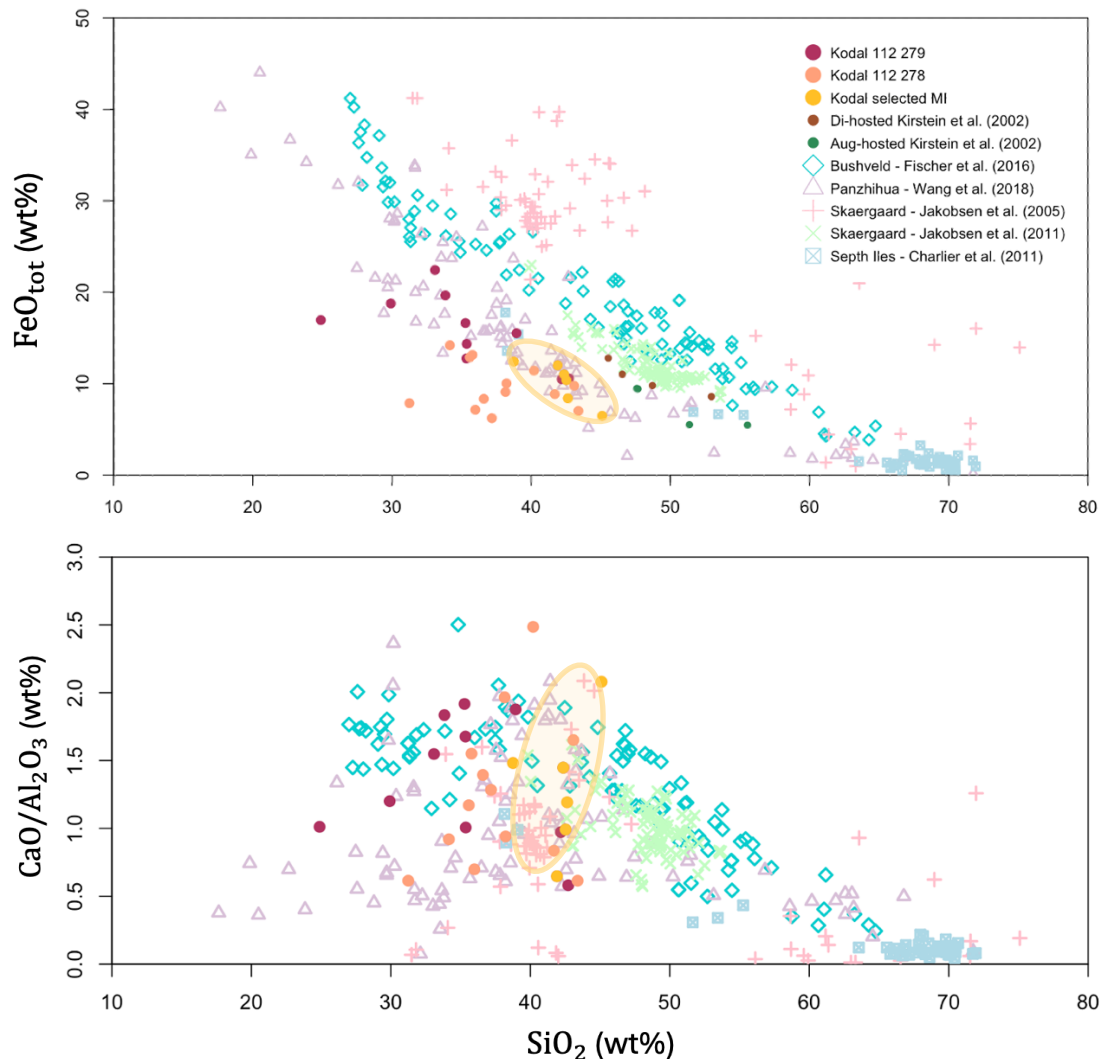
Figure 16. Compositional variation of the re-homogenized melt inclusions for FeO_{tot} and (CaO/AL_2O_3) as a function of SiO_2 (wt.%)

Fischer *et al.* (2016) provided further insights into the continuous compositional range of apatite-hosted melt inclusions from Bushveld (turquoise losange; Figure 16 A). He suggested that this range of compositions resulted from the trapping of melt along the bimodal immiscibility surface during cooling. Fischer *et al.* (2016) estimated that from the apatite solidus to the complete crystallization of the crystal mush, apatite crystals would have trapped melt compositions over a temperature range of approximately 60 °C.

A similar extended continuous compositional range is notable in the Panzhihua gabbroic-layered intrusion in southwest China (purple triangles; Figure 16, Wang *et al.*, 2018). The only difference is that the curve defined by the compositions of the inclusions is slightly shifted downward compared to other localities, highlighting a slight overall deficit in FeO_{tot} (Figure 16 A).

Interestingly, this characteristic is consistent with the compositions measured in Kodal, where a similar deficit in FeO_{tot} is observed. It remains nevertheless evident that the melt inclusions from Kodal cover a narrower compositional range regarding the FeO_{tot} and SiO_2 content (29–45.1 wt.% SiO_2 and 6.23–2,43 wt.% FeO_{tot} ; Figure 16 A).

In contrast, the apatite-hosted melt inclusions from the Sept Iles layered intrusions exhibit a smaller compositional range with two distinct poles: the Fe-rich pole and the more abundant Si-rich pole (blue squares, Figure 16 A). Compared to other studies on natural rocks, the Fe-rich melt composition from the most evolved cumulates of the Sept Iles closely resembles the Kodal melt inclusion compositions (Figure 16 A). The apatite-hosted inclusions from the Sept Iles have intermediate compositions of 18 wt.% FeO_{tot} and 38 wt.% SiO_2 for the Fe-rich inclusions, and the most Si-enriched inclusions contain 0.5 wt.% FeO_{tot} and 70 wt.% SiO_2. In parallel, the Fe-rich compositions found in the Bushveld and Panzhihua intrusions are significantly higher than those from Sept Iles and Kodal, reaching respectively, 35 and 40 wt.% FeO_{tot}, for 25 and 17 wt.% SiO_2 (Fischer *et al.*, 2016; Wang *et al.*, 2018).

Despite FeO_{tot} and SiO_2 being the principal major elements that show the most significant compositional differences between immiscible liquids, other elements also indicate the segregation of two liquids. When liquid immiscibility occurs, the major elements partition between the conjugate liquids: alumina and alkalis concentrate in the Si-rich liquid, whereas TiO_2, MgO, FeO_{tot}, MnO, CaO, and P_2O_5 concentrate in the Fe-rich liquid. Since Ca partitions into the Fe-rich liquid, in contrast to Al which preferentially concentrates in the Si-rich liquid, the ratio of CaO/Al_2O_3 tends to be higher in the immiscible Fe-rich liquid (Watson, 1976; Dixon & Rutherford, 1979; Philpotts, 1982; Jacobsen *et al.*, 2011).

Both in natural rocks and experimental data, the CaO/Al_2O_3 ratio aligns with the expected values for an emulsified Fe-rich liquid (Figure 16 B and 17 B). However, it is noteworthy that the CaO values show very little variation over the range of SiO_2 covered by the Kodal melt inclusions. CaO appears to be the only element that does not exhibit a simple linear trend when plotted as a function of SiO_2 in the apatite-hosted inclusions from Bushveld and Panzhihua (Fischer *et al.*, 2016; Wang *et al.*, 2018). Although a general decreasing trend is observed, at low SiO_2 contents (25 to 40 wt.% SiO_2), the CaO values stabilize and even show an inverse slope, consistent with Kodal observations. This trend is also observable in Figure 16 B, where the Al_2O_3 content follows a linear trend with increasing SiO_2 content.

Subsequently, Kodal melt inclusions were compared to experimental data (Dixon and Rutherford, 1979; Charlier *et al.*, 2013; Zhang *et al.*, 2023) and to immiscible glasses that commonly occur in the mesostasis of tholeiitic basalt and much less frequently in alkaline basalts (Figure 17, Philpotts, 1982). This occurrence imbalance is essentially due to the lack of residual liquids that are quenched to glass in alkaline volcanic rocks, and it does not inform on the unmixing properties of alkaline systems (Philpotts, 1982).
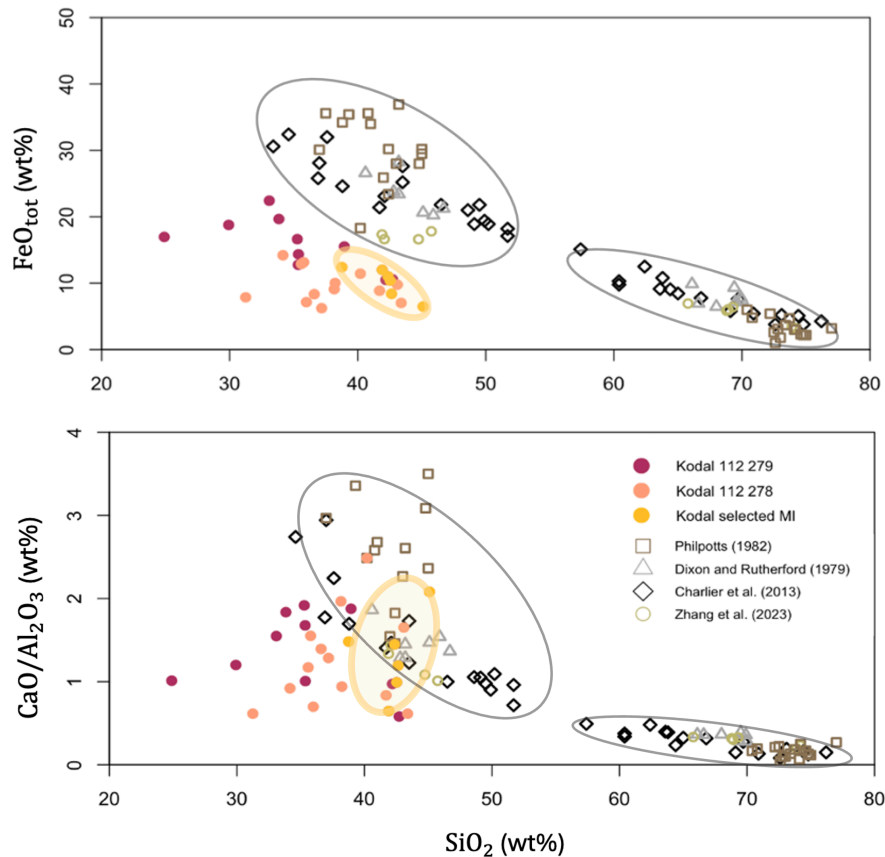
Figure 17. Compositional variation of the re-homogenized melt inclusions for FeO_{tot} and (CaO/AL_2O_3) as a function of SiO_2 (wt.%)

Compared to most melt inclusion compositions, experimental and mesostasis data exhibit two well-defined distinct poles (black circles, Figure 17). On the graph of FeO as a function of SiO_2, the Kodal inclusions cluster near the Fe-rich pole. However, none of the points intersect the experimental pole.

Examining the pseudo-ternary Greig diagram, which represents all major elements simultaneously, reveals that the melt inclusions in Kodal are exclusively aligned with the Fe-rich poles based on their SiO_2 content (Figure 18 A). Additionally, the melt inclusion data display a broader range of compositions that encompass the Kodal data. However, within the well-defined poles of the experimental data, the Kodal inclusions show higher contents of alumina and alkalis (Figure 18 B).
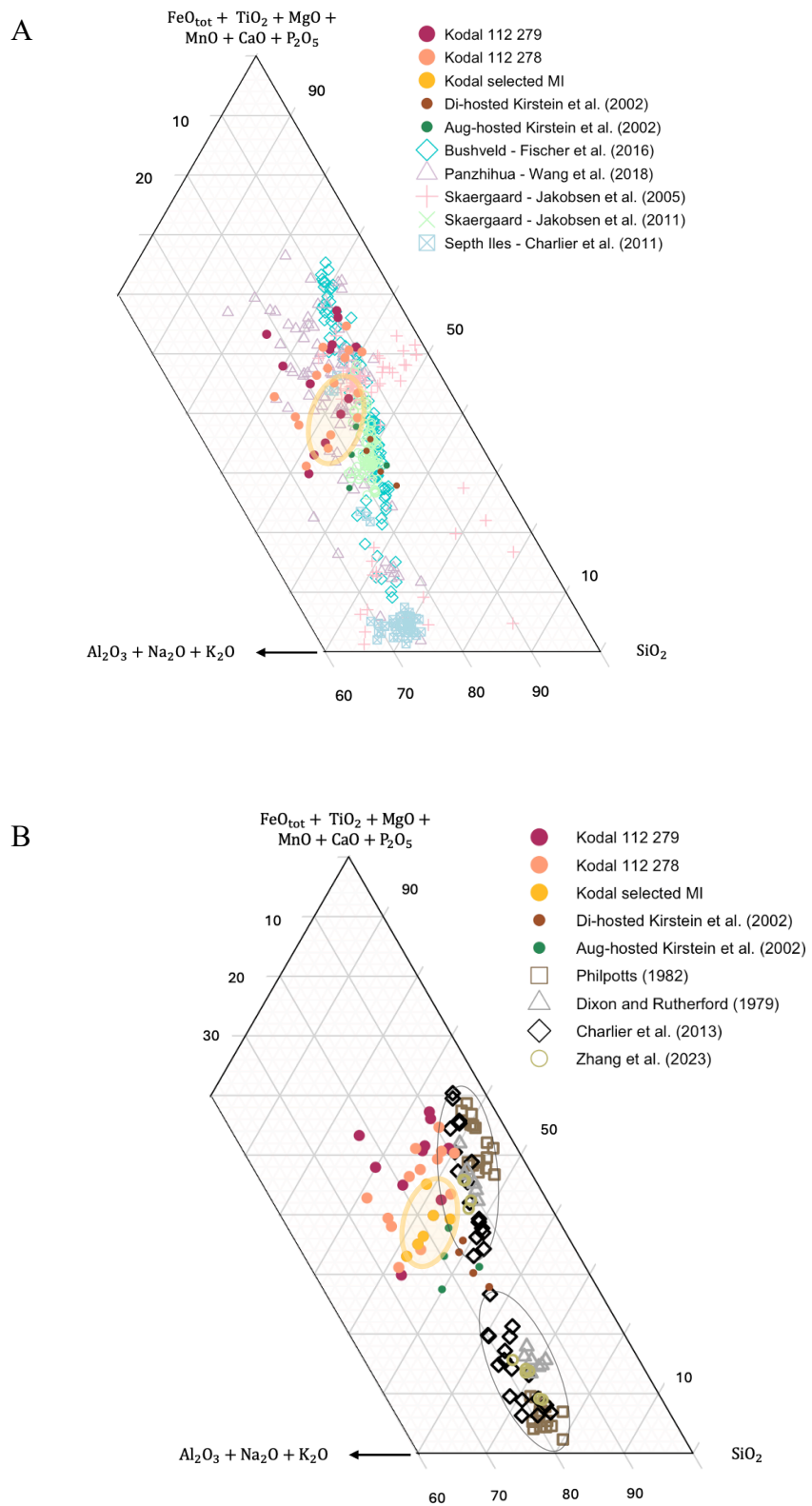
Figure 18. Pseudo-ternary Greig diagram. **A.** Comparison between Kodal melt inclusions and literature on immiscible inclusions. **B.** Comparison between Kodal melt inclusions and experimental Fe-rich and Si-rich immiscible melts in equilibrium, coupled with Philpotts (1982) immiscible glasses in the mesostasis.

Philpotts (1982), by comparing immiscible glasses occurring in the mesostasis of tholeiitic and alkaline basalts, highlighted that major elements segregate in the same manner within the conjugate liquids. However, certain elements partition in different proportions depending on the alkaline content of the basalts. For example, CaO and FeO can be deficient in the Fe-rich liquid in alkaline rocks. Nevertheless, SiO_2 exhibits the same partitioning in both tholeiitic and alkaline basalts, which implies similar widths of the immiscibility field (Philpotts, 1982).

These observations suggest that if immiscibility occurred during the formation of the Kodal deposit, the measured compositional range is incomplete. As previously highlighted, the melt compositions of Kodal exhibit a narrow compositional range, approximating the Fe-rich pole of the segregated liquids, with a complete absence of compositions above 45 wt.% SiO_2, which would correspond to the Si-rich pole of the immiscible liquids.

Several factors could explain the lack of Si-rich melts:

- Depending on where the liquid line of descent intersects the bimodal immiscibility surface during cooling, the segregated melts are produced in different proportions. If the liquid line of descent favors Fe-rich melts, these will be the predominant phase, reducing the probability of trapping Si-rich melts.

- Apatite crystals are preferentially wetted by Fe-rich melts (Philpotts, 1979; Holness *et al.*, 2011; Jakobsen *et al.*, 2011), which explains the higher concentration of Fe-rich compositions in the inclusions. This is primarily due to phosphorus's tendency to partition significantly into the Fe-rich liquid if immiscibility occurs (Veksler *et al.*, 2006; Jakobsen *et al.*, 2011). However, data from Kodal consist exclusively of Fe-rich melts.

- Since larger, darker inclusions were more visible through the apatite, they might have been preferentially picked. However, the range of samples is presumably broad enough to avoid this bias.

Despite these possible factors that would preferentially trap Fe-rich melts, the complete absence of Si-rich melts remains suspicious. Another interpretation of the narrow compositional range could be that the formation of the Kodal deposit followed a simple evolution involving only fractional crystallization without silicate liquid immiscibility.

To explore this further, we will compare the melt inclusion data to the whole-rock compositions measured at multiple localities in the Larvik plutonic complex (LPC) and the northern area, which comprise similar iron- and phosphorus-rich mineralization.

10.2.2. General iron depletion

Figure 19 shows in grey the whole-rock data of several Fe-Ti-P mineralizations and their surrounding rocks, all located in the western hemisphere at a maximum of 20 km from the Kodal deposit (all the Fe-Ti-P-REE occurrences (yellow stars) are mapped in Figure 2). This includes the LPC (lardalite, foyalite, monzonite, syenite), the Løkka intrusion (monzonite and syenite), the Rimstad intrusion (monzonite, syenite), the Kiste intrusion (syenite), the Siljan intrusions (monzodiorite, monzonite, quartz-monzonite, syenite), and the Skrim intrusion composed of monzonite. These data were provided by the NGU and will be published in Mansur *et al.* (in preparation). Conversely, the whole-rock measurements collected from the Kodal deposit are part of a doctoral thesis and will be published in Buellens *et al.* (submitted) (shaded blue dots in Figure 19).

As expected, massive ore area form Kodal exhibit whole-rock compositions that are silica-depleted and show the highest concentrations of FeO_{tot}, reaching up to 55 wt.% (Figure 19). In contrast, the surrounding rocks (monzonite) and the syenite dykes that cross the deposit are at the other extreme of the graph (FeO_{tot} versus SiO_2), showing less than 10 wt.% FeO_{tot} for 50 – 65 wt.% SiO_2. The melt inclusion compositions sit between the two extremes and roughly follow the trend of the curve defined by the whole-rock compositions of all the intrusion zones (grey dots; Figure 19). However, the inclusions exhibit compositions shifted downward,
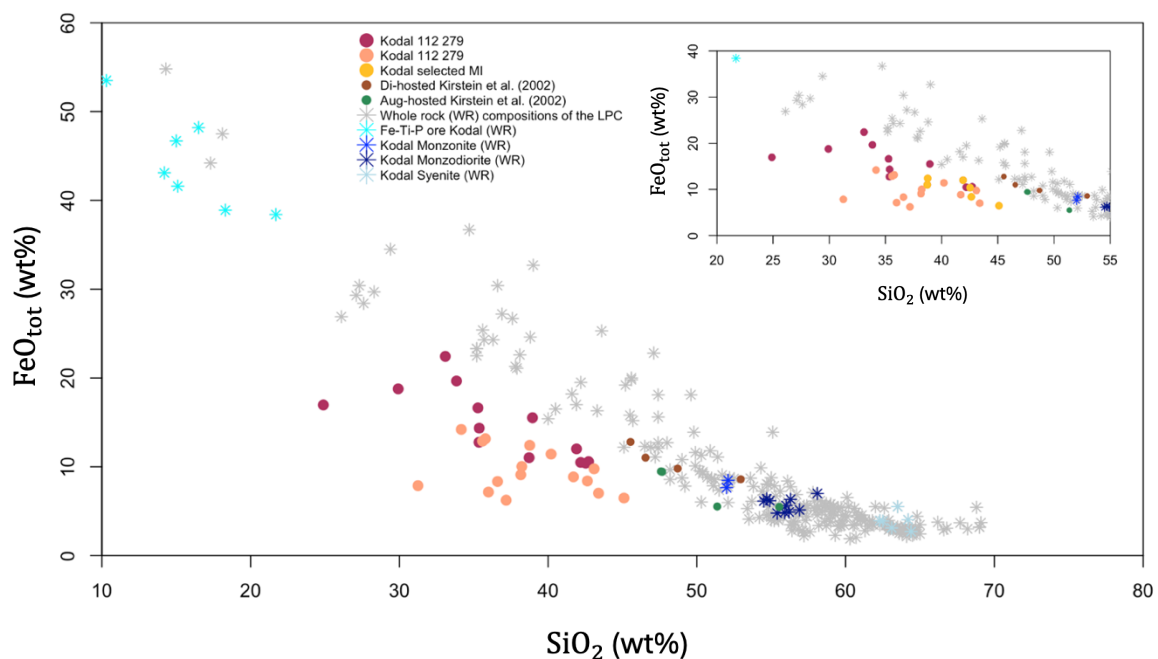
Figure 19. Compositional variation of FeO_{tot} versus SiO_2 of Kodal melt inclusions compared to whole rock data from several localities in the LPC and northern areas (Fe-Ti-P mineralizations and host rocks; data from Buellens *et al.* (submitted) and Mansur *et al.* (in preparation)).

The whole-rock data presented have undergone a series of igneous processes, such as fractional crystallization and magma mixing or unmixing, which prevent the preservation of the original melt composition. To minimize the impact of these processes, the Kodal melt composition will be compared to the first magmatic occurrence of the Oslo Rift: the B1-basalt sequences. These sequences offer a unique insight into the compositional evolution of the LPC alkaline magma during cooling.

10.2.3. Concordance with B1-basalts trends

B1-basalts mark the onset of magmatic activity in the Oslo Rift, occurring from 305 to 290 Ma (Sundvoll *et al.*, 1990; Neumann *et al.*, 2002). Extensive rift-related tectonism resulted in the extrusion of large volumes of basaltic lavas, which were subsequently covered by younger rock except in localized areas such as Skien and the eastern margin of the Vestfold lava field (Neumann *et al.*, 1990). These primitive basaltic series are located at the extremities of the Oslo Rift, on both sides of the Kodal deposit (Figure 1).

The Skien area presents the thickest lava sequence in the Oslo Rift (~1500 m), consisting of nephelinite at the base, with alkalinity decreasing upward to basanites and alkali basalts at the top (TAS classification of Le Bas *et al.*, 1986; Segalstad, 1979; Neumann *et al.*, 1990).

Beyond providing insight into the primitive lavas of the Oslo Rift, clinopyroxene present as phenocrysts in the Skien area and in the Kodal mineralization (Jacupirangite), exhibit high Mg-numbers which indicates that both are derived from a more magnesian mafic magma. On the contrary, higher Mg-numbers ($\frac{Mg}{Mg+Fe_{tot}}$) are not characteristic of the mafic to intermediate intrusions of the Oslo region, such as the monzonitic host at Kodal (Andersen & Seiersten, 1994).

Additionally, two sequences from the Vestfold lava field were selected for comparison as they also offer an history of sub-alkaline to alkaline composition evolution. The oldest lavas appear in the 170 m thick Horten sequence, located at the easternmost part of the extrusion, compared to the 90 m long Holmestrand sequence (Neumann *et al.*, 1990). These sequences help illustrate the range of magmatic compositions present in the Oslo Rift.

The SiO_2 content in the Skien basalt shows minimal variation and falls within a similar range as the Kodal melt inclusions (39 wt.% to 46 wt.% SiO_2; Figure 20 A-B-C). Additionally, the majority of the inclusions generally follow the trends established by the B1 basalts. However, it is noteworthy that the inclusions from sample K78 exhibit a slight depletion in FeO_{tot} compared to the B1 basalts, while the inclusions from sample K79 show lower SiO_2 concentrations (down to 25 wt.%) with higher FeO_{tot} values.

As illustrated, primitive lavas exhibit low variation in SiO_2 content during the early stages of magmatic evolution (Figure 20 A-B-C). Consequently, we also illustrated the variation of major elements relative to MgO content. These graphs help understand the compositional evolution of magma during cooling, as MgO content is proportional to the liquidus temperature in basaltic magma (Bowen, 1924; Winter, 2010).

B1-basalt sequences from Skien and Vestfold exhibit continuous evolution in compositions with similar trends (grey arrows in Figure 20). Typically, as MgO decreases, there is a corresponding decrease in CaO and FeO_{tot}, while SiO_2, Al_2O_3 and $K_2O + Na_2O$ levels increase.
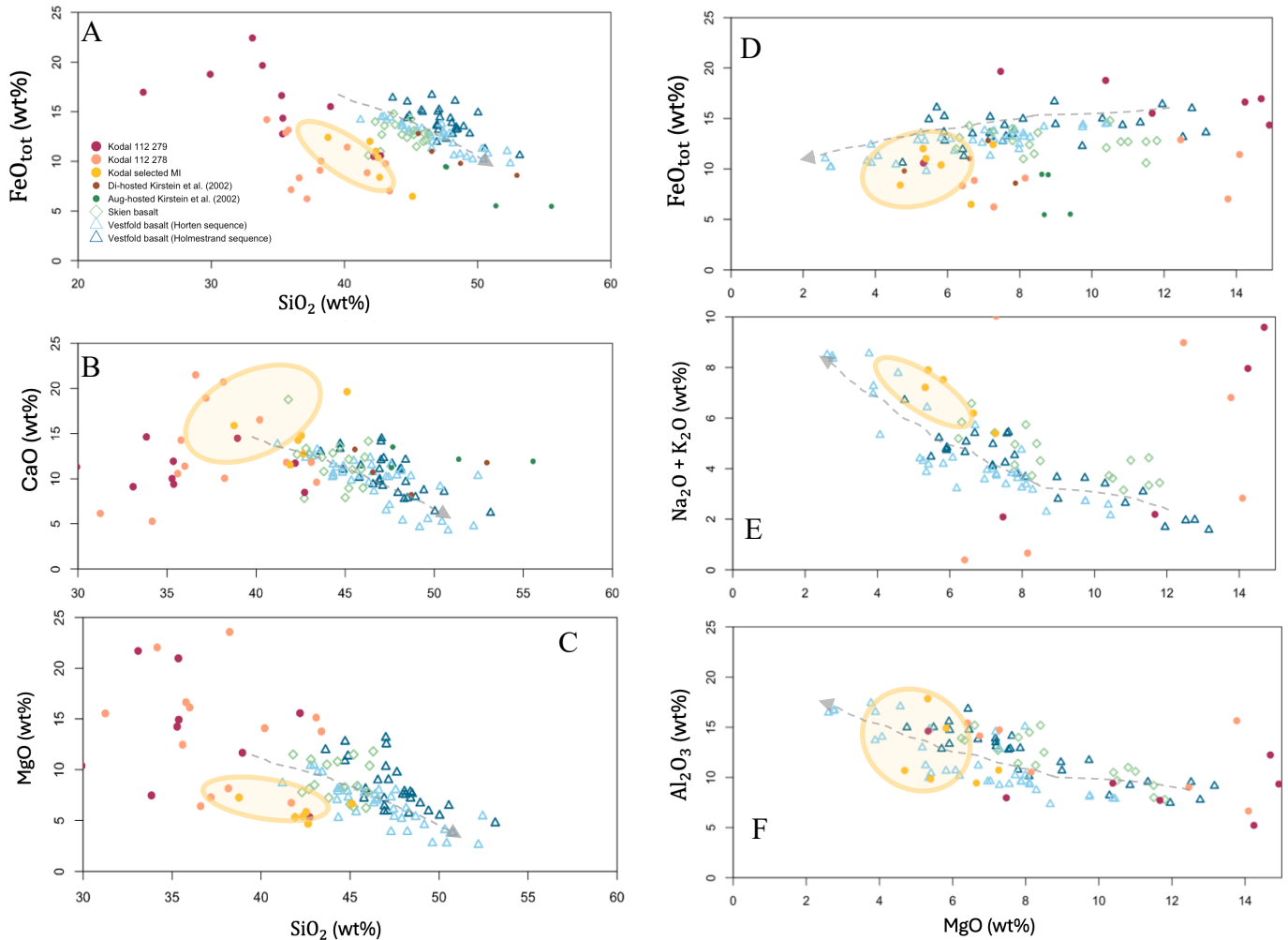
Figure 20. Major elements relation among B1 balsalt in Vestfold and Skien compared to Kodal melt inclusions.

The MgO content in the inclusions may be challenging to interpret since it was used as a criterion to select melt inclusions. As illustrated in Figure 20 C, MgO contents exceeding 15 wt.% are likely associated with the presence of MgO-rich microcrystals rather than representing the composition of a liquid. Nevertheless, the restricted selection of inclusions (yellow circles; Figure 20) shows depleted MgO content. The variation of FeO_{tot}, Al_2O_3 and $K_2O + Na_2O$ relative to MgO in the selected melt inclusions are consistent with all the sequences from the B1 basalts.

The concordance between the major elements in the melt inclusions and the B1-basalt (particularly with respect to MgO content) suggests a normal evolution of the magma solely through fractional crystallization. As previously noted, there are no distinct liquid compositions indicating possible emulsions during deposit formation. Furthermore, compositions relative to SiO_2 and total FeO_{tot} content remain highly constrained. However, it is important to note that the interpretations are based on a limited sample size, as most of the heated inclusions did not present a homogeneous phase.

11. Conclusion

In this study, we aimed to determine if silicate liquid immiscibility played a role in the formation of the Fe-Ti-P and REE-rich Kodal deposit. To do this, we examined the unique information trapped in the melt inclusions.

Several indications initially suggested the possibility of liquid immiscibility at the Kodal deposit. This deposit features a remarkable concentration of intriguing iron-titanium-phosphorus mineralization, similar in composition to the large Fe-Ti-P ore deposits found in slowly cooled tholeiitic systems where silicate liquid immiscibility has been suggested. Melt inclusion compositions have been the principal indicators of immiscibility in layered intrusions within tholeiitic environments. The Kodal poly-crystalline inclusions are similar in size and shape to those found in these environments, and their abundance within the apatite crystals may suggest the coexistence of various viscosities at the onset of apatite crystallization. Additionally, the variability in shades of the polycrystalline inclusions, ranging from light to dark, suggests that droplets of two immiscible liquids (Fe-rich and Si-rich) were trapped within the inclusions.

After heating and quenching the apatite-hosted inclusions, we observed that most inclusions still contained residual phases, predominantly Fe-Ti oxides. It was then pointed out that the abundance of Fe-Ti oxides was the principal parameter controlling the colors of the inclusions. Thus, the variability of the tints is not a reliable indicator of the composition of the melt inclusions. The large diversity of phases recorded within the poly-crystalline inclusions and the inconsistency of certain phases from one inclusion to another indicated that solid phases were trapped along with the liquid in the inclusions. The residual crystals were also diverse, including large magnetite, ilmenite, as well as sub-euhedral to euhedral silica.

Melt compositions were measured in the homogeneous textures of the heated inclusions, often surrounding residual crystals. Compared to the melt inclusion literature data from deposits in tholeiitic environments where silicate liquid immiscibility was reported, Kodal melt inclusions exhibit a smaller compositional range regarding SiO_2 and FeO_{tot} contents. Nonetheless, the compositions are exclusively concordant with the Fe-rich pole of the emulsified liquids. These observations were similar to silicate liquid immiscibility experimental data. It is noted that the proportion of liquids in each immiscible pair is unknown, and Si-rich droplets may be rarer, which could explain their absence.

The complete absence of Si-rich liquid, coupled with the concordance of Kodal melt inclusions with the natural evolution of the B1-basalt, preferentially suggests that silicate liquid immiscibility did not play a role in the formation of the Kodal deposit.

These results should be interpreted with caution, as more than half of the heated inclusions did not present homogenized textures but rather a multitude of microcrystals from which no liquid composition could be measured. Furthermore, the melt inclusion compositions were generally deficient in FeO_{tot} and SiO_2, especially compared to LPC whole-rock data and B1-basalts. This deficiency could be correlated with the numerous residual crystals. It would be beneficial to experiment with heating at different temperatures and for longer durations to observe variations in textures and compositions.

12. References

Andersen, T., 1984. Crystallization history of a Permian composite monzonite-alkali syenite pluton in the Sande cauldron, Oslo rift, southern Norway. *Lithos*, 17, 153–170.

Andersen, T. & Seiersten, M., 1994. Deep cumulates in a shallow intrusion: origin and crystallization history of a pyroxenite (jacupirangite s.l.) body in the Larvik Pluton, Oslo Region, South Norway. *Neues Jahrbuch für Mineralogie Monatshefte*, 6, 255–274.

Andres, U., Jirestig, J. & Timoshkin, I., 1999. Liberation of minerals by high-voltage electrical pulses. *Powder Technology*, 104, 37–49. https://doi.org/10.1016/S0032-5910(99)00024-8

Andres, U., Timoshkin, I., Jirestig, J. & Stallknecht, H., 2001. Liberation of valuable inclusions in ores and slags by electrical pulses. *Powder Technology*, 114, 40–50. https://doi.org/10.1016/S0032-5910(00)00260-6

Barth, T. F. W., 1945. Studies on the igneous rock complex of the Oslo Region, II. Systematicpetrography of the plutonic rocks. Skrifter fra detNorske Videnzaps-Akademi i Oslo, I, Matematisk-Naturvidenskapelige Klasse, 1944 (9), p. 104.

Bergstøl, S., 1972. The jacupirangite at Kodal, Vestfold, Norway. *Mineralium Deposita*, 7, 233–246.

Berthelsen, A., 1980. Towards a palinspastic tectonic analysis of the Baltic shield. *In* Cogné, J., & Slausky, M. (eds), *Geology of Europe*. 26th ed. Paris. Mémoires du bureau de recherches géologique et mininière, 26th International Geological Congress, 108, 5–21.

Berthelsen, A., Olerud, S. & Sigmond, E. M. O., 1996. *Oslo, bedrock geology map*. 1:250,000. Norway, Norges Geologiske Undersokelse.

Brøgger, W. C., 1898. Die Eruptivgesteine des Kristianiagebietes. III. Das Ganggefolge des Laurdalits. Vid.-Akad. Skr. I. Mat. Nat. K1. 1897. No 6, 1—377.

Brøgger, W. C. (1890). Die Mineralien der Syenitpegmatitgänge der südnorwegischen Augit- and Nephelinsyenite. *Zeitschrift für Kristallographie*, 16(1), 235–663.

Brøgger, W. C. & Schetelig, J., 1923. *Geologisk oversiktskart over Kristianiafeltet*. 1:250,000. Norway, Norges Geologiske Undersokelse.

Brøgger, W. C., 1933. Die Eruptivgesteine des Oslogebietes. VII. Die chemische Zusammensetzung der Eruptivgesteine des Oslogebietes. *Skrifter Det Norske Videnskaps Akademi i Oslo. I, Matematisk-Naturvidenskapelig Klasse*, 1933(1), 1–147.

Boyd, F.R., England, J.L., 1960. The quartz-coesite transition. Journal of Geophysical Research (1896-1977) 65, 749–756. https://doi.org/10.1029/JZ065i002p00749

Bowen, N. L., 1928. *The Evolution of the Igneous Rocks*. Princeton University Press. Princeton, NJ. (1956 reprint by Dover, New York)

Buck, W. R., 1991. Modes of continental lithospheric extension. *Journal of Geophysical Research*, 96(B12), 20161–20178. https://doi.org/10.1029/91JB01485

Daly, R. A., 1914. Igneous rocks and their origin: New York, McGraw-Hill, 563 p.

Danguy, L. & Quivy, R., 1956. Rétrodifussion (backscattering) des électrons par les solutions et les alliages. *Journal de physique Radium*,17 (4), 320–325. https://doi.org/10.1051/jphysrad:01956001704032000

Danyushevsky, L. V., McNeill, A. W. & Sobolev, A. V., 2002. Experimental and petrological studies of melt inclusions in phenocrysts from mantle-derived magmas: an overview of techniques, advantages and complications. *Chemical Geology*, 183(1–4), 5–24. https://doi.org/10.1016/S0009-2541(01)00369-2

Charlier, B., Namur, O., Toplis, M.J., Schiano, P., Cluzel, N., Higgins, M.D. & Vander Auwera, J., 2011. Large-scale silicate liquid immiscibility during differentiation of thoeleiitic basat to granite and the origin of the Daly gap. *Geology,* 39(10), 907–910. https://doi.org/10.1130/G32091.1

Charlier, B. & Grove, T. L., 2012. Experiments on liquid immiscibility along tholeiitic liquid lines of descent. *Contributions to Mineralogy and Petrology,* 164, 27–44. https://doi.org/10.1007/s00410-012-0723-y

Charlier, B., Namur, O. & Grove, T. L., 2013. Compositional and kinetic controls on liquid immiscibility in ferrobasalt–rhyolite volcanic and plutonic series. *Geochimica et Cosmochimica Acta*, 113, 79–93. https://doi.org/10.1016/j.gca.2013.03.017

Coes, L., 1955. High-pressure minerals. *American Ceramic Society*, 38, 298.

Corfu, F. & Dahlgren, S., 2008. Perovskite U-Pb ages and the Pb isotopic composition of alkaline volcanism initiating the Permo-Carboniferous Oslo rift. *Earth and Planetary Science Letters*, 265, 256–269. https://doi.org/10.1016/j.epsl.2007.10.019

Condamine, P., Tournier, S., Charlier, B., Médard, E., Triantafyllou, A., Dalou, C., Tissandier, L., Lequin, D., Cartier, C., Füri, E., Burnard, P.G., Demouchy, S. & Marrocchi, Y., 2022. Influence of intensive parameters and assemblies on friction evolution during piston-cylinder experiments. *American Mineralogist*, 107, 1575–1581. https://doi.org/10.2138/am-2022-7958

Dahlgren, S., Corfu, F. & Heaman, L. M., 1996. U-Pb isotopic time constraints, and Hf and Pb source characteristics of the Larvik plutonic complex, Oslo paleorift. Geodynamic and geochemical implications for the rift evolution. V.M. Goldsschmidt, *Conference abstracts*, 1, p. 120.

Dahlgren, S., 2004. *Nordagutu, bedrock geology map 1713 IV*. 1: 50,000. Norway, Norges Geologiske Undersokelse.

Dahlgren, S., 2010. The Larvik plutonic complex: The larvikite and nepheline syenite plutons and their pegmatites. *In* Larsen, A. O. (ed), *The Langensundsfjord History, Geology, Pegmatites, Minerals*. Salzhemmendorf, Bode, 26–37.

Danyushevsky, L. V., McNeill, A. W., Sobolev, A. V., 2002. Experimental and petrological studies of melt inclusions in phenocrysts from mantle-derived magmas: an overview of techniques, advantages and complications. *Chemical Geology*, 183(1–4), 5–24. https://doi.org/10.1016/S0009-2541(01)00369-2

Decrée, S., Coint, N., Debaille, V., Hagen-Peter, G., Leduc, T. & Schiellerup, H., 2022. The Potential for REEs in Igneous-related Apatite Deposits in Europe. *In* Smelror, M., Hanghøj & Schiellerup, H. (eds), *The green stone age: exploration and exploitation of minerals for green technologies*. London, Geological Society, Special Publications, 526, 219–249. https://doi.org/10.1144/SP526-2021-175

Dixon, S., & Rutherford, M. J., 1979. Plagiogranites as late-stage immiscible liquids in ophiolite and mid-ocean ridge suites: An experimental study. *Earth and Planetary Science Letters*, 45(1), 45–60. https://doi.org/10.1016/0012-821X(79)90106-7

Dunn, T., 1993. The piston-cylinder apparatus. *In* Luth R.W. (Ed.), *Experiments at high pressure and applications to the earth's mantle, MAC Short Course Handbook, Volume 21.* Mineralogical Association of Canada, 39–94.

Fischer, L.A., Wang, M., Charlier, B., Namur, O., Roberts, R.J., Veksler, I.V., Cawthorn, R. G. & Holtz, F., 2016. Immiscible iron- and silica-rich liquids in the upper zone of the Bushveld complex. *Earth Planetary Science Letters,* 443, 108–117. https://doi.org/10.1016/j.epsl.2016.03.016

Hall, H. T., 1958. Some high-pressure, high-temperature apparatus design considerations: equipment for use at 100,000 atmospheres and 3000°C, *Review of Scientific Instruments,* 29, 267-275. https://doi.org/10.1063/1.1716172

Hess, P. C., 1995. Thermodynamic mixing properties and the structure of silicate melts. *In* Stebbins, J. F., McMillan, P. F. & Dingwell, D. B. (eds), *Structure, dynamics and properties of silicate melts*. Washington, D.C., Mineralogical Society of America, Reviews in mineralogy, 32, 145–190.

Holness, M., Stripp, G., Humphreys, M., Veksler, I., Nielsen, T., Tegner, C., 2011. Silicate liquid immiscibility within the crystal mush: late-stage magmatic microstructures in the Skaergaard intrusion, East Greenland. *Journal of Petrology*, 52(1), 175–222. https://doi.org/10.1093/petrology/egq077

Honour, V.C., Holness, M.B., Charlier, B. Piazolo, S. C., Namur, O., Prosa, T. J., Martin, I., Rosalind, T. H., Maclennan, J., Jean, M. M., 2019. Compositional boundary layers trigger liquid unmixing in a basaltic crystal mush. *Nature Communications,* 10, 4821. https://doi.org/10.1038/s41467-019-12694-5

Humphreys, M. C. S., 2011. Silicate liquid immiscibility within the crystal mush: evidence from Ti in plagioclase from the Skaergaard intrusion. *Journal of Petrology*, 52(1), 147–174. https://doi.org/10.1093/petrology/egq076

Ihlen, P. M., Schiellerup, H., Gautneb, H. & Skår, Ø., 2014. Characterization of apatite resources in Norway and their REE potential — a review. *Ore Geology Reviews,* 58, 126–147. https://doi.org/10.1016/j.oregeorev.2013.11.003

James, P. F., 1975. Liquid-phase separation in glass-forming systems. *Journal of Materials Science*, 10, 1802–1825.

Jakobsen, J. K., Veksler, I. V., Tegner, C. & Brooks, C. K., 2005. Immiscible iron- and silica-rich melts in basalt petrogenesis documented in the Skaergaard intrusion. *Geology*, 33(11), 885–888. https://doi.org/10.1130/G21724.1

Jakobsen, J. K., Veksler, I. V., Tegner, C., Brooks, C. K., 2011. Crystallization of the Skaergaard intrusion from an emulsion of immiscible iron-and silica-rich liquids: evidence from melt inclusions in plagioclase. *Journal of Petrology*, 52(2), 345–373. https://doi.org/10.1093/petrology/egq083

Kent, A. J., 2008. Melt inclusions in basaltic and related volcanic rocks. *Reviews in Mineralogy and Geochemistry*,69(1), 273–331. https://doi.org/10.2138/rmg.2008.69.8

Kirstein, L. A., Dunworth, E. A., Nikogosian, I. K., Touret, J. L. R. & Lustenhouwer, W. J., 2002. Initiation of melting beneath the Oslo rift: a melt inclusion perspective. *Chemical Geology*, 183(1–4), 221–236. https://doi.org/10.1016/S0009-2541(01)00379-5

Kodal Minerals PLC, 2014. *Group Annual Report and Financial Statements for the year ended 31 March 2014*. London, England, 57 p. https://kodalminerals.com/wp-content/uploads/2017/08/Kodal-Report-and-Accounts-2014.pdf

Larsen, B. T., Olaussen, S., Sundvoll, B. & Heeremans, M., 2008. The Permo-carboniferous Oslo rift through six stages and 65 million years. *Episodes*, 31(1), 52–58. https://doi.org/10.18814/epiiugs/2008/v31i1/008

Latypov, R. M., Namur, O., Bai, Y., Barnes, S. J., Chistyakova, Sy., Holness, M. B., Iacono-Marziano, G., Kruger, W. A. J., O'Driscoll, B., Smith, W. D., Virtanen, V. J., Wang, C. Y., Xing, C.-M., & Charlier, B., 2024. Layered intrusions: Fundamentals, novel observations and concepts, and controversial issues. *Earth-Science Reviews*, *249*, 104653. https://doi.org/10.1016/j.earscirev.2023.104653

Le Bas, M. J., Le Maitre, R. W., Streckeisen, A. & Zanettin, B., 1986. A chemical classification of volcanic rocks based on the total alkali-silica diagram. *Journal of Petrology*, 27(3), 745–750. https://doi.org/10.1093/petrology/27.3.745

Le Maitre, R. W., Streckeisen, A., Zanettin, B., Le Bas, M. J., Bonin, B. & Bateman, P. (eds), 2022. Glossary of terms. *In igneous rocks: a classification and glossary of terms*. 2nd ed. Cambridge, Cambridge University Press, 43–158. https://doi.org/10.1017/CBO9780511535581

Lindberg, P. A., 1985. Fe–Ti–P mineralizations in the Larvikite–lardalite complex, Oslo Rift. *Norges geologiske undersøkelse bulletin*, 402, 93–98.

Liu, P. -P., Zhou, M. -F., Chen, W. T., Boone, M., Cnudde, V., 2014. Using multiphase solid inclusions to constrain the origin of the Baima Fe–Ti–(V) oxide deposit, SW China. *Journal of Petrology*. 55(2), 951–976. https://doi.org/10.1093/petrology/egu012

McBirney, A. R. & Nakamura, Y., 1974. Immiscibility in late-stage magmas of the Skaergaard intrusion. *Carnegie Inst Wash Yearb*, 73, 348–352.

Miranda, A.C.R., Coint, N., Dare, S. & Mansur, E.T., 2023. Iron-Ti and apatite mineralisation associated with alkaline monzonitic rocks: An example from the Kodal deposit, Permian Oslo Rift, Norway. *Proceedings of the 17th SGA Biennial Meeting*, 28 August – 1 September 2023. Zurich, Switzerland, 3, 229–232.

Namur, O., Charlier, B., Toplis, M. J., Higgins, M. D., Hounsell, V., Liégeois, J. P. & Vander Auwera, J., 2011. Differentiation of tholeiitic basalt to A-type granite in the Sept Iles layered intrusion, Canada. *Journal of Petrology*, 52(3), 487–539. https://doi.org/10.1093/petrology/egq088

Neumann, E. -R., 1976. Compositional relations among pyroxenes, amphiboles and other mafic phases in the Oslo Region plutonic rocks: Publication No. 115 in the Norwegian Geotraverse project. Lithos, 9(2), 85–109. https://doi.org/10.1016/0024-4937(76)90028-1

Neumann, E. -R., 1980. Petrogenesis of the Oslo region larvikites and associated rocks. *Journal of Petrology*, 21(3), 499–531. https://doi.org/10.1093/petrology/21.3.499

Neumann, E. -R., Sundvoll, B., Øverli, P. E., 1990. A mildly depleted upper mantle beneath southeast Norway: evidence from basalts in the Permo-Carboniferous Oslo Rift. *Tectonophysics*, 178 (1), 89–107. https://doi.org/10.1016/0040-1951(90)90461-G

Neumann, E.-R., Olsen, K. H., Baldridge, W. S. & Sundvoll, B., 1992. The Oslo rift: a review. *Tectonophysics*, 208, 1–18. https://doi.org/10.1016/0040-1951(92)90333-2

Neumann, E. -R., Dunworth, E. A., Sundvoll, B. A., Tollefsrud, J. I., 2002. B$_1$ basaltic lavas in Vestfold–Jeløya area, central Oslo rift: derivation from initial melts formed by progressive partial melting of an enriched mantle source. *Lithos*, 61, 1–2. https://doi.org/10.1016/S0024-4937(02)00068-3

Neumann, E. -R., Wilson, M., Heeremans, M., Spencer, E., Obst, K., Timmerman, M. J. & Kirstein, L., 2004. Carboniferous-Permian rifting and magmatism in southern Scandinavia, the North Sea and northern Germany: A review. *In* Wilson, M., Neumann, E.-R., Davies, G. R., Timmerman, M. J., Heeremans, M. & Larsen, B. T. (eds), *Permo-Carboniferous magmatism and rifting in Europe*. London, Geological Society, Special Publications, 223, 11–40. https://doi.org/10.1144/GSL.SP.2004.223.01.02

Nielsen, N. A., 1967. Kodal-forekomsten. Et industriobjekt i Vestfold. *Tidsskrift for Kjemi, Bergvesen, og Metallurgi*, 27(4), 73–76.

Oftedahl, C., 1960. Permian rocks and structures of the Oslo region. *In* Holtedahl, O. (ed), *Geology of Norway*. Trondheim, Norges geologiske undersøkelse, 208, 298–343.

Oftedahl, C., & Petersen, J. S.,1978. Southern part of the Oslo Rift. *Norges geologiske undersøkelse Bulletin, 337*, 163–182.

Petersen, J. S., 1978. Structure of the larvikite-lardalite complex, Oslo-region, Norway, and its evolution. *Geologische Rundschau*, 67(1), 330–342. https://doi.org/10.1007/BF01803271

Pedersen, T. & van der Beek, P., 1994. Extension and magmatism in the Oslo rift, southeast Norway: no sign of a mantle plume. *Earth planetary science letters*, 123(1–3), 317–329. https://doi.org/10.1016/0012-821X(94)90276-3

Philpotts, A.R., 1967. Origin of certain iron-titanium oxide and apatite rocks. *Economic Geology*, 62(3), 303–315. https://doi.org/10.2113/gsecongeo.62.3.303

Philpotts, A. R., 1982. Compositions of immiscible liquids in volcanic rocks. *Controntributions of Mineralogy and Petrology,* 80, 201–218. https://doi.org/10.1007/BF00371350

Pirotte, H., 2023. *Planet Mercury and the behavior of elements in reduced conditions*. Ph.D. thesis, Liège, University of Liège. 307p.

Pufahl, P. K. & Groat, L. A., 2017. Sedimentary and Igneous Phosphate Deposits: Formation and Exploration: An Invited Paper. Economic Geology, 112(3), 483–516. https://doi.org/10.2113/econgeo.112.3.483

Rämö, O.T., Andersen, T. & Whitehouse, M.J., 2022. Timing and Petrogenesis of the Permo-Carboniferous Larvik Plutonic Complex, Oslo Rift, Norway: New Insights from U–Pb, Lu- Hf, and O Isotopes in Zircon. *Journal of Petrology*, 63(12), egac116. https://doi.org/10.1093/petrology/egac116

Ro, H. E. & Faleide, J. I., 1992. A stretching model for the Oslo rift. *Tectonophysics*, 208, 19–36. https://doi.org/10.1016/0040-1951(92)90334-3

Roedder, E. & Weiblen, P. W., 1970. Lunar petrology of silicate melt inclusions, Apollo 11 rocks. Proceedings of the Apollo 11 Lunar Science Conference. *Geochim Cosmochim Acta*, 1(1), 801–837.

Roedder, E., 1984. *Fluid Inclusions*. Reviews in Mineralogy, 12, Mineralogical Society of America, 644 p.

Segalstad, T. V., 1979. Petrology of the Skien basaltic rocks, southwestern Oslo Region, Norway. *Lithos*, 12(3), 221–239. https://doi.org/10.1016/0024-4937(79)90006-9

Shelby, J. E., 2005. *Introduction to glass science and technology*. 2nd ed. Cambridge, U.K., The Royal Society of Chemistry. 308 p. https://doi.org/10.1039/9781847551160-00249

Sorby, H.C., 1858. On the microscopical structure of crystals, indicating the origin of minerals and rocks. *Quarterly Journal of the Geological Society*, 14, 453–500. http://dx.doi.org/10.1144/GSL.JGS.1858.014.01-02.44

Sundvoll, B. A., Neumann, E. -R., Larsen, B. T. & Tuen, E., 1990. Age relations among Oslo rift magmatic rocks: implications for tectonic and magmatic modelling. *Tectonophysics*, 189, 67–87. https://doi.org/10.1016/0040-1951(90)90460-P

Touzé, S., Bru, K., Ménard, Y., Weh, A. & Von der Weid, F., 2017. Electrical fragmentation applied to the recycling of concrete waste – Effect on aggregate liberation. *International Journal of Mineral Processing*, 158, 68–75. https://doi.org/10.1016/j.minpro.2016.11.009

U.S. Geological Survey, 2024. Mineral commodity summaries 2024, U.S. Geological Survey. https://pubs.usgs.gov/publication/mcs2024 (Consulted 10/06/2014)

Veksler, I.V., 2006. Crystallized melt inclusions in gabbroic rocks. In: Webster, J. D. (ed.) Melt Inclusions in Plutonic Rocks. Mineralogical Association of Canada, Short Courses 36, 100-122.

Veksler, I. V., Dorfman, A. M., Danyushevsky, L. V., Jakobsen, J. K., Dingwell, D. B., 2006. Immiscible silicate liquid partition coefficients: implications for crystal-melt element partitioning and basalt petrogenesis. Contributions to Mineralogy and Petrology, 152(6), 685–702. https://doi.org/10.1007/s00410-006-0127-y

Veksler, I. V. & Charlier, B., 2015. Silicate liquid immiscibility in layered intrusions. *In* Charlier, B., Namur, O., Latypov, R. & Tegner, C. (eds), *Layered intrusions*. Dordrecht, Springer geology, 229–258. https://doi.org/10.1007/978-94-017-9652-1

Wang, K., Wang, C. Y. & Ren, Z.-Y., 2018. Apatite-hosted melt inclusions from the Panzhihua gabbroic-layered intrusion associated with a giant Fe–Ti oxide deposit in SW China: insights for magma unmixing within a crystal mush. *Contributions to Mineralogy and Petrology*, 173(7), 1–14. https://doi.org/10.1007/s00410-018-1484-z

Wang, M., Veksler, I., Zhang, Z. C., Hou, T. & Keiding, J. K., 2017. The origin of nelsonite constrained by melting experiment and melt inclusions in apatite: The Damiao anorthosite complex, North China Craton. *Gondwana Research*, 42, 163–176. https://doi.org/10.1016/j.gr.2016.10.015

Wang, Y., Coint, N., Mansur, E. T., Acosta-Gongora, P., Miranda, A. C. R., Nasuti, A. & Baranwal, V. C., 2024. Leveraging domain expertise in machine learning for critical metal prospecting in the Oslo Rift: a case study for Fe-Ti-P-Rare Earth Element mineralization. *Minerals*, 14(4), 377–396. https://doi.org/10.3390/min14040377

Watson, E. B., 1976. Two-liquid partition coefficients: experimental data and geochemical implications. *Contributions to Mineralogy and Petrology,* 56, 119–134.

Winter, J. D., 2010. *Principles of Igneous and Metamorphic Petrology*. Pearson.

Zhang, Y., Namur, O. & Charlier, B., 2023. Experimental study of high-Ti and low-Ti basalts: liquid lines of descent and silicate liquid immiscibility in large igneous provinces. *Contributions to Mineralogy and Petrology,* 178, 7. https://doi.org/10.1007/s00410-022-01990-x

Ziegler, P. A., 1978. North Sea rift and basin development. *In* Ramberg, I. B. & Neumann, E.-R. (eds.), *Tectonics and Geophysics of Continental Rifts*. Dordrecht, Springer, NATO Advanced Study Institutes Series, 37, 249–277. https://doi.org/10.1007/978-94-009-9806-3_21

Ziegler, P. A., 1990. *Geological atlas of western and central Europe*. 2nd ed. London, Shell international company. 239 p.

13. Annex
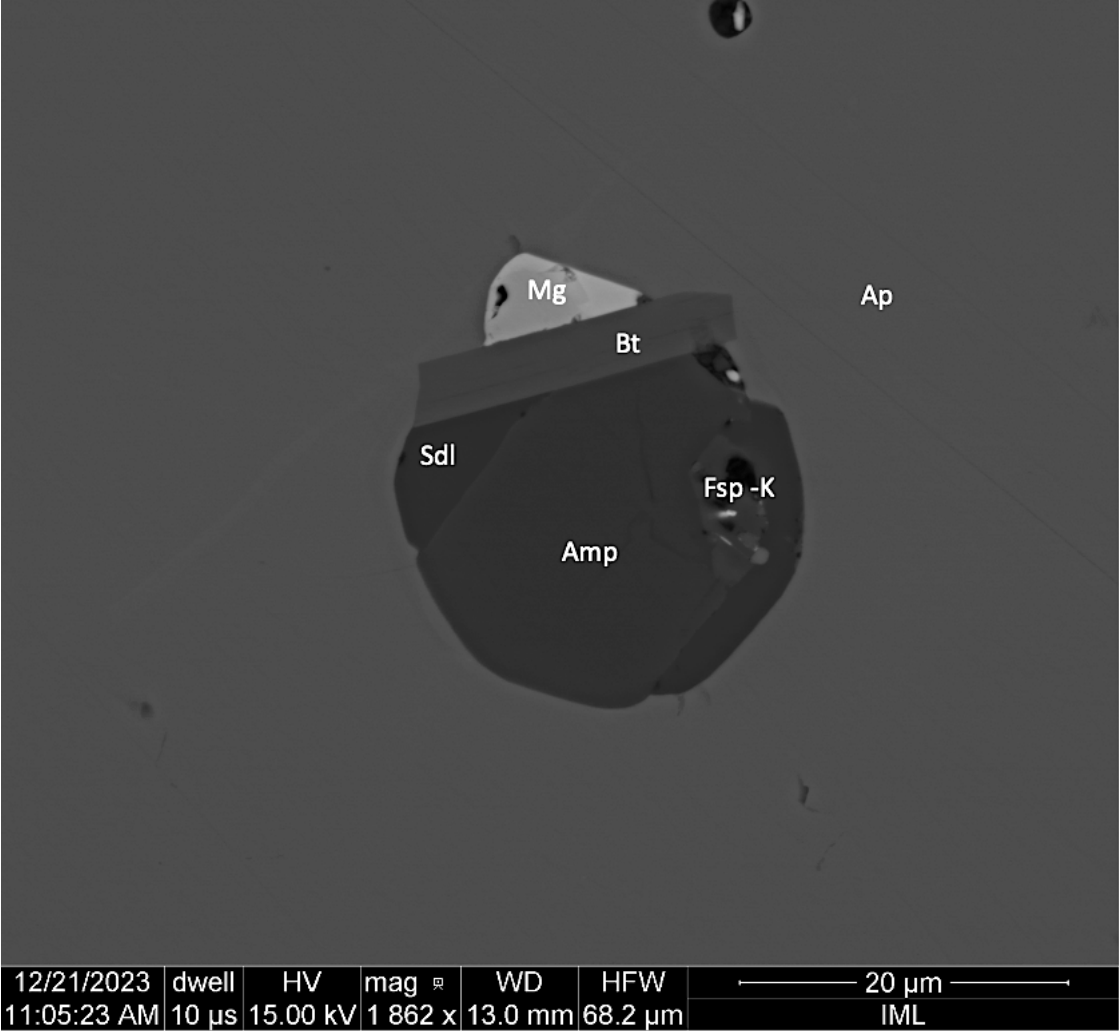
Annex 1. Back-scattered electron images of poly-crystalline inclusion in apatite grain (Kodal sample).

Mg = magnetite, Bt = Biotite, Sdl = sodalite, Amp = Amphibole, Fsp-K = potassic feldspar

Annex 2
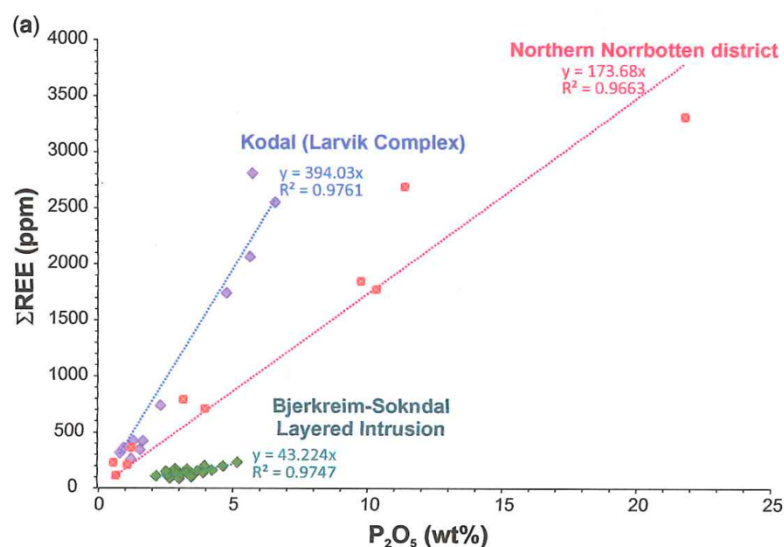
Annex 2. Correlation between total REE content and P₂O₅ content on whole-rock analyses. (Decrée *et al.*, 2022)

Annex 3

Rock type	Characterization	Reference
Foyaite	Hypersolvus nepheline syenite, trachytic texture caused by platy alkali feldspar	Le Maitre et al. (2002)
Jacupirangite	Alkali pyroxenite, Ti-augite with minor T-magnetite, nepheline, apatite, perovskite, and melanite	Derby (1891)
Lardalite	Coarse-grained nepheline syenite, rhomb-shaped alkali, or ternary feldspar and large nepheline	Brøgger (1890)
Larvikite	Augite syenite or monzonite, rhomb-shaped ternary feldspar (with schiller), barkevikite, Ti-augite, and lepidomelane; minor nepheline, quartz, and olivine may be present	Brøgger (1890)
Tønsbergite	Red variety of larvikite, alkali feldspar syenite with rhomb-shaped feldspar	Brøgger (1890)

Annex 3. Local rock names of the Larvik plutonic complex and the Oslo graben (modified from Rämö *et al.*, 2023).
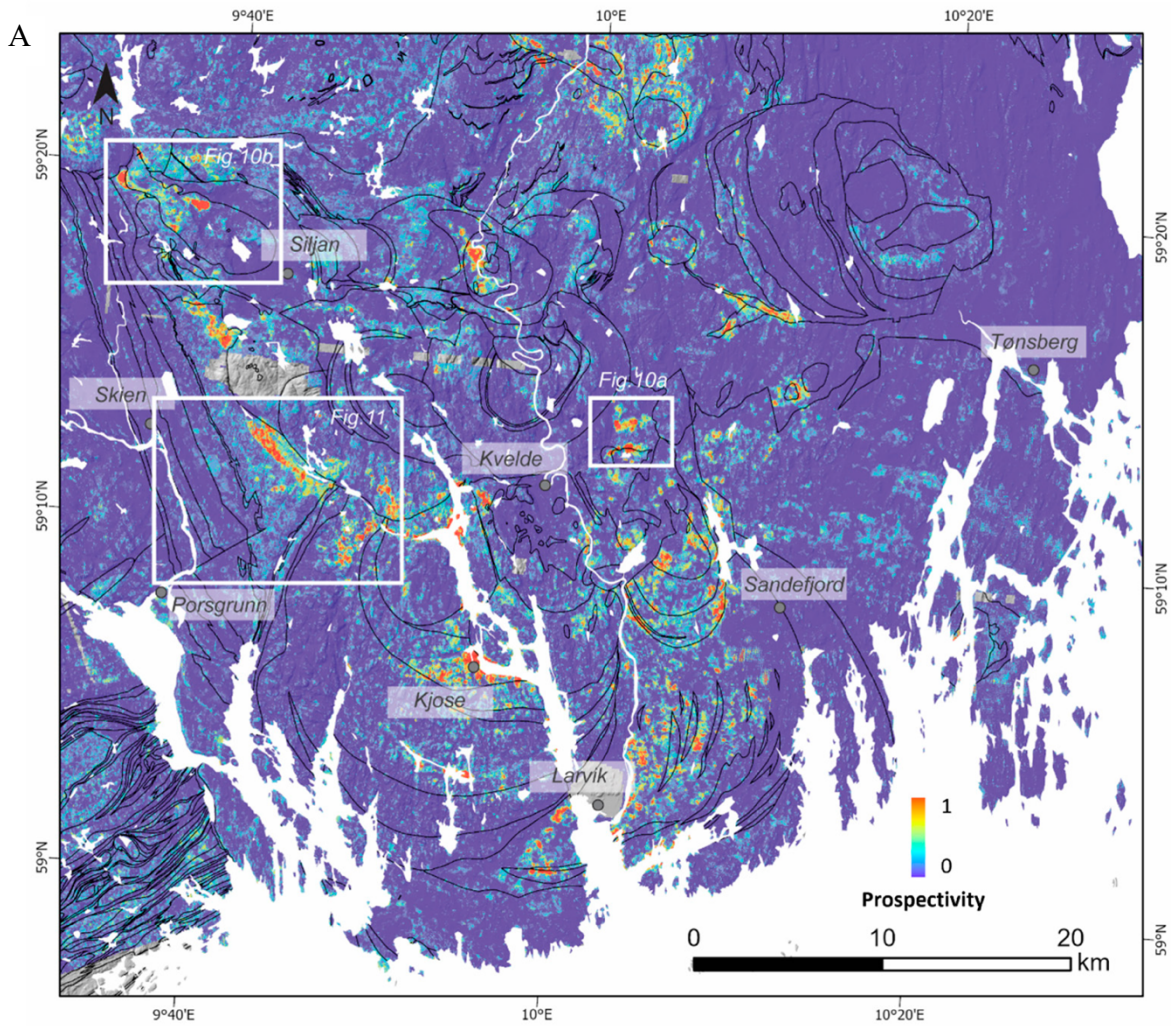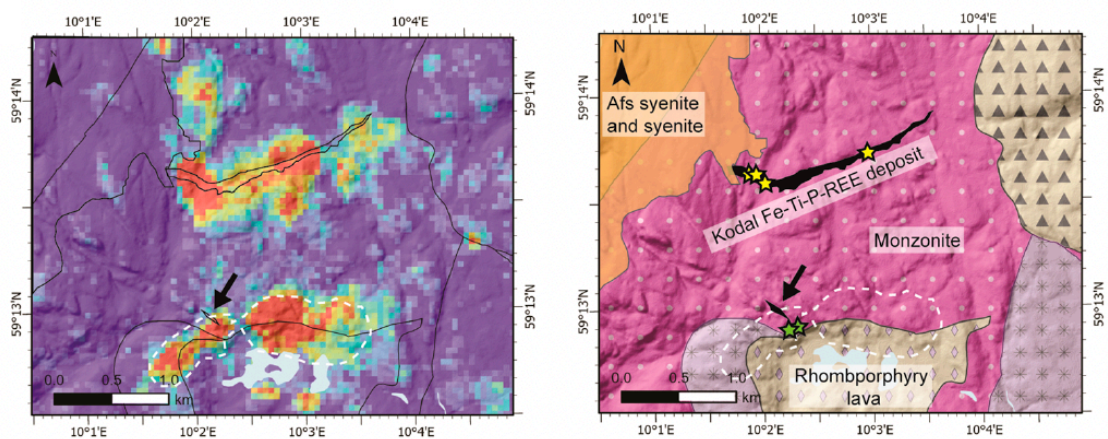
Annex 4. A. Prospectivity map of the target Fe-Ti-P mineralization in the LPC and northern area. B. prospectivity map and the geology map of the Kodal area. The black arow indicates the new mineralization discovered, Kodal South. (modified after Wang *et al.* (2024)).
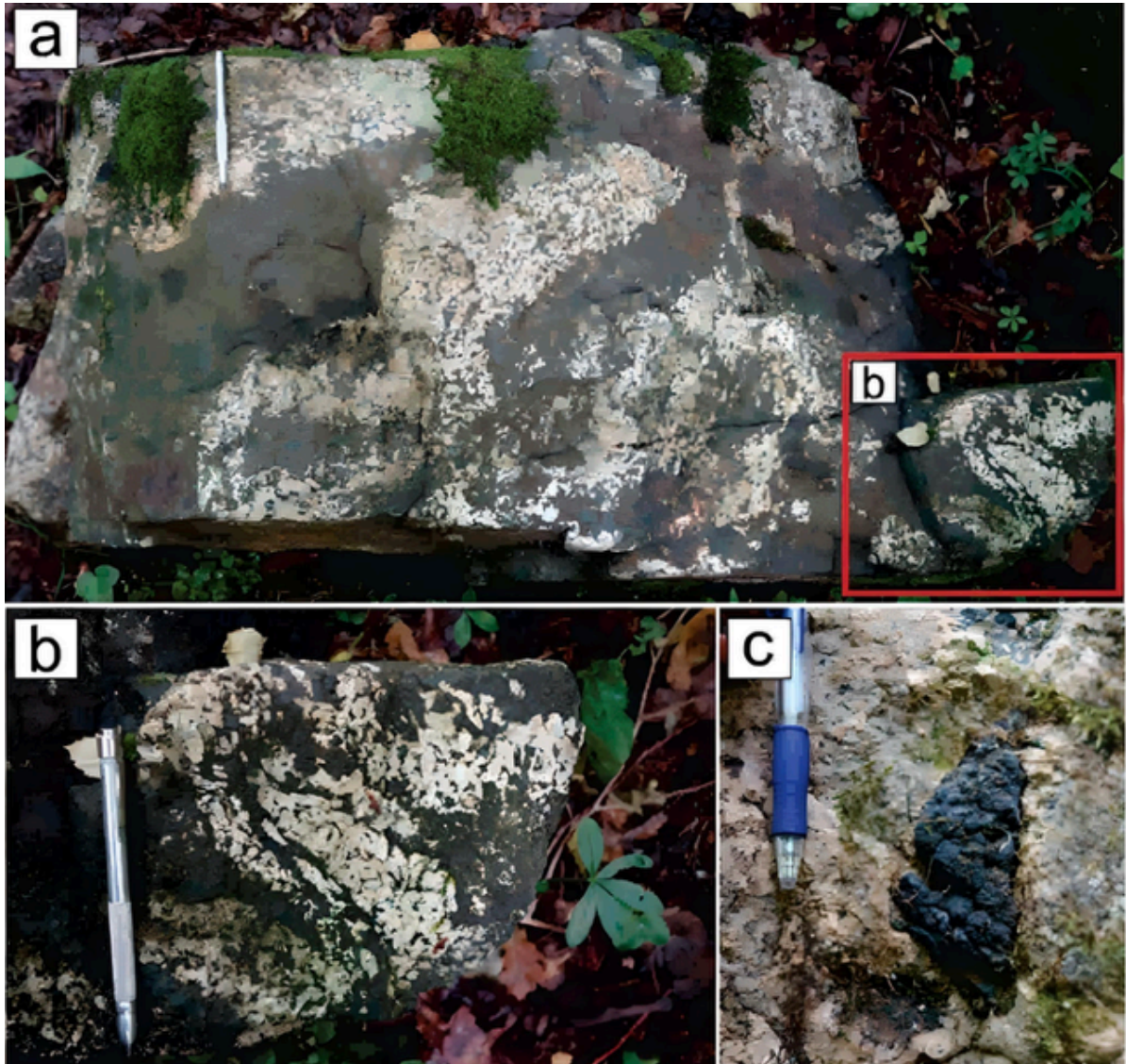
Annex 5. Kodal deposit samples. a-b) flow texture between the monzonite-host (rich in rhomb-shaped feldspar phenocrysts) and centimetric domains of massive P-Fe-Ti ore. c) Sharp contact between centimetric massive ore and monzonite-host. (Miranda *et al.*, 2023)
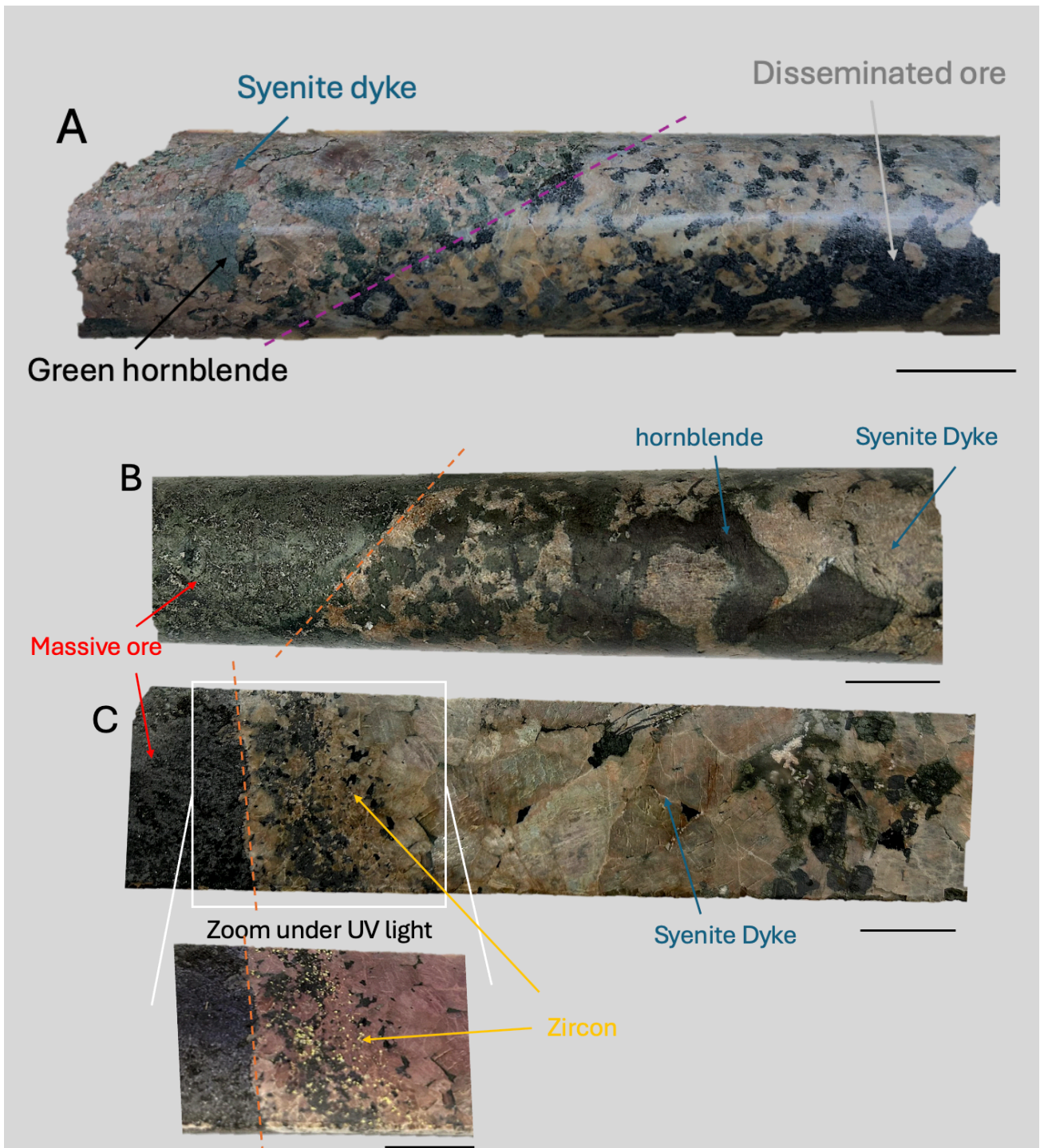
Annex 6. Photographs of Kodal cores (Core DDH66 A. 13 m depth B. 158 m depth C. 20.3 m depth) purple dashed line = contact between the syenite dyke and the disseminated ore, orange dashed line = contact between the syenite dyke and the massive ore. The black line is the scale and represent 2cm.
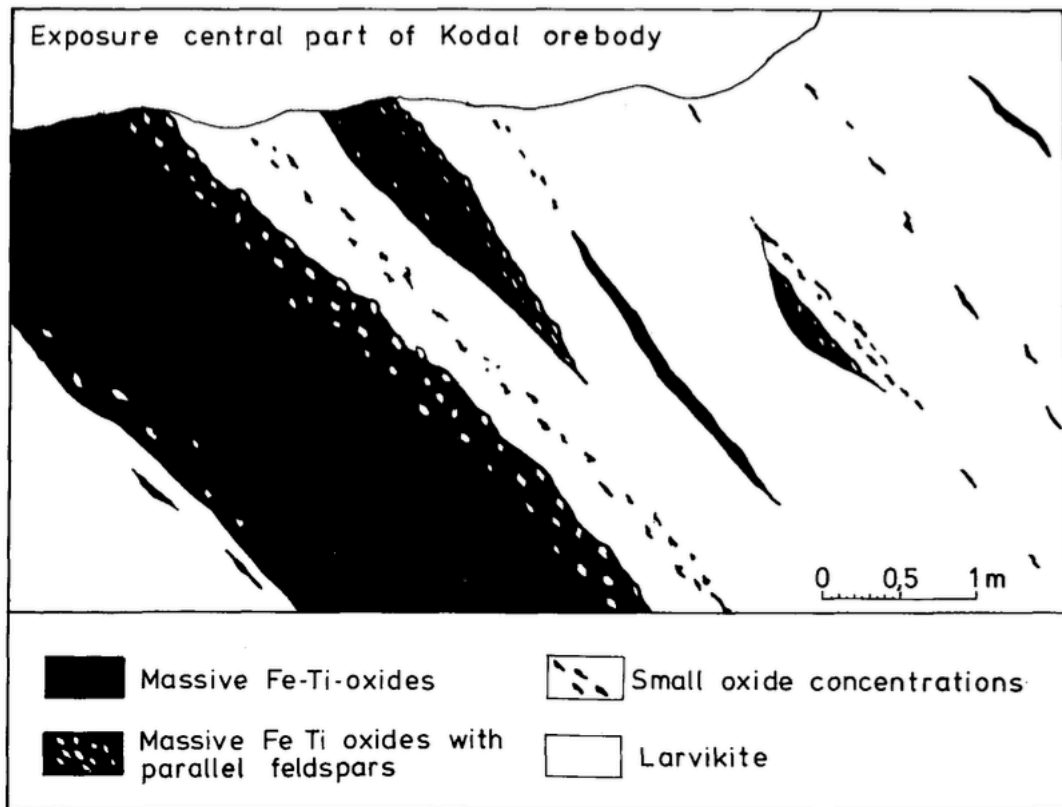
Annex 7. section of the central part of the Kodal orebody schematizing sharp contact at the footwall boundaries, while the hanging walls show a gradational evolution (Lindberg, 1985).
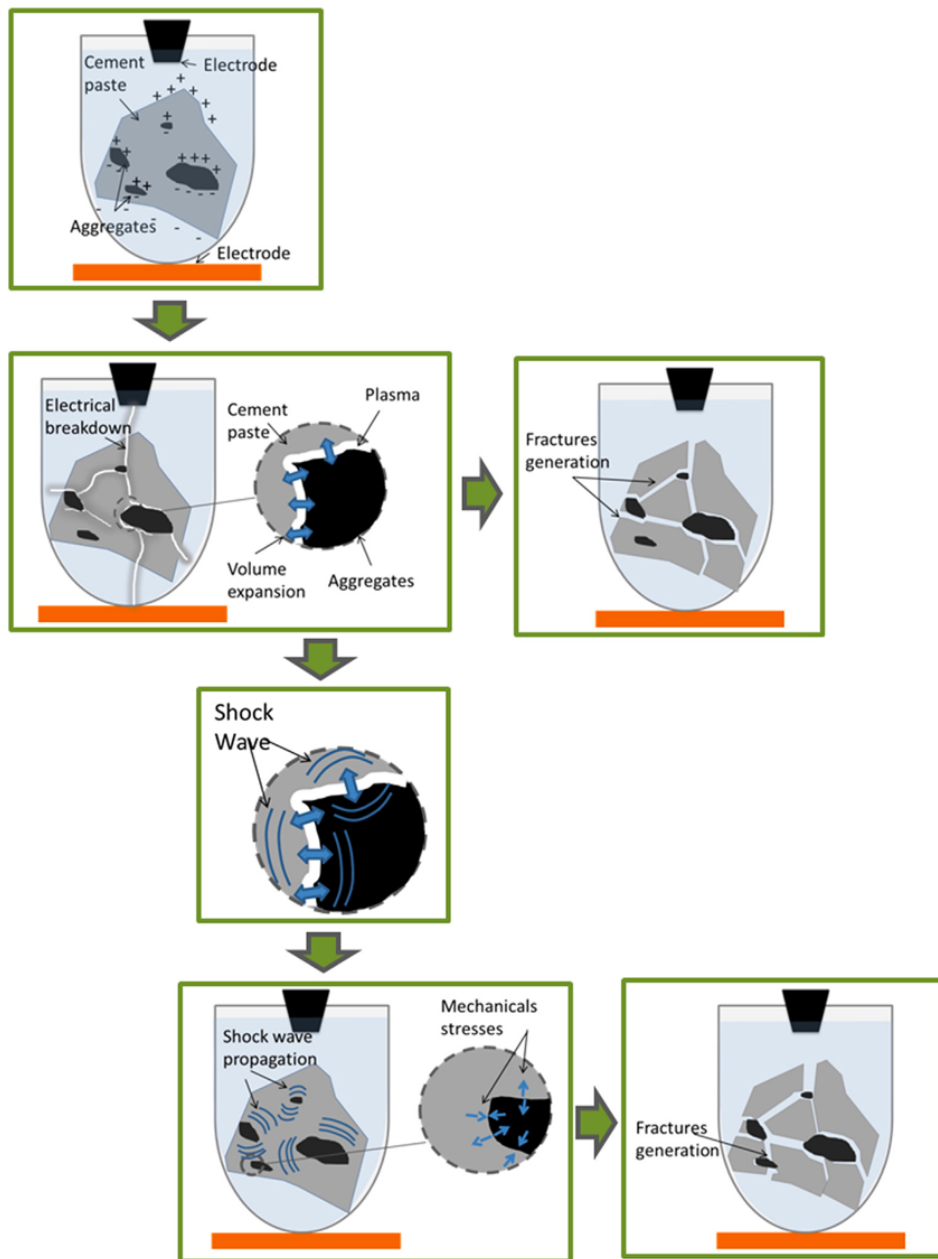
Annex 8. Electrical fragmentation principal mechanisms from Touzé *et al.* (2017)

A

B

Annex 9. A. Selfrag apparatus. B. Sieve the Selfrag fragmented ore portion every 100 pulses approximately (150 μm)
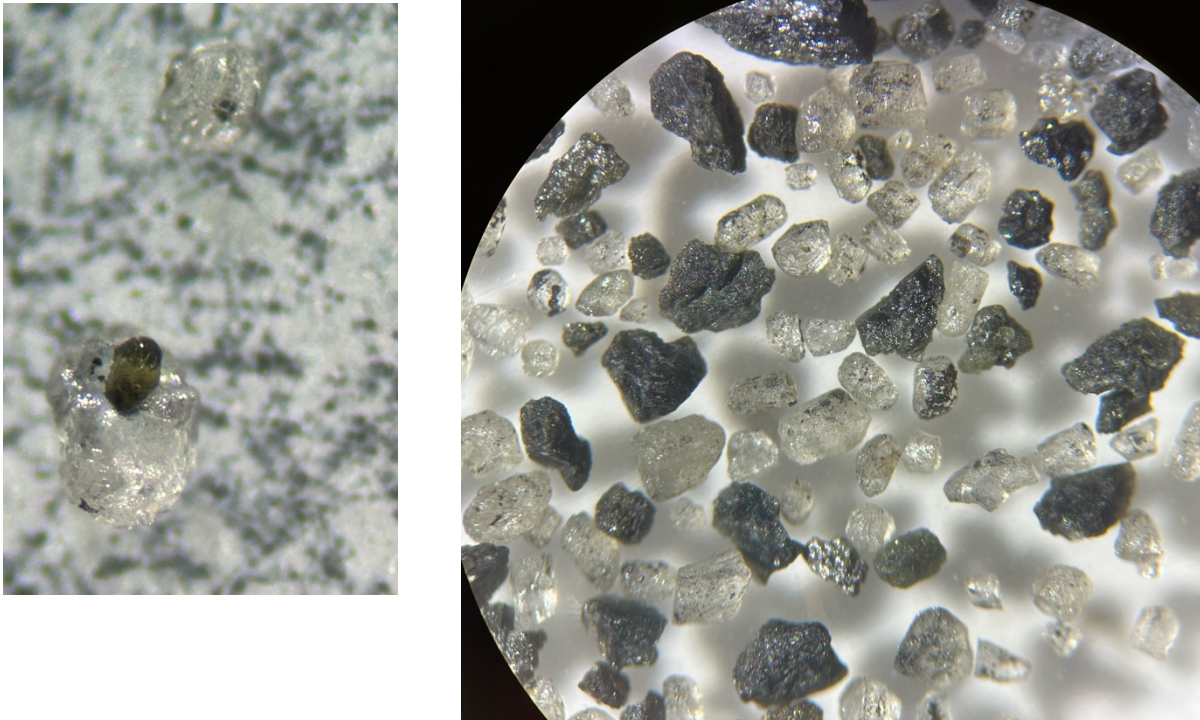
Annex 10

Annex 10. Separated grains resulting from the Selfrag fragmentation went through all the separation phases. The apatite in the left picture shows breakage at the level of the inclusion.
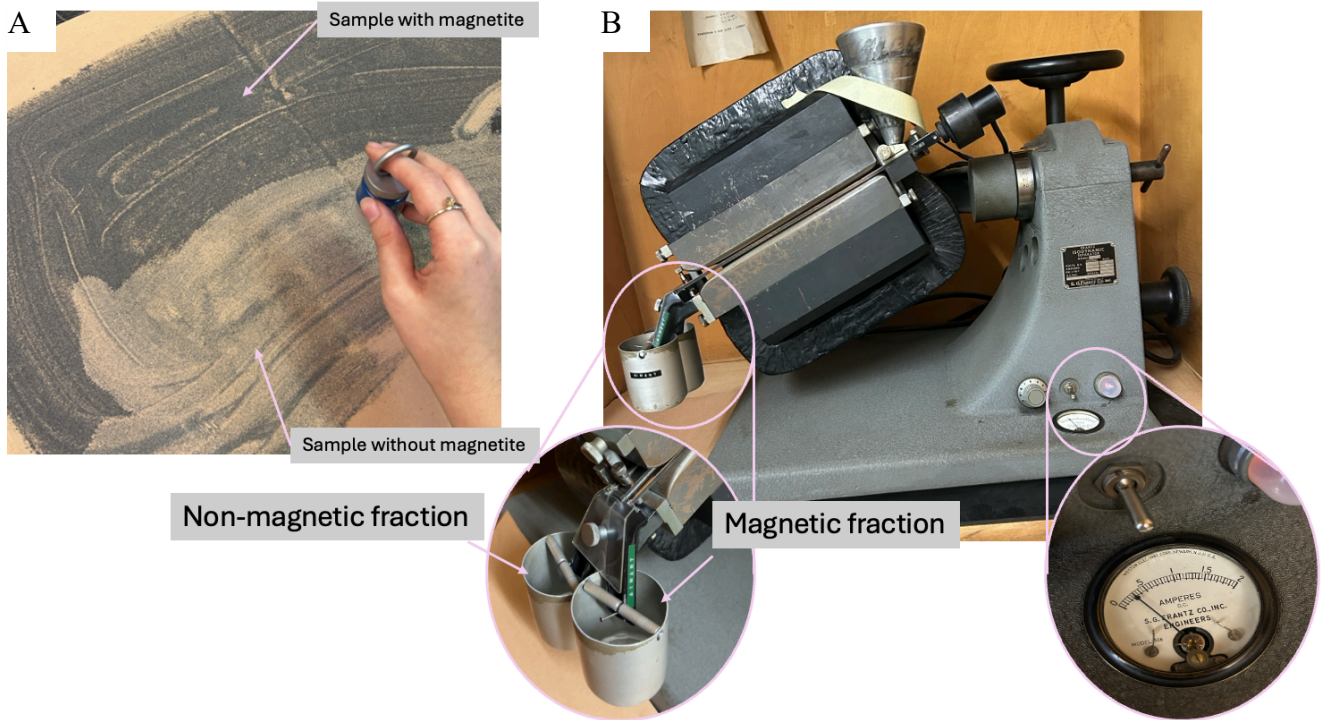
Annex 11. **A.** Separation of the apatite crystal by removing the magnetite with a magnet. **B.** Separation of the apatite crystals using the Frantz separator.

Annex 12

Annex 12. Piston cylinder apparatus, model MavoPress LPC 250-300/50 by Voggenreiter
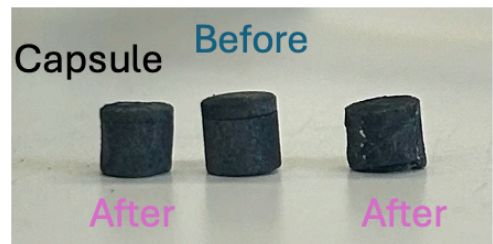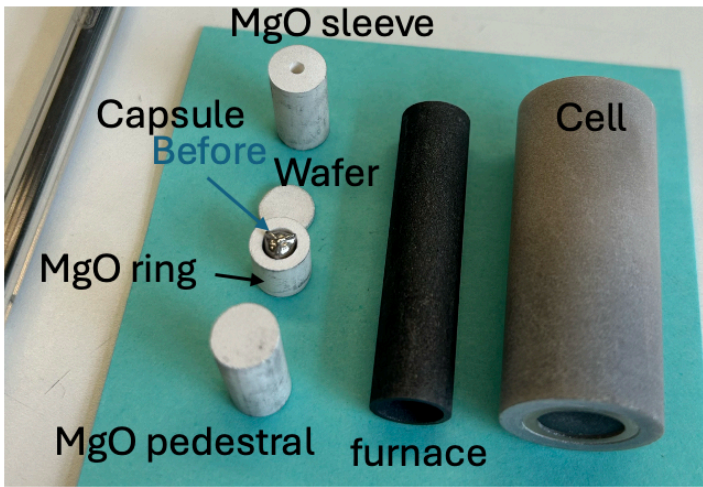
Annex 13. Photographs of the cell assemblage with the different capsules before and after the manipulation in the piston-cylinder apparatus.
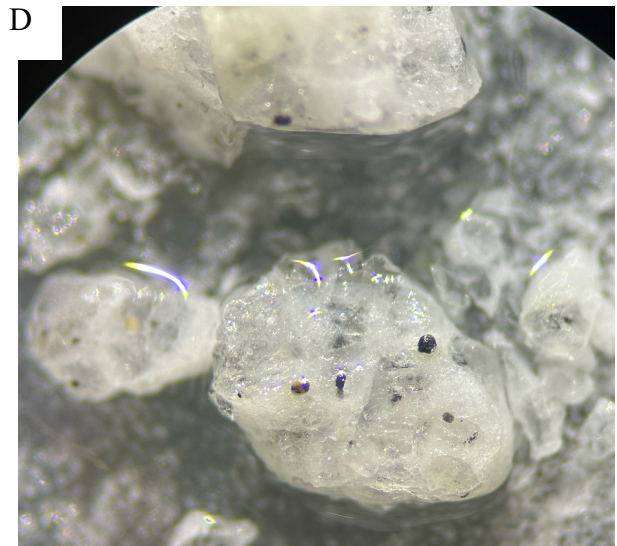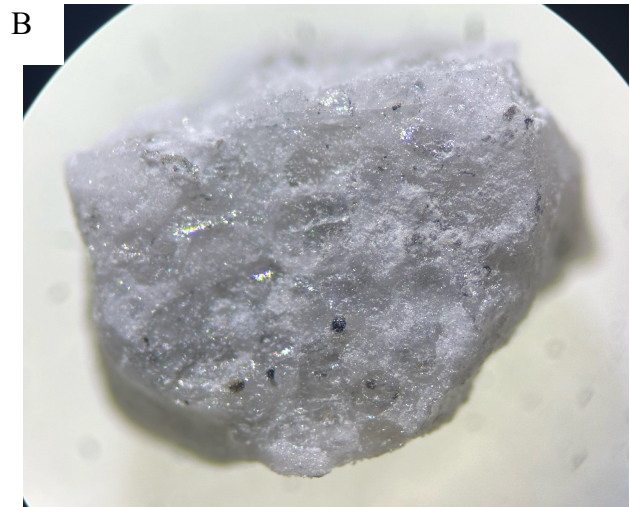
Annex 14. A. Pt-Au capsule opened after being heated in the pressure vessel. B. Apatite crystals agglomerated in the MgO matrix after heating. C-D. Apatite crystals after being graded in order to obtain single crystals, but they preferentially fractured at the inclusion levels.
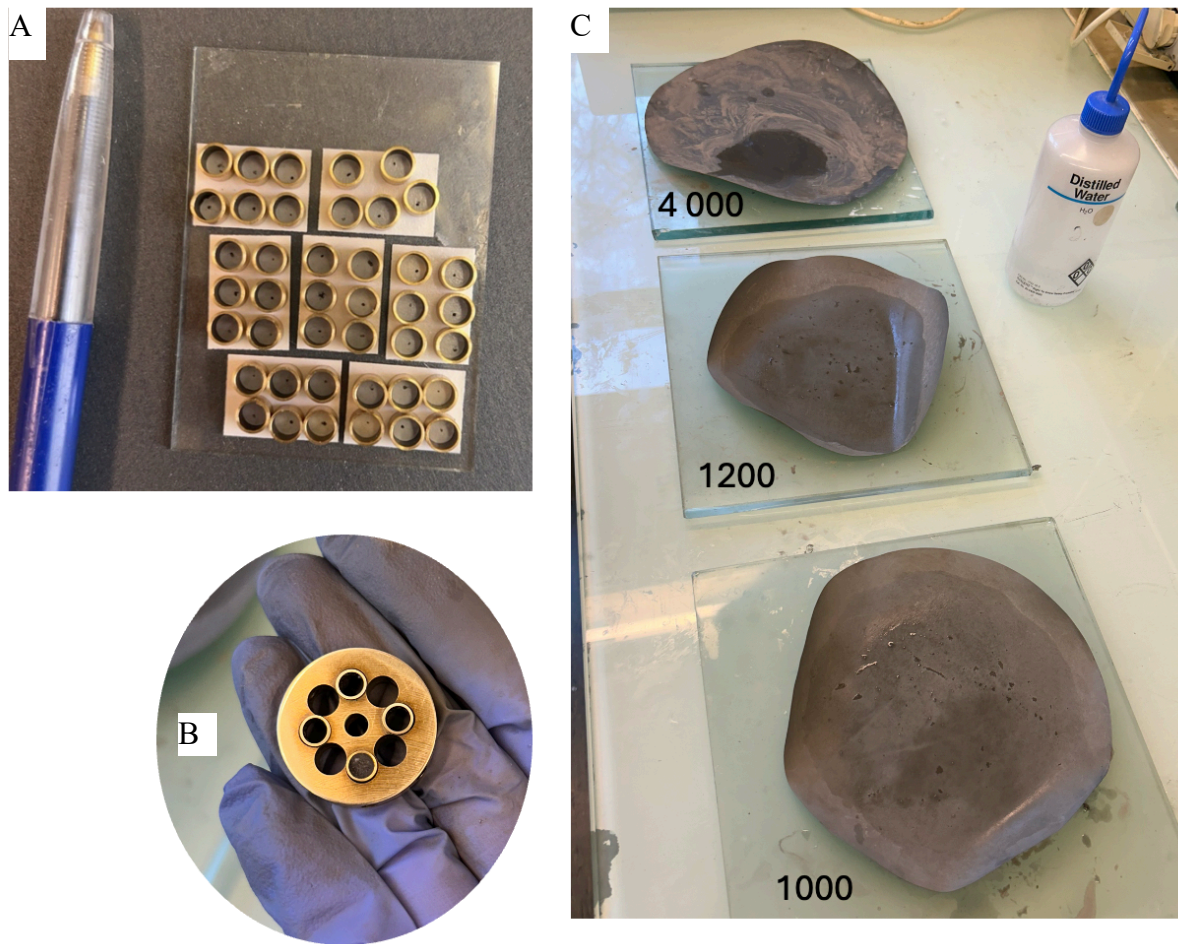
Annex 15. A. Mounting the heated apatite in sleeves to pour epoxy into them. B. Mounting four sleeves together in a wheel to polish them until the inclusion is reached. C. Polishing mat.

Annex 16

Phases	Si	Ti	Al	Fe	Mn	Mg	Ca	Na	K	P	Cl	S	Cu	Ba	La
Pyroxene	26,68	0	0	6,86	0	12,65	7,92	3,62	0,79	0	0	0	0	0	0
Chlorite	16,04	12,25	9,87	19,09	0	12,25	0,37	0	0	0	0	0	0	0	0
Amphibole	21,01	0	8,84	16,44	0	0	13,33	0	0	0	0	0	0	0	0
Biotite	20,02	4,17	9,24	11	0	10,74	0	0	7,74	0	0	0	0	0	0
Magnetite	0	1,05	0,59	96,87	0	1,07	0	0	0,09	0	0	0	0	0	0
Titanite	17,1	24,02	0	0	0	0	22,63	0	0	0	0	0	0	0	0
Plagioclase	67,71	0,75	21,78	0,75	0	0	2,67	7,04	0,06	0	0	0	0	0	0
K-feldspar	24,12	0	23	0	0	0	0	1,61	7,7	0	0	0	0	0	0
Sodalite	19,41	0	19,13	0	0	0	0	19,13	0	0	7,58	0	0	0	0
Bornite	0	0	0	27,48	0	0	0	0	0	0	0	30,01	42,51	0	0
Monazite	0	0	0	0	0	0	0	0	0	18,51	0	0	0	14,88	36,31

Annex 16. Semi-quantitative compositions of phases present in the poly-crystalline inclusions before heating.

Annex 17

Core	MI no.	Phases	SiO$_2$ (wt.%)	TiO$_2$ (wt.%)	Al$_2$O$_3$ (wt.%)	FeO$_{tot}$ (wt.%)	MnO (wt.%)	MgO (wt.%)	CaO (wt.%)	Na$_2$O (wt.%)	K$_2$O (wt.%)	P$_2$O$_5$ (wt.%)	S (wt.%)	Zr (wt.%)	Total (wt.%)
79	79-2-NaClglass	Biotite	40,69	2,78	15,61	8,27	0,08	21,32	0,27	1,44	8,69	0,51	0,34	0	100
79	79-3-NaCl-glass	Si	35,11	1,99	7,26	15,93	0,43	16,36	9,88	8,99	0	3,8	0,26	0	100
79	79-3-NaCl-big	Magnetite	0,1	5,85	3,28	86,11	0,7	3,08	0,49	0,31	0	0,08	0	0	100
79	79-3-little	titanite	14,96	35,32	5,72	10,65	0	3,08	18,29	9,66	0	2,21	0,09	0	100
79	79-3-Ap	Apatite	0,32	0	0,65	0,13	0	0	56,83	0,13	0	41,93	0	0	100
79	79-4-glass	Si	32,7	3,06	11,99	10,77	0	20,4	8,58	8,71	0	3,49	0,28	0	100
79	79-5 I-glass	Silica	36,3	0,57	6,73	15,59	0,22	25,23	5,66	6,44	0,13	2,11	1,03	0	100
79	79-5 I-big	Magnetite	0,11	6,73	1,93	88,56	0,47	1,28	0,48	0,31	0	0,14	0	0	100
79	79-5 I-little	Pseudobrookite	3,5	7,95	11,99	63,23	0	11,03	1,12	0,82	0	0,37	0	0	100
79	79-5 III-h-light	gl (melt)	42,53	1,82	14,9	10,39	0,21	5,82	14,78	7,27	0,25	2,03	0	0	100
79	79-5 III-h-dark	Silica	40,16	1,02	9,23	12,53	0,38	21,71	8,43	4,69	0,15	1,29	0,41	0	100
79	79-5 II-light	titanite	15,05	33,75	4,02	2,04	0	7,86	31,83	2,91	0	2,54	0	0	100
79	79-5 II-h	n.d.	42,27	0,27	7,64	0,94	0	9,74	34,07	4,03	0	0,87	0,17	0	100
79	79-5 II-dark	Apatite	6,53	0	1,5	0,49	0	1,7	55,28	4,44	0,13	29,63	0,3	0	100
79	79-6-triangle	Perovskite	4,23	60,73	3,31	7,25	0	0,68	17,7	5,45	0,48	0,18	0	0	100
79	79-6-light-bottom	titanite	30,4	34,55	6,06	12,22	0	1,5	13,16	0	0	0,28	0	1,83	100
79	79-6-h	gl	42,72	3,58	14,62	10,58	0,32	5,33	8,49	8,34	4,44	1,58	0	0	100
79	79-6-light-up	Pseudobrookite	3,42	12,52	4,84	64,51	0,88	11,51	1,33	0,27	0,06	0,66	0	0	100
79	79-7-light-middle	pyrite	0,09	0	0,33	49,44	0,13	0,05	0,19	0	0	0	49,77	0	100
79	79-7-h	Biotite	40,1	2,34	15,79	8,6	0,08	21,32	0,2	0,56	10,31	0,44	0,26	0	100
79	79-8-light	Magnetite	0,09	5,22	2,3	90,56	0,8	0,38	0,36	0,29	0	0	0	0	100
79	79-8-h	gl	41,91	1,66	17,85	12,01	0,3	5,32	11,55	2,79	4,42	2,19	0,72	0	100
79	79-1a-h	gl	24,89	2,71	12,24	16,96	0,17	14,69	12,38	7,91	1,68	6,37	0	0	100
79	79-1b-light	Magnetite	0,09	6,78	2,8	85,84	0,84	2,37	0,62	0,5	0,04	0,1	0	0	100
79	79-1b-dark	gl	43,25	0,97	14,4	9,63	0,3	12,92	2,97	3,42	9,07	2,03	1,04	0	100
79	79-9-light	ilmenite	0,35	48,63	0,79	42,01	0,87	6,78	0,47	0	0	0,09	0	0	100
79	79-9-h	gl	38,95	6,13	7,72	15,52	0,52	11,67	14,49	1,69	0,5	2,81	0	0	100
79	79-10-light	Magnetite	0,17	2,22	2,79	79,43	1,24	12,82	0,84	0,4	0	0,09	0	0	100
79	79-11a-light	Magnetite	1,96	3,39	4,56	78,09	0,45	8,8	0,99	0,92	0,4	0,44	0	0	100
79	79-11a-h	gl	29,92	1,45	9,42	18,77	0,26	10,38	11,31	7,36	5,35	5,78	0	0	100
79	79-11b-light	Magnetite	2,55	4,69	5,31	78,26	0,42	6,64	0,71	0,35	0,39	0,21	0	0	100
79	79-12-light	Magnetite	0,14	6,58	2,33	87,82	0,99	1,18	0,58	0,25	0,04	0,09	0	0	100
79	79-12-dark	Si	41,36	0,78	8,23	15,48	0,55	22,3	4,08	0,97	4,47	0,97	0,81	0	100
79	79-13-circle	Zircon	28,4	6,9	1,3	4,9	0,15	0,64	0	0	0	0	0,17	57,54	100
79	79-13-light	ilmenite	0,12	49,17	1,11	40,68	0,99	7,47	0,47	0	0	0	0	0	100
79	79-13-h	gl	35,28	7,35	5,22	16,63	0,63	14,24	10,01	6,38	1,58	2,68	0	0	100
79	79-14a-h	n.d.	34,86	3,04	13,12	6,33	0,26	17,54	14,67	9,02	0	0,88	0,29	0	100
79	79-14b-h	titanite	22,93	24,43	3,07	2,85	0,12	4,41	37,3	3,28	0	1,23	0	0,37	100
79	79-15-h	n.d.	36,81	2,41	10,04	15,58	0,22	22,04	4,98	4,28	0,51	2,51	0,63	0	100
79	79-16a-h	n.d.	25,26	1,58	16,02	15,85	0,54	20,61	18,74	0,52	0	0,79	0,11	0	100
79	79-16a-Fe	Magnetite	0,11	0,63	0,14	98,41	0	0	0,71	0	0	0	0	0	100
79	79-15-Fe	pyrite	0,62	6,46	4,76	62,43	0,26	5,7	0,36	0	0,13	0,14	19,14	0	100
79	79-16b-Fe	Ferropseudobrookite	0,44	53,58	0,71	16,26	15,78	9,99	1,02	2,14	0	0,08	0	0	100
79	79-16b-h	n.d.	41,71	0,95	15,3	3,97	0,37	16,42	24,83	5,69	0	0,5	0,25	0	100
79	79-16c-h	n.d.	35,06	1,75	11,17	4,54	0,38	19,38	18,47	7,01	0	1,95	0,29	0	100
79	79-17a-h	n.d.	30,34	0,5	14,76	7,88	0,67	26,6	12,38	4,47	0	2,09	0,31	0	100
79	79-17b-Fe	Pseudobr	0,1	6,79	2,6	71,82	1,8	8,86	7,07	0,95	0	0	0	0	100
79	79-17b-h	n.d.	26,3	0,68	14,88	7,65	0,22	12,4	35,63	1,06	0	1,09	0,08	0	100
79	79-18a-h	Si	38,04	1,27	7,81	12,79	0,28	21,34	8,29	7,69	0	2,22	0,28	0	100
79	79-18a-Fe	Si	40,5	0	10,42	10,97	0	4,46	21,15	8,55	0	3,7	0,24	0	100
79	79-18a-dark	plagioclase	40,79	1,34	23,16	7,49	0	4,13	9,27	11,55	0	2,06	0,22	0	100
79	79-18b-h	gl	33,09	0,56	5,89	22,43	0,43	21,7	9,12	3,77	0	3,01	0	0	100

Annex 17. Semi-quantitative compositions of the heated inclusions measured using SEM coupled with an X-ray detector. Si = residual silica composition; n.d. = undetermined phases, these undetermined phases are characterized by an ensemble of microcrystals and were measured using the areas instead of dots.

Core	MI no.	Phases	SiO$_2$ (wt.%)	TiO$_2$ (wt.%)	Al$_2$O$_3$ (wt.%)	FeO$_{tot}$ (wt.%)	MnO (wt.%)	MgO (wt.%)	CaO (wt.%)	Na$_2$O (wt.%)	K$_2$O (wt.%)	P$_2$O$_5$ (wt.%)	S (wt.%)	Zr (wt.%)	Total (wt.%)
79	79-19-Fe	Pseudobr	1,1	9,61	3,99	75,44	0,55	7,78	0,8	0,28	0,3	0,14	0	0	100
79	79-19-hexagone	pigeonite	46,75	3,54	4,82	6,63	0,07	13,92	23,38	0,53	0	0,2	0,16	0	100
79	79-19-h	Si	40,34	4,13	8,73	9,83	0,2	18,59	10,45	2,44	3,53	1,52	0,24	0	100
79	79-20-Fe	Magnetite	0,15	6,91	4,66	83,82	0,89	2,54	0,67	0,19	0	0,16	0	0	100
79	79-20-h	plagioclase	37,47	0,43	31,21	4,6	0,09	3,88	2,48	16,43	1,93	1,17	0,31	0	100
79	79-21-h	gl	33,84	10,16	7,97	19,66	0,3	7,47	14,63	1,12	0,97	3,88	0	0	100
79	79-21-Ti	Ferropseudobrookite	0,1	50,83	1,84	37,81	0,69	8,33	0,4	0	0	0	0	0	100
79	79-21-Fe	titanite	31,23	33,29	7,63	13,2	0	1,88	11,04	0,19	0	0,46	0	1,09	100
79	79-22-Fe	Magnetite	0,1	3,73	4,34	89,2	0,83	0,93	0,49	0,28	0	0,1	0	0	100
79	79-22-h	gl	35,37	1,61	9,34	14,35	0,48	14,92	9,4	9,5	0,82	4,21	0	0	100
79	79-23a-middle	n.d.	12,9	1,84	42,75	16,4	0,32	19,32	2,9	0,81	0,65	2,12	0	0	100
79	79-23a-h	gl	42,19	1,94	12,05	10,49	0,48	15,57	11,72	2,78	0,5	2,28	0	0	100
79	79-23b-Fe	Magnetite	4,38	0	1,8	75,58	0	5,55	4,32	3,67	0	4,7	0	0	100
79	79-23b-h	SI	37,79	0,21	9,95	3,9	0,35	29,35	8,24	8,74	0	1,05	0,41	0	100
79	79-24-h	n.d.	26,78	1,01	12	13,11	0,98	20,45	23,82	0,7	0	1,03	0,13	0	100
79	79-24-Fe	Magnetite	0,08	0,38	0,14	98,52	0	0	0,88	0	0	0	0	0	100
79	79-24-Fecumulat	n.d.	0,61	35,75	1,06	33,78	1,58	6,18	20,19	0,55	0	0,3	0	0	100
79	79-25-h	n.d.	17,68	2,77	30,03	18	0,51	7,49	11,74	8,33	0	2,27	1,18	0	100
79	79-25-lid?	Anorthite	34	0,18	20,91	2,02	0	3,29	35,85	3,35	0	0,24	0,16	0	100
79	79-26-Fe	pbr	4,62	5,58	8,54	67,19	0,28	8,44	2,01	2,63	0	0,7	0	0	100
79	79-26-h	gl	35,35	1,21	7,12	12,76	0,08	20,97	11,94	6,8	0	3,77	0	0	100
79	79-27-h	n.d.	36,02	1,52	7,65	8,43	0,67	24,11	10,02	8,24	0	2,95	0,39	0	100
79	79-28-Fe	ilmenite	0,43	50,47	0,72	41,84	1,1	4,45	0,9	0	0	0,1	0	0	100
79	79-28clair	titanite	29,05	39,15	0,65	1,91	0	0,31	28,21	0,22	0	0,21	0	0,3	100
79	79-28moyen	gl	42,36	5,79	9,86	11,02	0,7	5,4	14,28	7,55	0,35	2,69	0	0	100
79	79-28gris	titanite	24,64	35,42	1,69	16,73	0,59	1,31	17,36	1,79	0	0,47	0	0	100
79	79-28-H?	ilmenite	0	52,01	0,72	41,11	1,16	4,23	0,77	0	0	0	0	0	100
79	79-29-Fe	pyrite	0,11	0	2,45	42,97	0	0,27	0,58	0	0	0	53,63	0	100
79	79-29-H	n.d.	31,44	2,55	12,64	13,59	0	21,71	7,08	7,24	0,11	2,99	0,65	0	100
78	78-1-h	Biotite	41,16	2,27	16,26	7,21	0	22,11	1,44	2,87	6,22	0,45	0	0	100
78	78-1-Fe	Si	26,73	1,44	10,04	11,26	0	23,35	25,91	0	1,26	0	0	0	100
78	78-1b-h	gl	38,23	1,35	10,68	10,03	0	23,56	10,05	1,76	0	4,34	0	0	100
78	78-2a-h	chlorite	42,47	1,76	13,82	6,57	0	23,45	4,51	2,79	4,17	0,46	0	0	100
78	78-2b-h	chlorite	44,92	1,72	12,11	7,6	0,29	18,21	10,78	4,1	0,27	0	0	0	100
78	78-3-Fe	Pbr	1,09	9,11	7,75	74,88	0,62	5,94	0,47	0	0,15	0	0	0	100
78	78-3-H	n.d.	38,98	1,06	8,48	13,94	0,4	27,17	4,3	1,59	2,63	0,9	0,54	0	100
78	78-3-amph	Biotite	42,02	1,62	15,36	5,74	0	25,22	0,29	1,25	8,51	0	0	0	100
78	78-4-h	chlorite	42,77	1,3	12,83	7,41	0,29	20,61	10,04	3,5	0,59	0,67	0	0	100
78	78-5-h	n.d.	24,03	0,17	10,79	1,87	0,11	17,75	30,99	2,32	0	11,82	0,17	0	100
78	78-6-dark	Biotite	41,78	2,36	14,53	6,37	0,08	24	0,18	2,26	7,9	0,31	0,23	0	100
78	78-6-crystal	Si	45,8	1,9	9,81	8,03	0,19	17,72	12,16	3,71	0,24	0,22	0,21	0	100
78	78-6-h	gl	43,39	2,24	15,65	7,02	0,14	13,77	9,61	3,66	3,15	1,37	0	0	100
78	78-7-Fe	Ferropseudobrookite	0,08	54,34	0,35	34,36	1,35	8,93	0,6	0	0	0	0	0	100
78	78-7-h	gl	40,2	6,61	6,65	11,43	0,55	14,09	16,53	2,83	0	1,11	0,14	0	100
78	78-8a-h	gl	31,25	6,05	10,01	7,87	1,05	15,54	6,15	10,04	5,89	6,15	0,19	0	100
78	78-8a-Fe	Ferropseudobrookite	0,47	56,01	0,27	25,94	3,17	12,92	1	0,14	0,09	0	0	0	100
78	78-8b-ap	Ap	1,57	0,1	0,12	0,52	0	1,4	36,21	16,89	0,26	42,93	0	0	100
78	78-8c-Fe	ilmenite	2,04	32,24	9,25	32,02	6,23	13,32	3,05	1,23	0	0,62	0	0	100
78	78-8c-h	Si	31,18	1,54	4,1	11,84	3	28,68	8,68	3,89	0,05	6,82	0,23	0	100
78	78-8c-Fe+	Magnetite	0,32	0,52	0,24	97,37	0,07	0	1,16	0,15	0	0,18	0	0	100
78	78-9-Fe	ilmenite	0	49,54	1,1	35,93	1,78	11,22	0,44	0	0	0	0	0	100
78	78-9-h	gl	34,16	4,86	5,73	14,2	0,82	22,04	5,27	5,84	3,16	3,92	0,81	0	100
78	78-9-Felittle	Perovskite	10	42,52	1,09	5,54	0,34	12,11	27,4	0,86	0,14	0	0	0	100
78	78-10-Fe	Ferropseudobrookite	0	51,31	2,54	32,43	1,34	11,2	1,19	0	0	0	0	0	100
78	78-10-H	gl	35,59	7,29	9,02	12,89	0,7	12,46	10,56	8,74	0,24	2,51	0	0	100
78	78-11-h	n.d.	34,59	0,65	10,97	3,97	0	15,82	26,75	3,5	0	3,58	0,17	0	100
78	78-11-Fe	n.d.	17,96	27,66	2,21	6,35	0	8,99	33,34	1,83	0	1,43	0	0,24	100
78	78-1-MagnetiteO-Fe	pbr	0,15	10,03	6,31	76,68	0,72	5,44	0,37	0,17	0	0,11	0	0	100
78	78-1-MagnetiteO-h	Biotite	39,25	2,43	17,73	6,94	0	22,82	0,21	2,55	7,54	0,32	0,2	0	100
78	78-1-MagnetiteO-h?	Biotite	39,78	1,9	16,97	6,92	0	22,05	1,18	1,71	9,03	0,46	0	0	100
78	78-1b-MagnetiteO-H	gl	37,18	2,23	14,74	6,23	0,09	7,28	18,93	8,08	1,95	3,29	0,21	0	100
78	78-1c-MagnetiteO-H	gl	45,1	2,11	9,44	6,48	0,23	6,65	19,64	6,19	0	5,04	0,19	0	100
78	78-1d-MagnetiteO-h	gl	35,99	2,11	16,31	7,15	0,09	16,13	11,39	5,49	2,79	2,55	0,22	0	100
78	78-2-MagnetiteO-Fe	Ferropseudobrookite	0,13	55,27	0,87	32,8	1,12	9,43	0,37	0	0	0	0	0	100
78	78-2-MagnetiteO-H	gl	38,76	5,07	10,73	12,41	0,73	7,26	15,9	3,62	1,78	3,74	0,19	0,29	100
78	78-3-MagnetiteO-Fe	Ferropseudobrookite	0,1	58,08	1,17	26,2	1,29	12,49	0,67	0	0	0	0	0	100
78	-3-MagnetiteO-Fe-dro	Magnetite	0,14	8,54	1,68	82,02	0,9	5,91	0,59	0,2	0	0	0	0	100
78	78-3-MagnetiteO-h	gl	42,64	6,32	10,69	8,4	0,5	4,69	12,75	6,06	4,22	3,73	0,21	0,24	100
78	78-4-MagnetiteO-h	gl	43,09	4,69	7,17	9,77	0,55	15,13	11,84	3,87	2,42	1,47	0	0	100
78	78-4b-MagnetiteO-h	gl	35,78	7,24	9,2	13,15	0,43	16,64	14,27	0,35	0	2,94	0	0	100
78	78-4-MagnetiteO-h?	gl	38,16	7,82	10,54	9,1	0,4	8,15	20,72	0,52	0,14	4,45	0	0	100
78	78-4c-MagnetiteO-h	gl	36,6	4,83	15,43	8,34	0,72	6,41	21,51	0,39	0	5,77	0	0	100
78	78-5-MagnetiteO-Fe	Magnetite	0,09	8,35	1,09	88,68	0,36	0,93	0,17	0,15	0	0	0	0,17	100
78	'8-5-MagnetiteO-hligh	enstatite	39,12	0,12	0,87	13,35	0,44	43,49	1,24	0,6	0	0,4	0,36	0	100
78	'8-5-MagnetiteO-hdarl	gl	41,7	1,44	14,14	8,86	0,39	6,74	11,81	12,29	0,71	1,92	1,03	0,28	100
78	78-5-MagnetiteO-h	Si	34,21	1,46	7,43	13,35	0,42	21,61	10,82	5,64	0,86	3,24	0,95	0	100
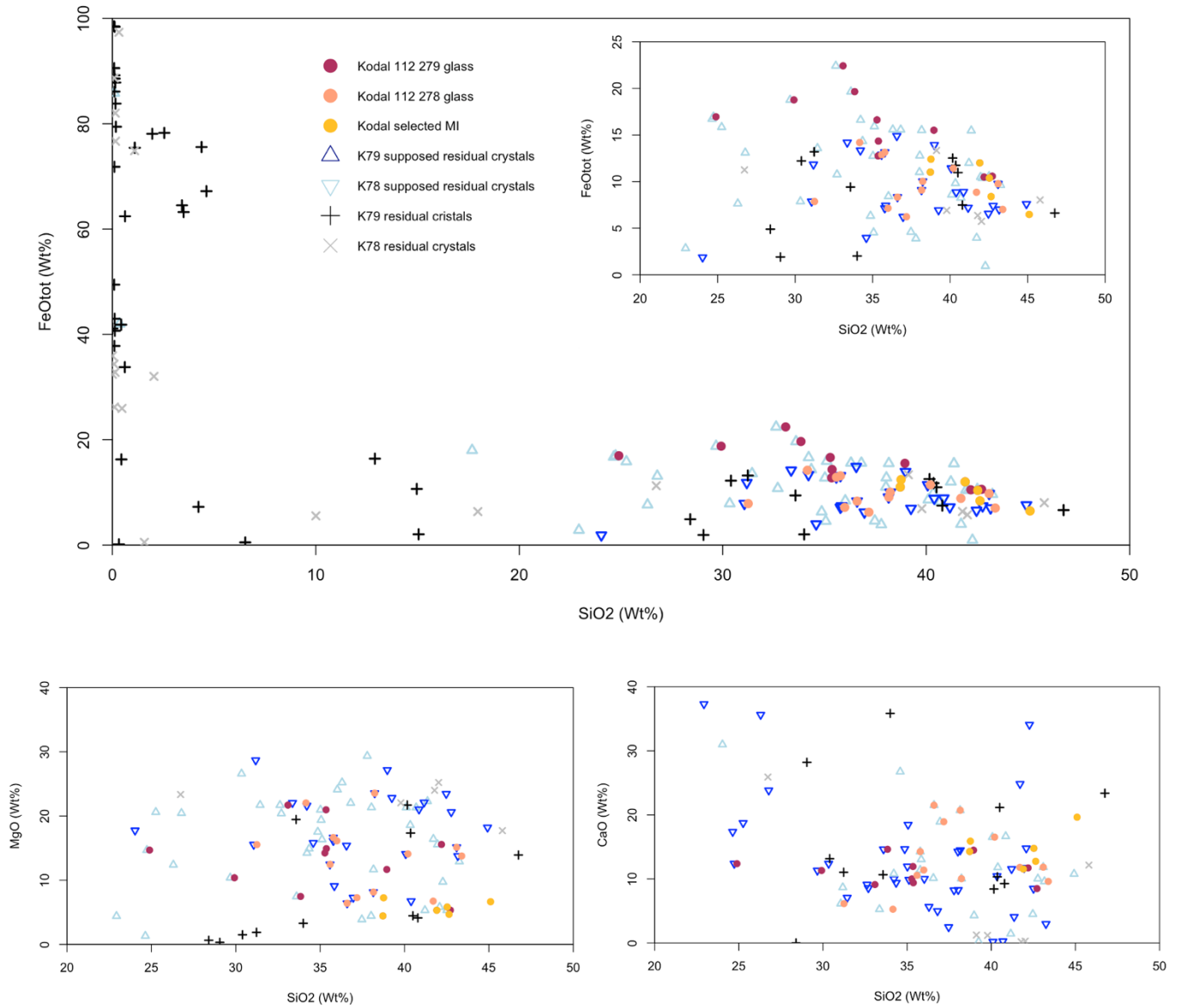
Annex 17. Correlation of major elements among all the phases measured in the heated inclusions.

A (78-MgO-1F)

A' 150 µm

B (78-MgO-2G

B' 20 µm

C (78-4) 50 µm

D (78-2) 50 µm
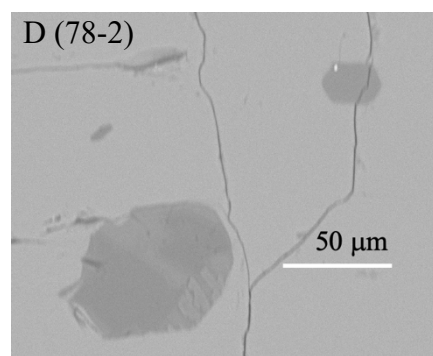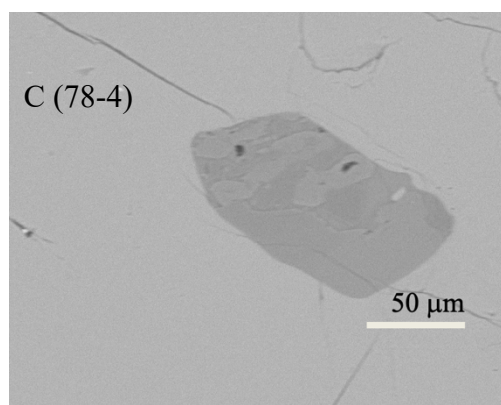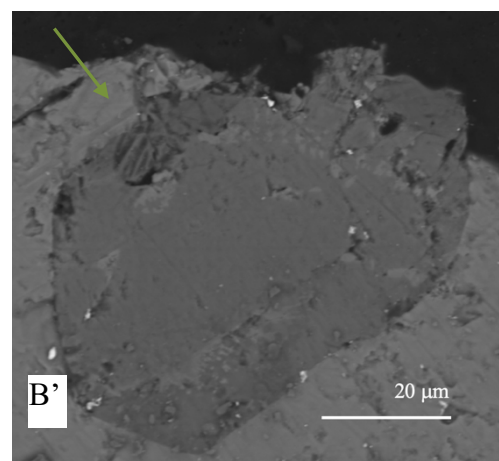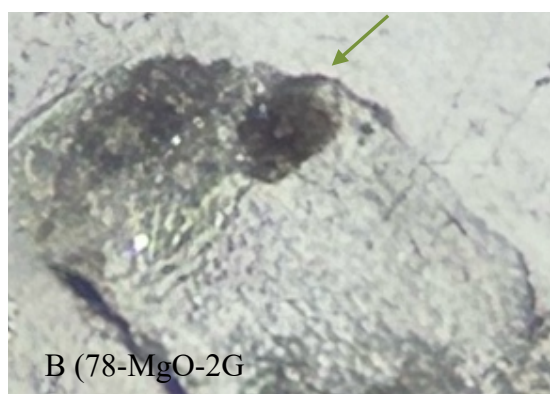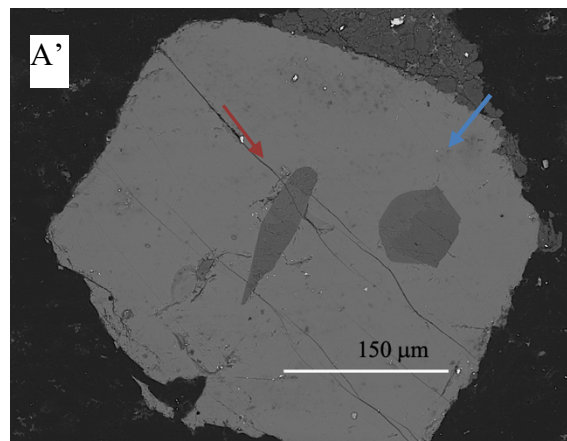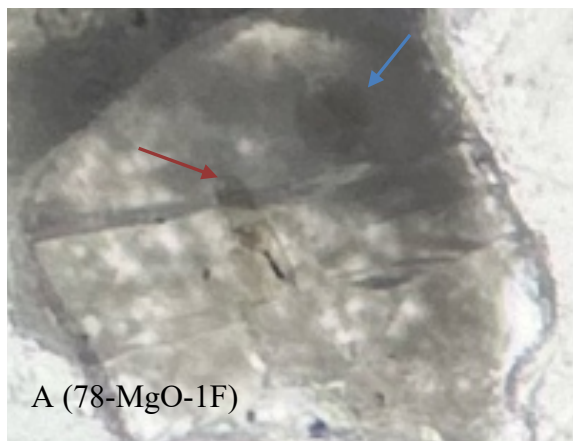
Sample no.	SiO$_2$	TiO$_2$	Al$_2$O$_3$	FeO$_{tot}$	MnO	MgO	CaO	Na$_2$O	K$_2$O	P$_2$O$_5$	Total
78-MgO-1F-1(H)	41,01	2,80	16,13	7,04	0,00	23,11	0,00	2,86	7,03	0,00	100,00
78-MgO-1F-2(clair)	50,39	0,83	8,30	7,49	0,00	19,33	9,64	4,02	0,00	0,00	100,00
78-MgO-1F-2(foncé)	42,11	3,08	14,42	7,02	0,00	23,73	0,00	2,61	7,03	0,00	100,00
78-MgO-2G	44,29	1,94	12,62	8,75	0,00	16,52	12,06	3,83	0,00	0,00	100,00
78-2(big)	42,47	1,76	13,82	6,57	0,00	23,45	4,51	2,79	4,17	0,46	100,00
78-2(little)	44,92	1,72	12,11	7,60	0,29	18,21	10,78	4,10	0,27	0,00	100,00
78-4	42,77	1,30	12,83	7,41	0,29	20,61	10,04	3,50	0,59	0,67	100,00

Annex 18. Heated solid inclusions. A-B. Binocular photographs, with arrows pointing directly at the inclusions. A'-B'. Respective back-scatter images of the aforementioned inclusions. C-D. Back-scatter images of other solid inclusions. The table represents the semi-quantitative composition of the solid inclusions.